POLITECNICO DI TORINO

Corso di Laurea Magistrale in Ingegneria Energetica e Nucleare

Dipartimento di Energetica, DENERG

Experimental Parametric Study of Spoiler Plates Effect on Flow-Induced Motion of Floating Offshore Wind Turbines Platforms

Relatore:
Prof. Giuliana Mattiazzo

Candidato:
Valerio Bianchi

A.A. 2018-2019

Alla mia famiglia e a tutti coloro che con piccoli e grandi gesti hanno contribuito a proseguire nel migliore dei viaggi. Infinitamente grazie.

"I'm the master of my fate, I'm the captain of my soul" [W. H. Henley]

Contents

Abstract

After Fukushima Daichii accident in 2011 and the consequent shutdown of most of the nuclear power plant in Japan, the Japanese government is investing resources in renewable power production projects, and particularly offshore wind projects. The offshore potential is larger than the inland.

The deep-water platform design is a crucial point for this kind of technologies. The power output and the performance of the wind turbine is strongly related to the relative orientation with the wind. Large motion of the platform would compromise the optimal efficiency.

According to what previously stated, the present work is investigating on fluid-structure interaction phenomena affecting deep-water platforms. In moored platforms, sea current generates vortices in the wake of structure that would excite the motion through alternating pressure forces on the platform. Self-excited and self-limited behavior can result in resonances between the frequency of the vortices and the frequency of the motion of the platform. This phenomenon has been investigated in the recent years and named as Flow-Induced Motion (FIM). Resonances are extreme conditions for the mooring system, as the cyclic loads acting on them will result in a reduction in lifetime of the component.

The aim of the present work is to analyze and mitigate experimentally the Flow-Induced Motion phenomenon, acting on a spar platform scaled model. The aspect ratio of the model is A_R=1.5 and the mitigation technique object of investigation consists on spoiler plates arranged on surface of the model. The choice of the mitigation device has been taken accordingly to the lack of research present in literature.

The routine used to investigate the effectiveness of the device is a parametric study involving three different set of parameters: aspect ratio of the spoiler ($A_{R,s}$), number of rings of plates (n_L) and number of plates per ring (n_D). Once the parametric study can clarify the influence of the parameters on the FIM mitigation, the Most Improved configuration can be found.

Aknowledgements

My path towards the achievement of one of my life objectives would not have been possible without the help of the people around me in this year at the University of Tokyo. This experience revealed to be one of the best in my life.

First of all, i want to thank my supervisor at the University of Tokyo, my sensei, Prof. Hideyuki Suzuki: the help, the trust, the resources, the advises revealed to be indispensable in developing this work. His great knowledge and experience gives the Ocean Space Planning Laboratory something that other labs are not provided with.

From the Politecnico di Torino i want to thank my supervisor Prof. Giuliana Mattiazzo. I want to thank her for the time spent for reviewing my work, the great knowledge shared and the work and life advises. I want to thank her for the late night calls because of the time-lag. Even though the distance and the time issues, she could be able to find time to revise and giving me useful hints for my work.

Dr. Rodolfo Gonçalves is another person i am really glad to have worked with. He shared with me ideas, knowledge and experiences regarding an engineering field completely new according to my background. I wanna thank him for the opportunity given and the time spent in reviewing my drafts and solving my doubts.

I want to thank Leandro Pinheiro da Silva, Fredi Cenci and Anja Schnepf for the support and the team work carried out in the time spent together. Wonderful people that i would be glad to meet again in the future. Hard workers and good friends.

My first Japanese friend, my tutor, my labmate Hiroki Shiohara. Thank you for you big help. You welcomed a confused gaikokujin in his first travel in Japan in the best way possible.

I want to thank all the present and past OSPL members, Prof. Hirabayashi, Prof. Yoshimura, Ass. Prof. Houtani, Sakai-san, Fukui-san, Marielle, Maria, Pedro, Matheus, Mao, Katafuchi-san, Kanata-san, Sakata-san, Makimura-san and all the other member of the Kashiwa Lab. branch. The lab value is given by the people that are working into.

I want to thank my university, Politecnico di Torino, for the great opportunity of study and life maturity: an experience like this is unique.

Thank you to my family, my lifetime friends and my new-discovered friends. All of them have been part of this work, supporting me and cheering me up like the top player who scores the victory goal at the last second.

Thank you very much to everyone.

Minasan, arigatou gozaimashita.

Grazie mille a tutti.

List of Figures

List of Tables

Chapter 1

Introduction

1.1 Offshore Wind Power

Nowadays, offshore projects are one of the most promising and advanced innovation in wind power generation field. Even though the capital investment is high and the payback period is long, especially for deep-water application, the power production and the capacity factor make them an interesting alternative to onshore applications.

In offshore applications, wind can be exploited in a more efficient way than onshore. The wind speed, because of the lack of obstacles (roughness) far away from the coast, is less unstable and higher than inland. This ensures a larger exploitation of the wind energy, increasing the capacity factor of those plants. A comparison of capacity factor for the two sector of wind energy production is shown below.

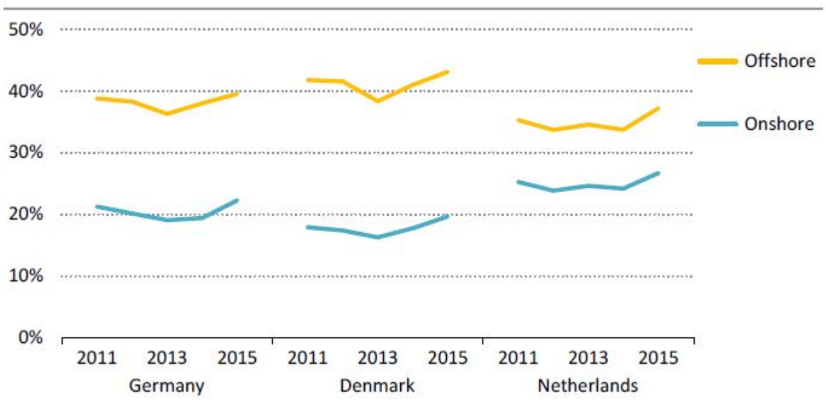

Figure 1.1: Offshore and onshore capacity factor in Germany, Denmark and Netherlands showed in IEA Technical Report[1].

European countries are the leaders in this field: the areas with bigger potentiality are the northern Europe countries, where the shallow sea depths give an advantage in terms of installation of fixed-bottom wind farms.

Indeed, offshore application can be for both shallow and deep-water condition, with great differences in their design, as shown in Figure 1.1. The cost of the technology is a big burden, but floating solution, even if difficult to install and more pricey, let countries with big water-depths to have offshore wind power production. Japan is an interesting example and its situation will be explained in a more detailed way in the next section.

Further reason for the increasing importance of this field is the big synergy between renewable and Oil and Gas (O&G) fields, regarding the development of deep-water offshore Research and Development (R&D). The maturity of this sector contributed in the growth of offshore wind power: a good hint for a transition from fossil fuels to renewable energies.

1.2 Deep-water Offshore Platforms

1.2.1 Main Platform Concepts

The work that is going to be explained is focused on floating structure, so a brief introduction to the different type of floating platform for wind application will be illustrated.

As explained in Castro-Santos et al. [4], among offshore platforms, three different types can be distinguished:

- *Ballast-stabilized, sparbuoy*: also called SPAR platforms, whose stability is ensured by heavy ballasts to lower the center of gravity below the center of buoyancy. The platform keeping is provided by mooring lines.

- *Buoyancy-stabilized, barge*: also known as semi-submersible. It's one of the main concept of platform since 1960s in O&G industry. The stability, especially in wave condition, is a mainly provided by the multi-bodied setup and its ballasting: the ballasting can give different option to counteract with the motion of the platform.

- *Tension Leg Platform, TLP*: the structure is floating and stabilized because of tendons which act as mooring system. The stiffness of the tendons is the parameter that affects the motion of platform. As far the motion is restricted a better performance of the wind turbine is warranted. The tendons are fixed to the seabed through suction buckets.

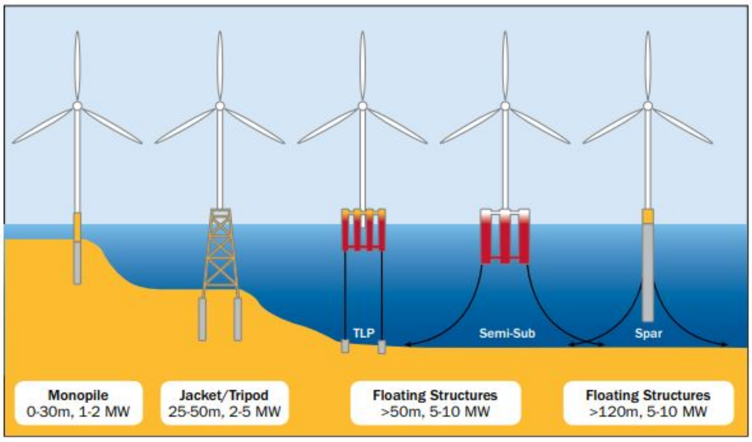

Figure 1.2: Offshore wind turbines for shallow-water and deep-water applications explained in Gao et al.[8].

1.2.2 Platform Motions

The motion of a Floating Offshore Platform is mainly induced by current and waves. Once a wind turbine is installed, even the wind turns into an important factor for the motion of the platform.

The displacements obtained, as shown in Figure 1.3, can be characterized according to the six degrees of freedom (6DOF) of the rigid body, which in naval engineering are named as:

- *surge*, motion in the direction parallel to the sea current (*inline direction*);
- *sway*, motion in the direction perpendicular to the sea current (*transverse direction*);
- *heave*, motion in the direction normal to the water-line;
- *yaw*, rotation of the body around the axis normal to the water-line and passing through its center of gravity;
- *pitch*, rotation of the body around the axis parallel to the transverse direction and passing through its center of gravity;
- *roll*, rotation of the body around the axis parallel to the inline direction and passing through its center of gravity.

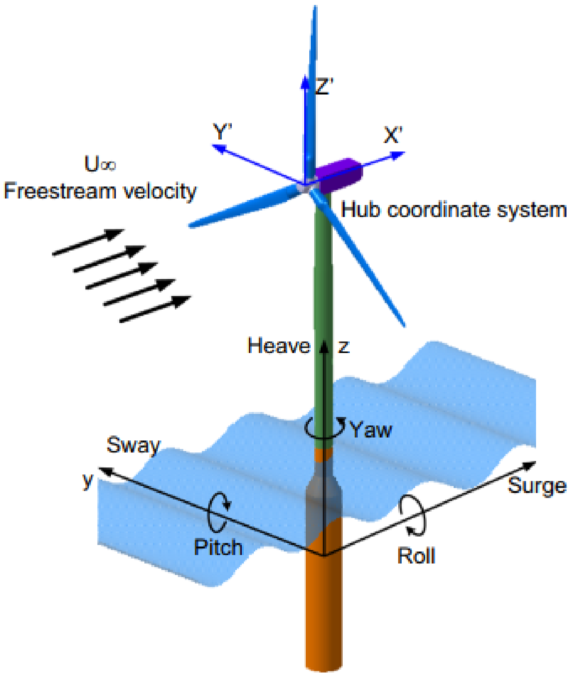

Figure 1.3: Platform 6DOF modes of motion

1.2.3 Spar platform

As case study of the following work, a brief description of the full-scale spar platforms, or *"sparbuoy"* concept will be illustrated.

This kind of platform is similar to a slender cylinder and its stability is provided by the application of ballasts to lower the center of gravity below the center of buoyancy.

The sea-keeping is ensured by a mooring system attached to the hull of the cylinder. The geometric symmetry and simplicity are favourable from both an economical and hydrodynamic point of view: its hull shape reduces the motion of the structure and involves a lower manufacturing cost. On the other hand the hull entails high drag forces and the FIM phenomenon, studied and discussed in Section 1.3, caused by the sea currents. Inline and transverse motion of a spar become relevant when FIM is verified.

According to Table 1.1, large differences in motion compliance are noticed in different concepts of platform.

Motion Compliance of Platform					
Platform	**Stability**	**Sway & Surge**	**Heave**	**Pitch & Roll**	**Yaw**
Spar	Ballast	C	C	C	C
Barge	Buoyancy	C	C	C	C
TLP	Mooring	C	R	R	C

Table 1.1: Platform types according to their stability and motion compliance shown in Castro et al.[4]. "C" stands for compliant modes and "R" for restrained modes

Spar platform are mainly used for deep-water applications; the simplicity of the manufacturing is the key point of this concept, whilst the installation does not reflect the same situation. Deep-water means longer mooring lines and the geometry of the structure implies more complexity in transportation and installation phase.

Figure 1.4: Aasta Hansteen spar platform transported by semi-submersible vessel from South Korea (manufacturing place) to Norway (installation place). Source: Equinor

1.3 Offshore Wind Energy in Japan

1.3.1 Energy Plan: antefact and objectives

After Fukushima Daichii NPP accident in 2011, Japan started a process of decommissioning of nuclear power plants in the territory. Consequently, increase in Liquefied Natural Gas (LNG) import occurred to meet the energy demand of the country.

Importing fossil fuels from Middle-East and Russia implied an increasing risk in energy safety. Japanese government realized the gravity of the problem, starting several projects involving renewable energy sources, from solar to wind.

Consequently to what explained before, the Japanese Ministry of Economy, Trade and Industry (METI) set three targets to pursue for 2030:

- Raise Self-Sufficiency rate: reducing the imports of sources for energy production.
- Lower the cost of electricity: re-powering nuclear power plants and improving coal thermal power generation.
- Reduce CO_2 emission: increasing the share of renewable and nuclear sources.

1.3.2 The Japanese Case: current situation

Wind power is one of the most prospective sector, and the increase in capacity is one of the reason of the big wind potential of Japan territory.

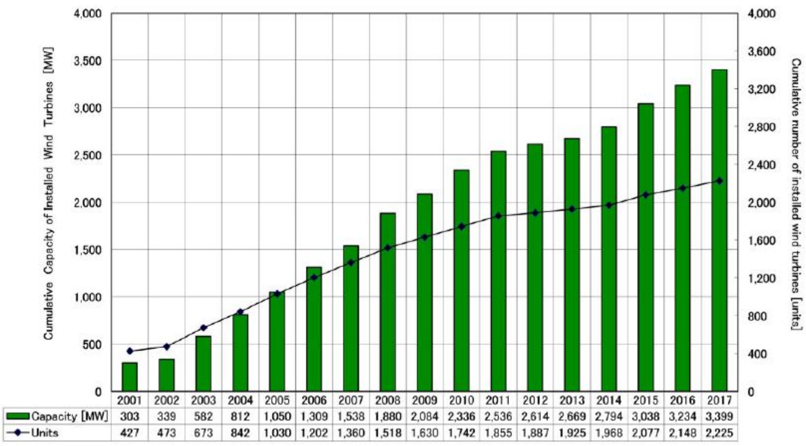

Figure 1.5: Cumulative wind turbines capacity and number of units installed in Japanese territory according to IEA Wind Report [33]

The morphology of Japan's territory puts it into a very unique condition. The Honshu island is the most mountainous part of the countries, while Kyushu and Hokkaido islands are more plane and with the biggest wind potential.

As highlighted in the IEA Wind 2017 Annual Report [33], a mismatch between wind resource locations and energy demand affects Japan. Northern areas are the less populated and with the lowest grid capacity, but the biggest wind potential. Opposite situation is for Honshu island, in which the wind potential is lower because of the lack of land where to install power plants, and the highest energy demand and density of population. Furthermore, the Japanese seismic area is mainly affecting the high wind potential areas: further complexities in design phase and regulation would be added. This is a reason why Japan is investing in offshore technology for wind energy production.

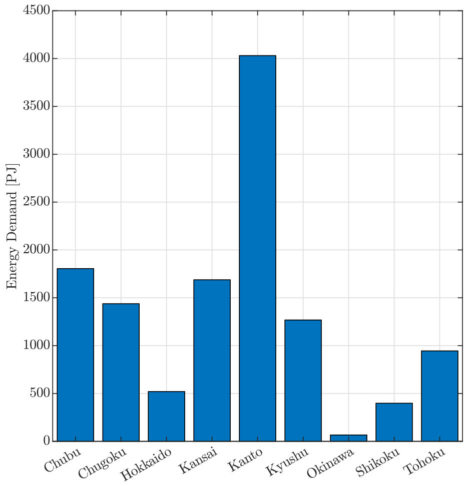

(a)

(b)

Figure 1.6: Energy demand for electricity by region according to Otsuka et al. [18] (a) and Japan map (b)

Furthermore, not all offshore applications can be considered the best options for Honshu area. As shown in Figure 1.8, the water depth around Japan is very high: this implies the utilization of deep-water solutions.

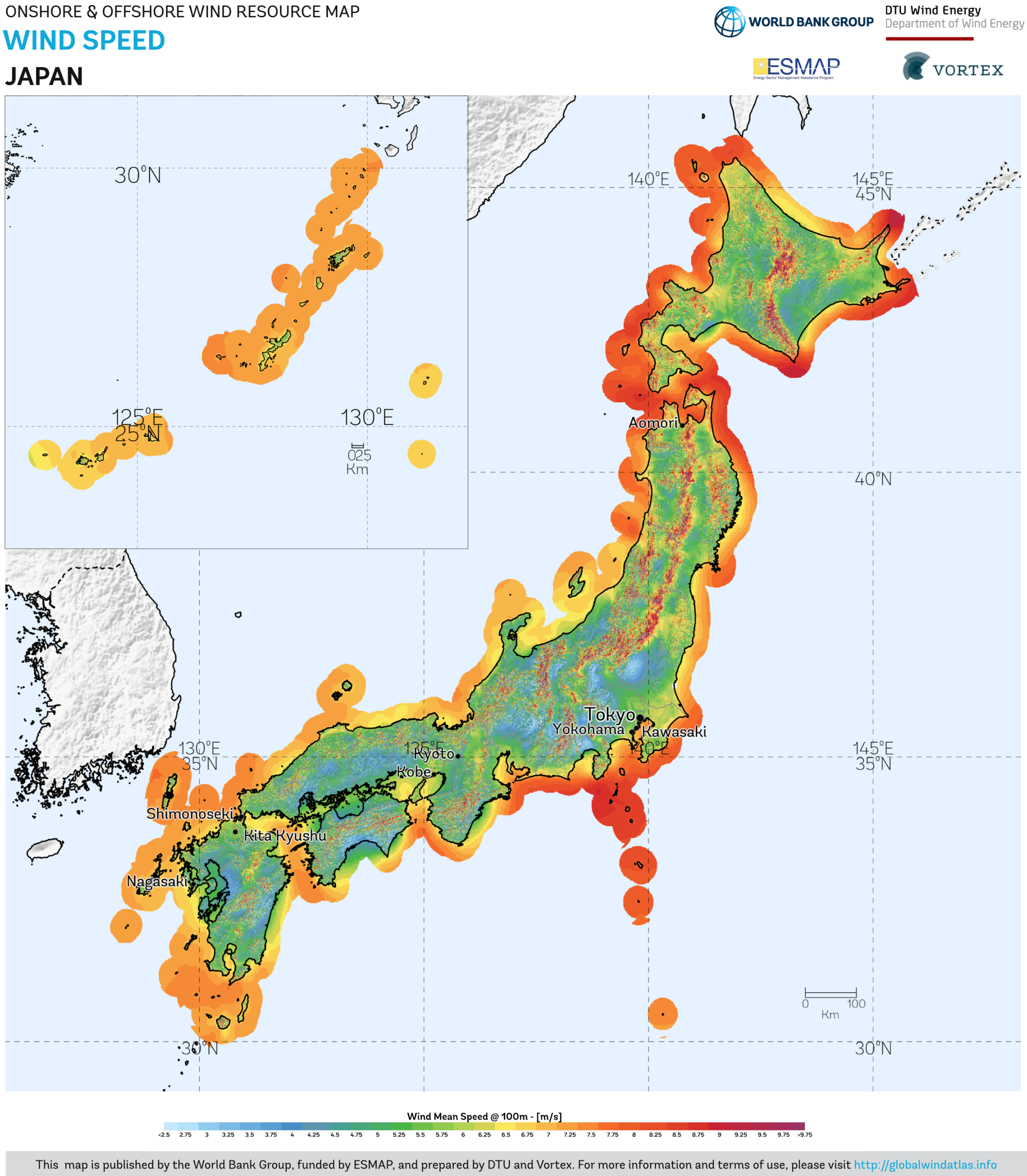

Figure 1.7: Japan wind potential calculated by the Wind Atlas Tool[17]

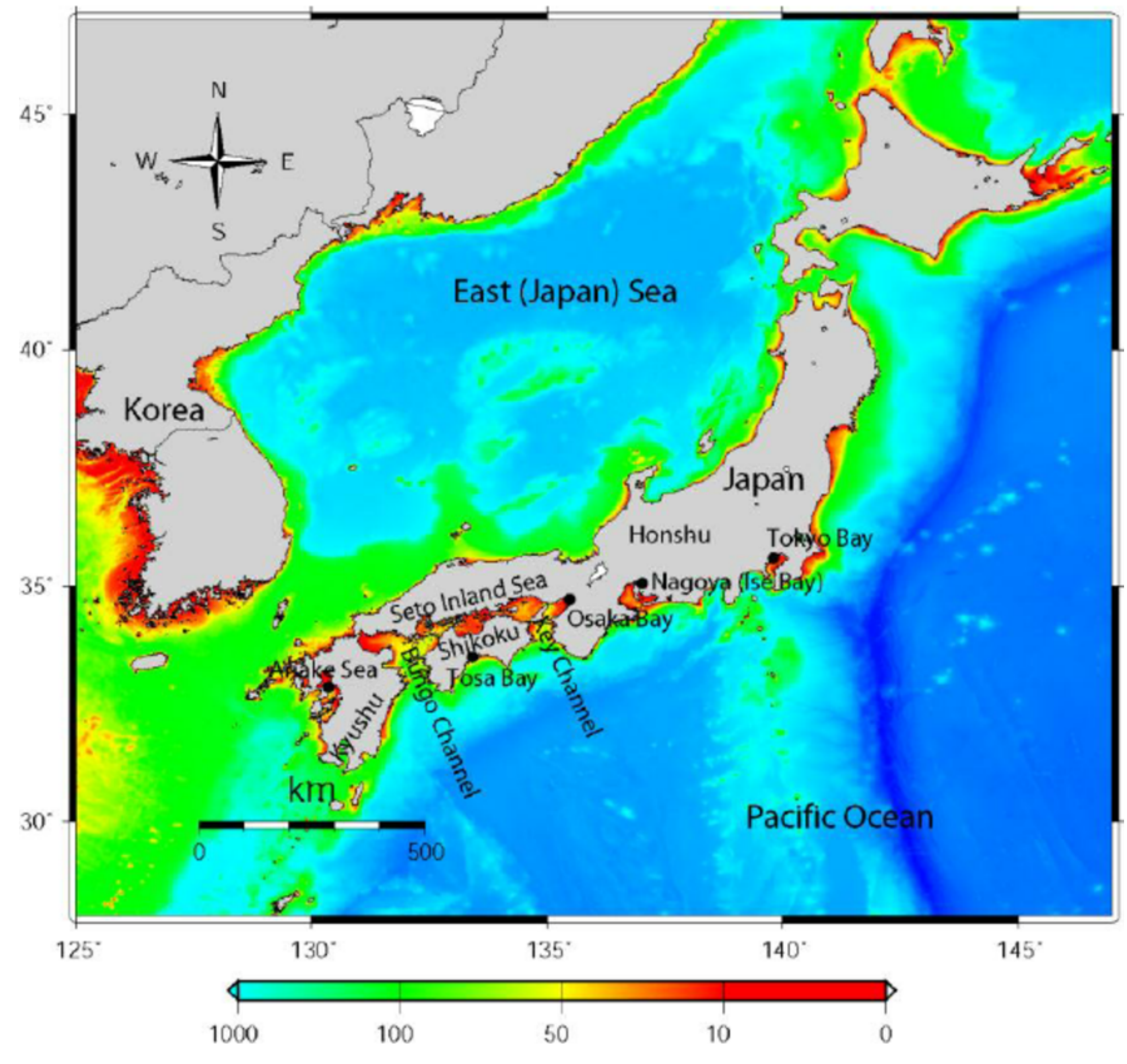

Figure 1.8: Japan seabed depth according to Lee et al.[16]

1.3.3 Future Projects

The synergy between Japan and Floating Offshore Wind Turbines (FOWT) technologies appears to be clear because of the high offshore wind power potential which could reach 1.6 TW.

According to the METI objective for the reduction in the cost of electricity, the R&D groups involved in this projects, like New Energy and industrial technology Development Organization (NEDO), are mainly trying to figure out a reduction in capital expenditure (CAPEX) and operative expenditure (OPEX). As long as costs related to manufacturing and installation are high, the technology development and application will be slowed.

Especially for Japan, the installation, moorings and anchors costs, shown in Figure 1.9a, are underestimated as the main applications in offshore wind field are deep-water.

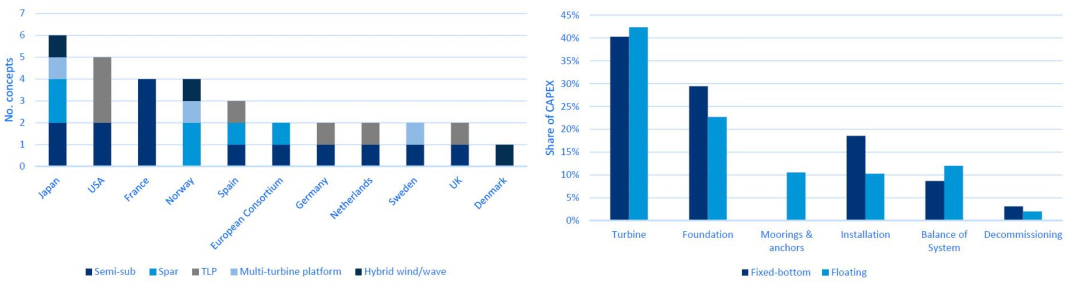

(a) **(b)**

Figure 1.9: Geographical origin and typology of floating wind platform concepts (a) and cost breakdown per component for typical fixed-bottom and floating offshore wind projects (b) according to the Carbon Trust Technical Report [27]

Furthermore, Japan is mainly investing and researching on spar platform concept (see Figure 1.9b). The reason is arisen to balance the high cost of installation with the low cost of manufacturing associated to this concept.

Chapter 2

Literature Review

Flow-Induced Motion phenomenon, as explained in Fujarra et al.[7], is group of phenomena related to the fluid-structure interaction. It affects most part of floating offshore platforms concepts, in presence of sea current and waves. This phenomenon is categorized in several different behaviours as shown in Figure 2.1.

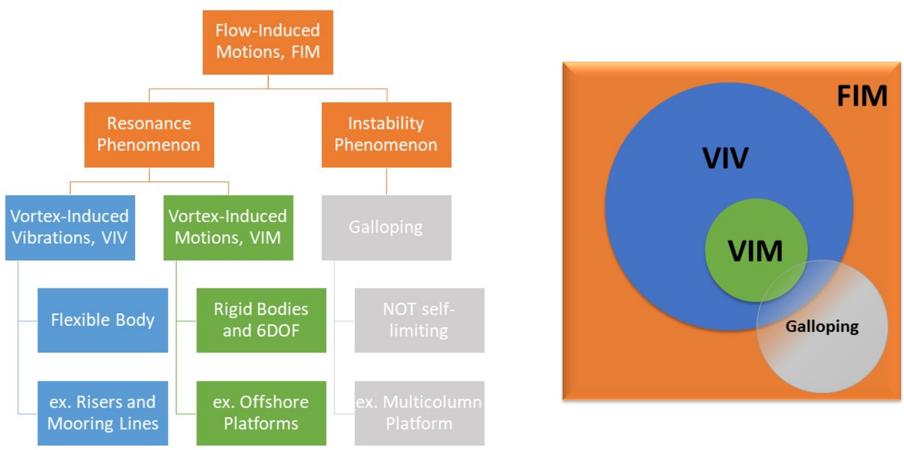

Figure 2.1: Diagram describing Flow-Induced Motion phenomena

Three different phenomena can be identified: Vortex-Induced Vibration (VIV), Vortex-Induced Motion (VIM) and galloping. VIV is affecting flexible and high aspect ratio bodies, whilst VIM mainly rigid bodies: these phenomena manifest as resonant behaviour, which is a result of compensation between energy delivered by the fluid to the structure and energy dissipation by hydrodynamic damping on the structure. On the other hand, galloping is only related to the instability of the platform and affects barge platforms. This phenomenon will not be explained according to the type of platform analyzed and the aim of the work.

The current chapter is summing up the background and the theoretical knowledge of the phenomenon, the parameters that characterize it and the goal of the present work.

2.1 Flow-Induced Motion

2.1.1 Genesis and background of the phenomenon

A glance on this phenomenon has been given for the first time on spar platforms in the Gulf of Mexico. As reported in Smith et al.[23], in the water of the Gulf of Mexico loop currents are present: large eddies are generated with a frequency six to twelve months, increasing the current speed. As water flows past the cylindrical structure of a spar platform, water viscosity causes flow separation and periodic shedding of vortices downstream the structure. In case the frequency of the shedding and the motion of the structure would match, a resonant peak in the transverse and inline direction is induced.

Consequently to the unexpectedly large value of the transverse amplitude, different concerns arose:

- *Fatigue issues*: fatigue damage accumulates during this kind of events, significantly decreasing the life-time of mooring system components like chain and fair-lead.

- *Link-to-link wear*: wear in chain and fair-lead due to cyclic frictions acting on their surfaces.

In case of underestimation of this phenomenon, component cannot respect the expectation in life-time regarding mooring system components.

2.1.2 Vortex shedding

Vortex shedding is a phenomenon related to the interaction between bluff bodies (like a spar) and a steady viscous fluid flow (like sea current). As explained in Blevins [3] for a cylinder, close to the widest section of the body two boundary layers separate from each side of the surface of the structure creating two layers. As the innermost portion of the layer is much slower than the outermost one, the free layers tend to roll up creating swirling vortices in the wake. The fluid flow creates a pattern of alternating low-pressure vortices on the downstream side of the object (see Figure 2.2a and Figure 2.2b). These vortices originated for Reynolds number, Re $40 < Re < 3 \cdot 10^5$ are called von Kármán vortices, whose main characteristic is the periodic shedding downstream a bluff body. Pressure forces will act on the object moving it towards the low-pressure zone.

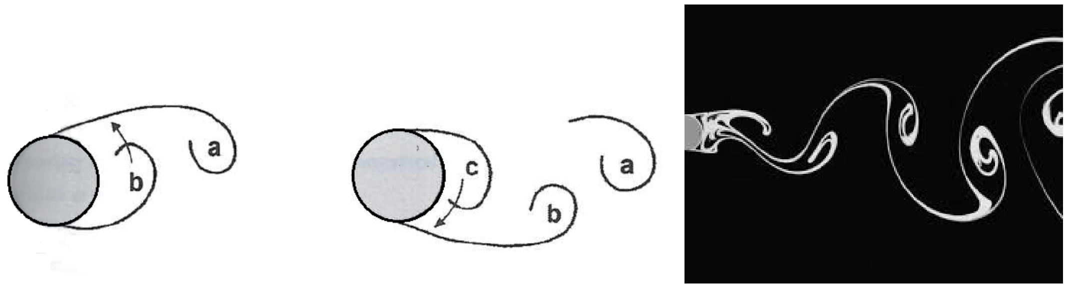

(a) **(b)**

Figure 2.2: Sketch (a), by Stappenbelt et al.[24], and PIV visualization (b), by van Dyke et al. [28], of vortex shedding mechanism

The frequency of shedding, f_S, of these vortices is proportional to the velocity of the flow, U, and the characteristic length of the body, D, in case of a cylinder is the diameter.

$$f_s = St \cdot \frac{U}{D}$$

The proportional factor is a non-dimensional parameter named as *Strouhal number*, St.

The Strouhal number is strongly dependent on the *Reynolds number*, Re which represents the ratio of inertial to viscous forces. The Reynolds non-dimensional parameter gives information regarding the flow regime and, according to Kozakiewicz et al.[15], different pattern, also called *vortex street* (see Figure 2.3), and frequencies of the vortex shedding are observed while changing the flow characteristics.

Furthermore, vortex shedding induces oscillation in lift and drag forces: the former with a zero mean value, whilst the latter with a non-null value. Vortex shedding mechanism is the excitation that triggers the FIM phenomenon on floating structures: when the frequency of the vortices matches with the frequency of the structure motion, kept in position by the moorings restoring force, resonance between the two mechanisms is verified. The flow velocity range in which this synchronization occurs is called *synchronization range* and it is manifested as large displacements in both inline and transverse direction, with transverse amplitudes double the inline one.

According to what explained at the beginning of the present Section, the FIM phenomenon is a macro-category which can be identified and distinguished in two different resonant behaviours: VIV and VIM.

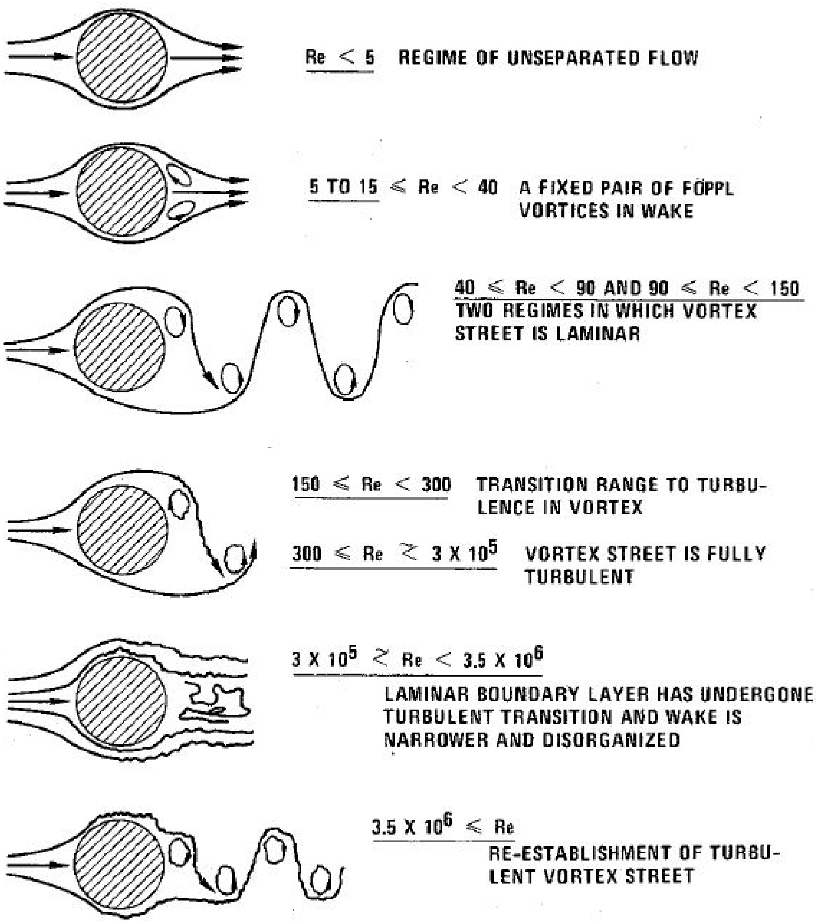

Figure 2.3: Regimes of fluid flow across smooth circular cylinders and their relative vortex streets from Blevins et al. [3]

2.1.3 Vortex-Induced Vibration

Vortex-Induced Vibration phenomenon is classified as a result of fluid-structure interaction due to vortex shedding on flexible bodies with high aspect ratio, like risers or mooring lines in real systems. As a consequence a self-limited and self-excited behaviour, because of the resonance between frequency of the vortex shedding downstream the structure and its natural frequency of the motion, occurs and it induces large resonant forces on the components that cannot be neglected.

The resonance is triggered by the vortex shed downstream the element and the region in which the activation of the phenomenon is referred as *synchronization range*, which would be described later on this Section.

Several non-dimensional parameters are derived in order to identify the VIV phenomenon. *Reynolds number*, *Re*, is fundamental parameter to identify the flow characteristics and the vortex shedding appearance. It is defined as the ratio of inertial to viscous forces:

$$Re = \frac{\rho U D}{\mu} = \frac{UD}{\nu} \tag{2.1}$$

where ρ, μ and ν are, respectively, density, viscosity and cinematic viscosity of the fluid, U is the velocity of the fluid flow and D is the characteristic dimension of the immersed body. von Kármán vortex street takes place in the wake of the cylinder for $Re > 40$.

The frequency of the shedding is strongly related to the flow regime and directly proportional to the flow velocity. According to these features, *Strouhal number*, *St*, is the non-dimensional parameter investigated for a better understanding of the shedding frequency. Equation 2.3 shows the relation among those characteristics:

$$St = f_s \frac{U}{D} \tag{2.2}$$

where f_s is the frequency of the vortex shedding.

Strong relationship between *St* and *Re*, and several correlation between them has been formulated by Williamson [32], for low *Re* numbers, and Roshko [20] and Schewe [22] for higher values of *Re*. The relationship between these parameters is shown in Figure 2.4.

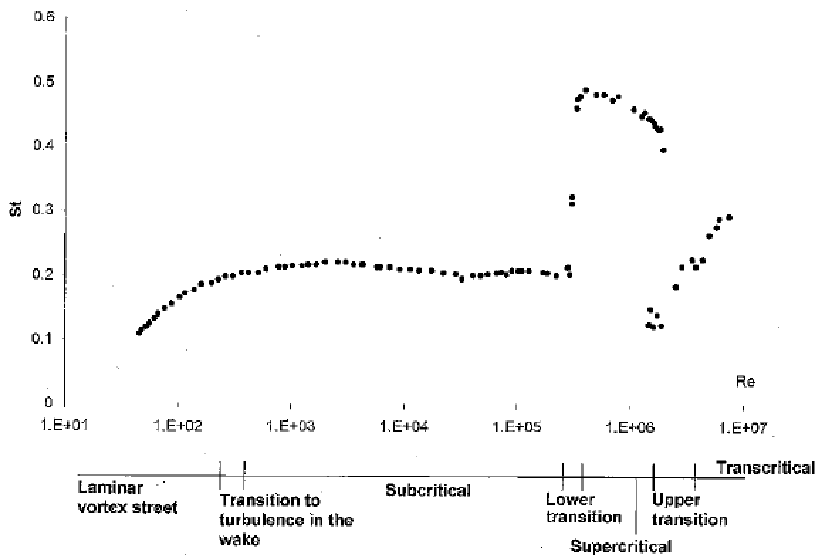

Figure 2.4: Relation between Strouhal and Reynolds number derived by Stappenbelt et al. [24]

Another important parameter is the *reduced velocity*, U_r, which is defined as the normalization of the current velocity with the natural period of the transverse motion in still water and the characteristic length of the body or model considered:

$$U_r = \frac{UT_n}{D} \tag{2.3}$$

where T_n is the natural period of the transverse motion in still water.

The natural period is derived through a decay test, which is described in Chapter 4, and then used to derive this parameter. The range of reduced velocities for spar platforms is generally $3 \leq U_r \leq O(10)$ according to Fredsoe et al. [5].

According to the work of Williamson et al. [31], the response of the VIV phenomenon consists on a linear increase of the frequencies of the shedding while increasing the flow velocity. This implies, according to Eq. 2.3, an approximately constant St in a wide range of Re.

In case of cylinder free to move in 2DOF, in a certain range of U_r the frequency of the displacement can match with the frequency of the shedding, resulting in a resonant motion affecting both the inline and the transverse displacements. This phenomenon can be defined as *self-excited* and *self-regulated*, as after a certain range of reduced velocity a desynchronization between the to frequencies occurs and the resonant behaviour disappears.

In order to generalize the behaviour for different size of cylinder, a non-dimensional amplitude is derived as the normalization of the displacements with the characteristic length of the structure, which is diameter for a cylinder. The non-dimensional amplitude can be distinguished as:

- *Inline*, which is the non-dimensional amplitude $\frac{X}{D}$
- *Transverse*, which is the non-dimensional amplitude $\frac{Y}{D}$

Figure 2.7, shows a typical VIV response for fixed cylinder.

Furthermore, as described in literature, the aspect of the body is fundamental for the study of the phenomenon, so it implies the introduction of the *aspect ratio*, A_R. This value is characterizing the response of the structure motion, according to different types of vortices that could occur. The aspect ratio is defined as the quota of immersed length over the characteristic length of the body:

$$A_R = \frac{L}{D} \tag{2.4}$$

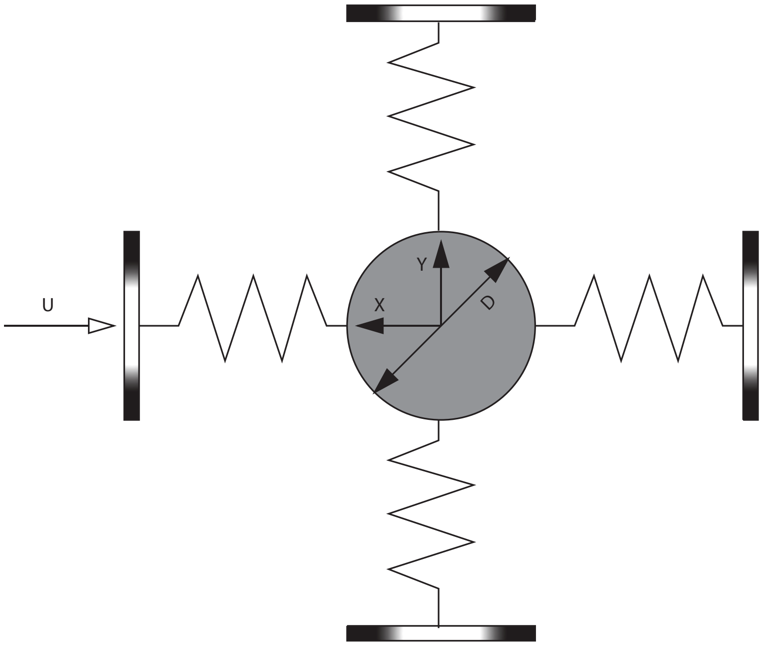

Figure 2.5: Sketch of experimental configuration

The change of this parameter influences size and number of the vortices downstream the body.

According to Pattenden et al. [19], different types of vortices are acting on the body and these can be classified as follows:

- *von Kármán*
- *tip vortex*;
- *arch vortex*;
- *horseshoe vortex*;
- *trailing vortex*.

The vortices previously listed are mainly originated on the side of the cylinder (see Figure 2.6). Other vortices are acting according to the A_R and also the free-end of the body is affected, according to Kawamura et al. [13].

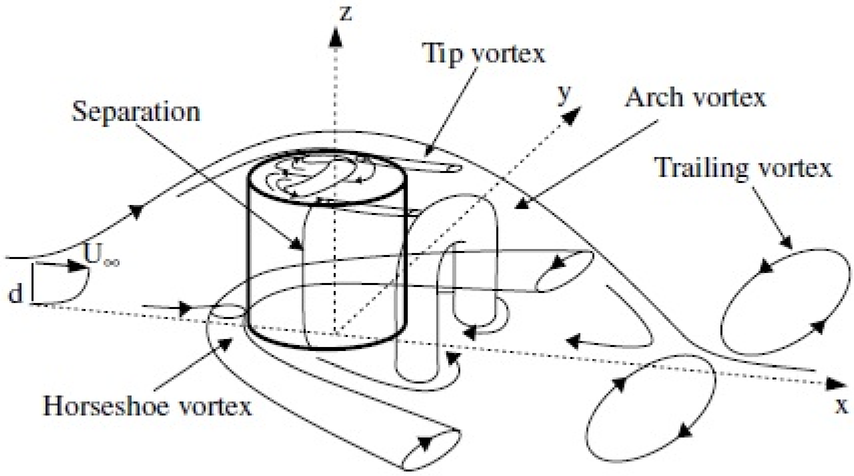

Figure 2.6: Type of vortex shed from a cylinder according to the work of Pattenden et al. [19]

The *mass ratio*, m^*, is also representing a factor to take into account while studying the VIV. This parameter stands for ratio between the structural mass of the body and the mass of fluid displaced. In the cylinder case:

$$m^* = \frac{4m}{\rho D^2 L \pi} \tag{2.5}$$

where L is the immersed length of the cylinder. In the case of floating structure $m^* = 1$, as in this case the mass of fluid displaced is equal to the structural mass.

According to the work of Stappenbelt et al. [25], for low mass ratio ($m^* < 6$), the main direction of the resonant displacement are both inline and transverse for cylinder in 2DOF motion. Whilst, for higher mass ratio, the phenomenon is mainly affecting the transverse direction.

Figure 2.7 from Williamson et al. [31], shows a typical VIV response for fixed cylinder, $m^* = 2.6$ and $L/D = 10$ free to move in 2DOF. Several branches are present in the response that can be mainly distinguished as *higher branch* (SU), in which largest amplitudes are encountered because of the resonant behaviour of the motion, and a *lower branch* (L) in which the synchronization between motion and vortex shedding is completely mismatched. The synchronization range is clearly defined in the range of $4 < U_r < 8$, as the frequencies is increasing linearly with the reduced velocity according to the definition of synchronization range. This behaviour results in a match between the frequency of the body motion with consequent resonant behaviour.

According to the aim of this work, the case is related to low mass ratio body, whose amplitude response is expected to result as in Figure 2.8.

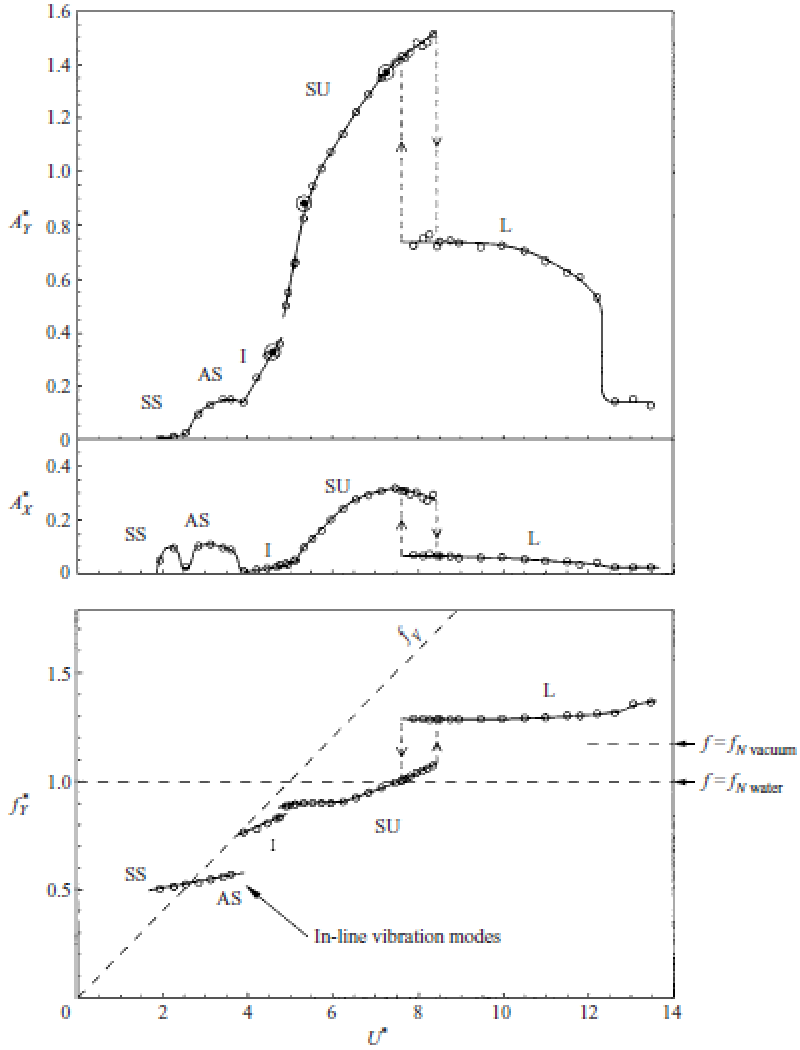

Figure 2.7: Characteristic amplitude for low mass ratio, high aspect ratio cylinder, and transverse frequency of the motion

Mainly, this parameter is associated to the *damping ratio*, ζ, which is the ratio between the viscous damping coefficient and the critical damping, identifying a further parameter $m^*\zeta$. The ζ is defined as shown in Eq. 2.6:

$$\zeta = \frac{c}{2m\omega_n} \tag{2.6}$$

The damping ratio is, approximately, dependent to a logarithmic decay, shown in Eq. 2.7:

$$\delta = ln\left(\frac{y_n}{y_{n+1}}\right) \tag{2.7}$$

where the y_n and y_{n+1} represent the first two oscillation peaks of the decay curve. The higher the $m^*\zeta$ parameter is the lower values of maximum amplitude

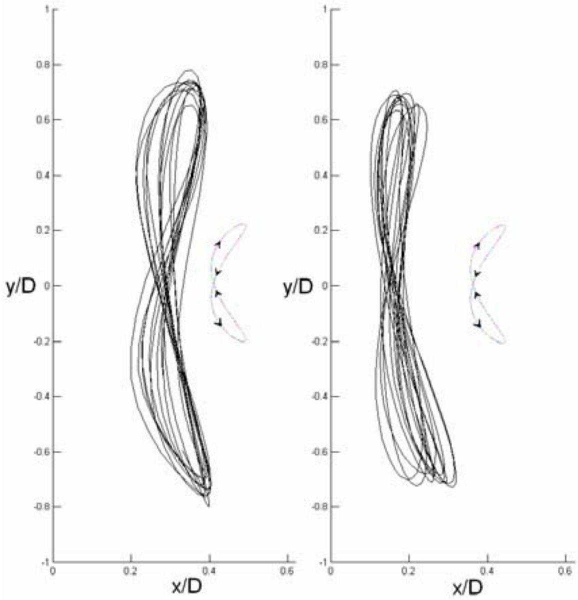

Figure 2.8: Trajectory for low mass ratio, $m^* < 6$, (left) and high mass ratio, $m^* > 6$(right) values

are encountered.

VIV can be distinguished from VIM, according to the difference in the frequency response of the structure when excited by the vortices.

2.1.4 Vortex-Induced Motion

Vortex-Induced Motion phenomenon can be considered as a particular case of VIV. According to the work of Fujarra et al. [7]. VIM is verified in case of cylinders with low aspect ratio, low mass ratio, high Reynolds number and at least 2DOF, as shown in Figure 2.9.

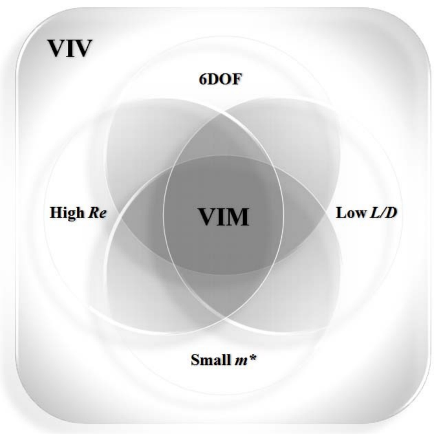

Figure 2.9: Scheme of difference between VIM and VIV by Fujarra et al. [7]

As a consequence a self-limited and self-excited behaviour, because of the resonance between frequency of the vortex shedding downstream the structure and its natural frequency of the motion, occurs and it induces large amplitudes of motion on the platform.

The difference in response between VIV and VIM is mainly related to the frequency of the motion and the displacement. In VIM case, according to the small aspect ratio involved, the displacements are larger and consequently lower frequencies of motion for the structure. Typical response for VIM case is shown in Figure 2.10, highlights only one branch in the response, with no *lower branch* for high reduced velocity range, as verified in VIV case.

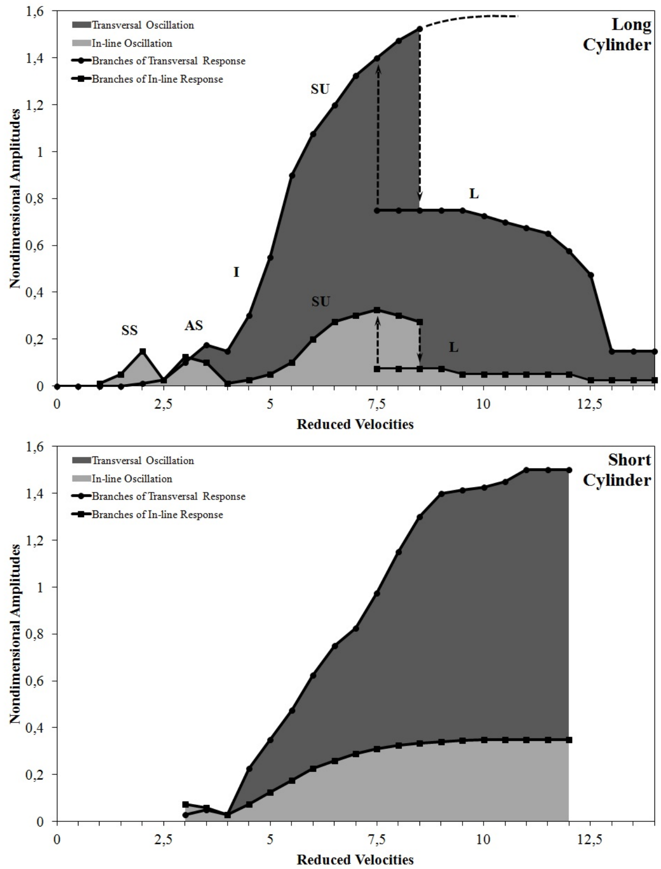

Figure 2.10: Inline and transverse amplitude response in VIV (upper) and VIM (down) case

The present work, in the full scale, can be compared to monocolumn platforms, which are consistent with the definition of the VIM phenomenon, as stated in Gonçalves et al. [10], as the model parameters are the one defined in Table **??**

Furthermore, it is important to set a definition for the *synchronization range*. This range can be evaluated through the Power Spectrum Density (PSD) analysis of the motion in the inline and transverse direction. As investigated in Gonçalves et

VIM characterizing parameters		
Mass Ratio	m^*	1
Reynolds Number	Re	10^7
Aspect Ratio	A_R	1.5
Degrees of Freedom	DOF	$6DOF$

Table 2.1: Parameters characterizing VIM for the present case in full scale

al. [11], the synchronization range for cylinder $m^* = 1$, $A_R = 1.5$ and 6DOF can be deduced from Figure 2.11. According to the work previous cited, comparing Figure 2.10 and 2.11 it can be seen that in the range of high PSD values the amplitudes of motion are increasing: this behavior can be relate to the start of a synchronization range, in this case defined for $U_r > 5$, with no sign of desynchronization.

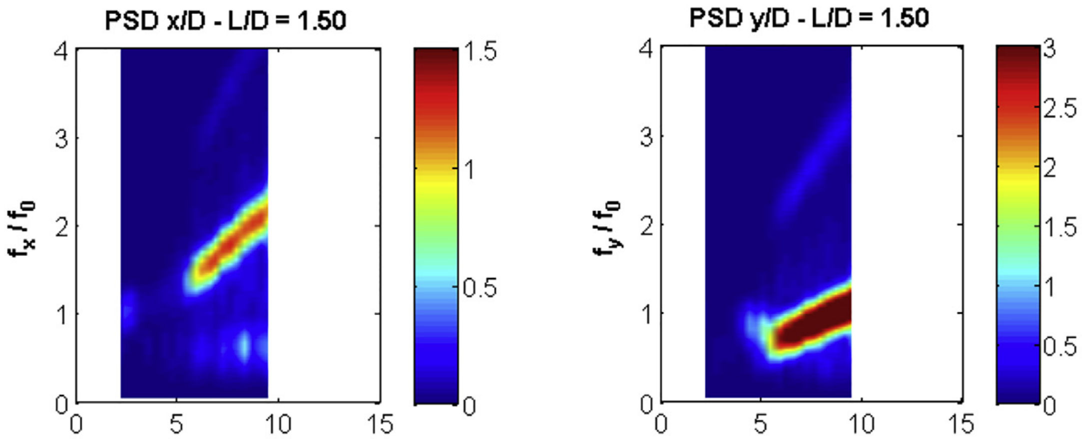

Figure 2.11: PSD of the motion in the inline and transverse direction for floating cylinder $A_R = 1.5$, resulted from the work of Gonçalves et al. [11]

2.1.5 Mitigation

After decades of investigation, several ways to mitigate the phenomenon were carried on. The different mitigation methodologies, as stated in Fredsoe et al. [5] are classified according to the parameters controlled:

- Reduced velocity: using active control systems to change the natural period of the motion (Kokkinis et al.[14]) or changing the design of platform, i.e. diameter for a spar, in other to delay as much as possible the synchronization region.

- Mass and damping: increasing the mass of the structure and the damping reduce or avoid the FIM phenomenon. Side effects on the natural frequency of the motion must be taken into account.

- Vortex shedding: protuberances on the surface of the structure will modify the pattern of the vortices and also their effect on the structure. This is a consequence of a modification of the boundary layer around the object. As shown in Figure 2.12, several different technologies has been studied and applied in the offshore field: strakes, fins, fairings, spoiler plates and so on. Spoiler plates so far is the less studied and it will be important element in the present work.

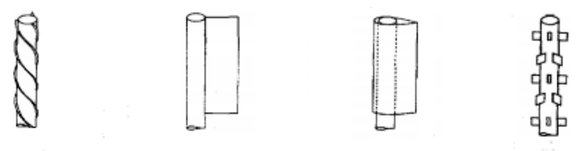

Figure 2.12: Vortex shedding mitigation devices: (from left to right) strakes, splitter plate, fairings and spoiler plates [3]

According to the past work of Gonçalves et al. [10], relevant reduction in both inline and transverse amplitude occurs when the spoiler plate device is implied in the mitigation. As shown in Figure 2.13, the amplitude are reduced in the range of high reduced velocities, whilst slightly increased in the low reduce velocity range. Very interesting is the fact that the amplitudes in the synchronization range are considerably reduced.

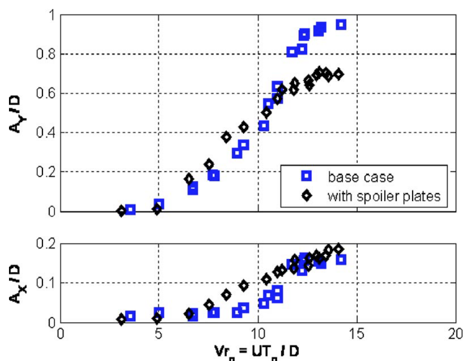

Figure 2.13: Transverse (up) and inline (down) response for a monocolumn platform tested in the work of Gonçalves et al. [10], considering the application of spoiler plates for mitigation purpose

2.2 Present work objectives

According to the different platform concepts, some mitigation devices could be feasible or not. In the past years, strakes has been the most applied device for the sake of vortex mitigation. The vortex shedding was successfully mitigated, but, as deduced by Fredsoe et al. [5], an increase in the drag forces on the structure had been noticed; furthermore, the installation of this device is very complex and costly, especially for low aspect ratio cylindrical platform, because of the very low tilt angle of the helix that would be designed to fit on the surface. In the offshore scenario, the low aspect ratio cylinders have attracted attention due to the increasing size of the circular platform. This structure can be classified as bluff bodies and the fluid-dynamics related is object of interest of several works in literature. These are reasons to investigate in other directions using other types of devices and the starting point of the present work.

According to the lack of studies in literature, the spoiler plates are the objects of study for the present thesis. In order to study the effect of the spoiler plates configuration, a spar platform is the target for the mitigation device, according to the simplicity of the structure shape and the better feasibility in construction phase. Additionally, the flow around cylinder is one of the biggest interests in research papers for both experimental tests and Computational Fluid Dynamics (CFD) calculations, so that characteristics of the flow and the vortices are well-known.

The aim of the work is targeting the implication of spoiler plates on a spar platform considering the mitigation effect that is implied. The work consists in performing a parametric study, whose goal is to find the parameter that most affects the mitigation the Flow-Induced Motion. The parameter chosen are *configurational* parameter that would characterize the disposition of the plates on the platform surface. In addition, an investigation on which is the Most Improved configuration (MIC) choosing among the parameters selected.

As presented in Antony et al. [2], mitigating the FIM and quantifying the motion will decrease the cost prediction and will contribute to an increase in the fatigue life of the components of the mooring system.

Chapter 3

Analysis Methodology

The experiment carried out in the towing tank gave the opportunity to understand the effect of the spoiler plates on the FIM mitigation. In order to investigate the mitigating behaviour of the device, the FIM response has been analyzed through the non-dimensional amplitudes, frequencies in inline and transverse direction and the hydrodynamic forces.

Although the motion of the platform is free in 6DOF, the inline and transverse motions are the most relevant displacement for the platform. Heave, yaw, pitch and roll motion are not significantly resonant with the vortex shedding, and this explain the choice of 2DOF analysis.

The input for the analysis is the signal produced by Qualisys®, which in post-processing phase is cut in order to exclude part of the signal with large systematic error (see Figure 3.1). The error produced is mainly due to *start and stop effect* of the cart.

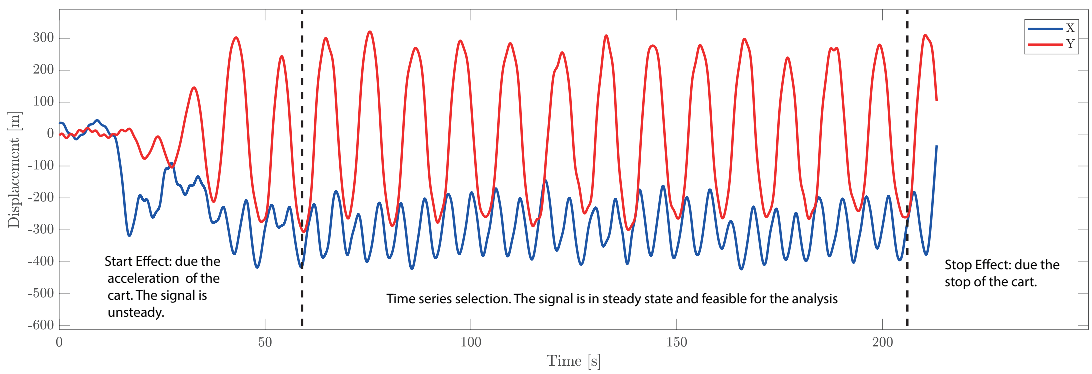

Figure 3.1: Routine for signal processing

Then, in order to assess a parametric study a *base case* configuration is fixed. From the base configuration one parameter is change, to analyze its impact on the phenomenon mitigation, and the other two are fixed. Starting every condition from the base case and changing the parameters gives the idea of which parameter is affecting the phenomenon.

The base case selected is the one with:

- n_D=8;
- n_L=5;
- $A_{R,S}$=1.

Each test of a configuration consists on 25 current condition, in order to compare - through a parametric analysis - the mitigation effectiveness of the parameter changed. Changing the configuration of the plates could imply a change of the natural period of the motion, so a decay test is performed per each case. Preliminary Motion Analysis (PMA) follows each cycle of experiment for a parameter.

In the following diagram (see Figure 3.2) the experimental procedure is schematized.

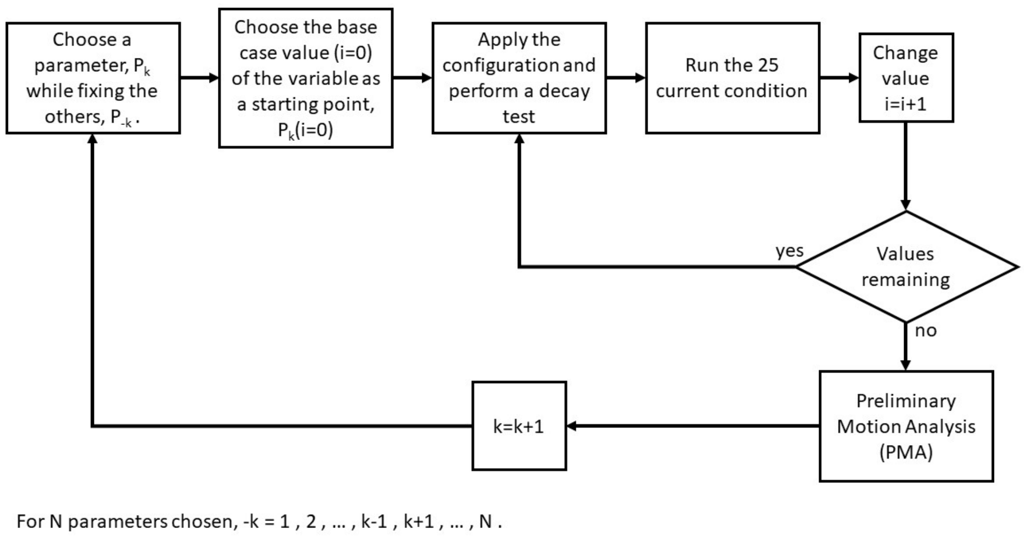

Figure 3.2: Flow chart of the experimental parametric study

Once performed a parametric study, through the data collected in the PMA phase, the best parameter value found from the parametric study is chosen. As far

Spoiler Plates Arrangement Parameters				
Parameter	**Symbol**	**Values**		
Number of Circumferences of Plates	n_L	3	5	7
Number of Plates per Circumference	n_D	4	8	16
Aspect Ratio of the Plates	$A_{R,S}$	0.5	1	2

Table 3.1: Spoiler Plate Arrangement Parameters

the best selection of the parameters is concerned, the procedure is similar to the one explained below, but the best parameter value is always fixed.

The time series of motion (i.e. Figure 4.11) collected by Qualisys® have been post-processed with Matlab®. The result is a parametric analysis for the non-dimensional amplitudes, frequencies and forces acting on the model per each configuration. These values are dependent on the range of reduced velocity investigated. The mitigation effectiveness of the parameter chosen for the spoiler configuration will be clarified. The analysis methodology will be described later on this Chapter.

3.1 Reduced Velocities

The reduced velocity (U_r) is defined as:

$$U_r = \frac{UT_n}{D}, \tag{3.1}$$

where U denotes the incident current velocity, T_n is the natural period of the motion of the platform in the transverse direction in still water, and D is the characteristic length of the body section which is subjected to a vortex shedding, which is the diameter for a spar model.

All the following analysis are compared to the value of reduced velocity in which they are verified. The natural period T_n is calculated from the decay test performed in still water.

3.2 Non-dimensional Motion Amplitudes

The motion is commonly represented in dimensionless values as X/D for inline and Y/D for transverse, where the nominal amplitudes are calculated based on the Root Mean Square (RMS) as:

$$\frac{X}{D} = \sqrt{2}\,RMS(X), \tag{3.2}$$

$$\frac{Y}{D} = \sqrt{2}\,RMS(Y). \tag{3.3}$$

This representation based on the RMS is generally employed to calculate the fatigue of mooring systems. The root mean square was calculated considering any set p of n values measured, as:

$$RMS(p) = \sqrt{\frac{1}{n} \cdot (\, p_1^2 \;+\; p_2^2 + \;...\; + \;p_n^2\,)} \tag{3.4}$$

3.3 Hydrodynamic Forces

The rigid body motion equations for the cylinder in the transverse and inline direction is calculated based on the equations and discussion proposed by Sarpkaya et al. [21], as follows:

$$m\ddot{X}(t) + c\dot{X}(t) + k_x X(t) = F_{Hx}(t), \tag{3.5}$$

$$m\ddot{Y}(t) + c\dot{Y}(t) + k_y Y(t) = F_{Hy}(t), \tag{3.6}$$

where m denotes the structural mass of the platform, C is the structural damping coefficient of the system, K is the stiffness coefficient, F_H are defined as the total hydrodynamic forces acting on the system, and the subscript x and y represents the inline and transverse direction respectively. The previous equations represent a linear model according to what explained in Chapter 3.

In such formulations, the structural components of the force are placed on the left side of the equations, while the hydrodynamic forces, such as the added mass, hydrodynamic damping and other fluid forces, are placed on the right side of the equation. As a result, the hydrodynamic forces in each direction can be estimated indirectly using these equations of motion.

Preliminary, the structural damping was neglected owing to its magnitude compared to the other dynamic forces. Therefore, the hydrodynamic forces were calculated based on the restoring and inertial forces.

Like the amplitudes, the hydrodynamic forces are represented in non-dimensional values. For the transverse direction, the hydrodynamic force is represented as a lift coefficient given by:

$$F_{Hy}(t) = \frac{1}{2}\rho A_f U^2 C_L(t), \tag{3.7}$$

$$C_L(t) = \frac{2F_{Hy}(t)}{\rho A_f U^2}, \tag{3.8}$$

where ρ is the fluid density, A_f denotes the projected area of the immersed body, in relation to the transverse direction to the flow.

Regarding the in-line direction, the hydrodynamic force can be described in two components. The first related to the static component (mean drag coefficient, $\overline{C}_D$), and the second related to the oscillatory component (dynamic drag coefficient, C_{Dd}) given by:

$$F_{Hx}(t) = \frac{1}{2}\rho A_f U^2 C_D(t), \tag{3.9}$$

$$\overline{C_D} = \int_{t_i}^{t_f} \frac{2F_{Hx}(t)}{\rho A_f U^2} dt, \tag{3.10}$$

$$C_{Dd} = \frac{2\sigma(F_{Hx}(t))}{\rho U^2 A_f} \tag{3.11}$$

where t_i and t_f accounts the initial and final time of the selected experimental data, σ is the standard deviation of the signal amplitude.

Approximately, the hydrodynamic force in the transverse direction can be expressed as an harmonic response [29, 21]:

$$\begin{aligned} F_{Hy}(t) &= F_0 \sin(\omega t + \phi) \\ &= F_0 \cos\phi \sin\omega t + F_0 \sin\phi \cos\omega t, \end{aligned} \tag{3.12}$$

where F_0 is the amplitude of the total hydrodynamic force in the transverse direction, ω denotes the angular frequency of the motion, and ϕ is the phase difference between the force and motion.

This fluid force can be represented by two components: one force in phase with the platform acceleration and the other force in phase with the platform velocity. Based on that, the non-dimensional lift coefficient in Eq. (3.13) can be expressed as:

$$C_L(t) = C_a \sin \omega t - C_v \cos \omega t, \tag{3.13}$$

where the total hydrodynamic force in phase with the body acceleration is denoted by C_a, which represents the added mass coefficient and reviewed in Sarpkaya et al. [21]; while the total hydrodynamic force in phase with velocity is given by the damping coefficient C_v.

The added-mass coefficient is estimated on the classical analysis in the frequency domain proposed in Fujarra et al. [6], where the following relation can be obtained:

$$\frac{\text{fft}\,[F_{Hy}(t)]}{\text{fft}\,[\ddot{Y}(t)]} \approx -m_a(\omega) + \frac{iC_v(\omega)}{\omega}, \tag{3.14}$$

where fft[ ] represents the fast-Fourier-transform operator. Therefore, the added-mass coefficient is obtained by:

$$C_a^{FD} = C_a^{FD}(\omega) = -\frac{\Re\left\{\frac{\text{fft}\,[F_{Hy}(t)]}{\text{fft}\,[\ddot{Y}(t)]}\right\}}{m}, \tag{3.15}$$

where $\Re\{\ \}$ is the real part of the complex number obtained via Fourier transform. The added mass coefficient was taken from the frequency which contains the highest energy.

3.4 Frequency Analysis

The last step of the analysis is to identify which is the synchronization range between the vortex shed and the motion of the platform. According to the work of Gonçalves et al. [11], for bluff floating cylinder, 6DOF motion, aspect ratio L/D=1.5 the Strouhal number is St=0.1.

The frequencies of the motion are calculated from the power spectrum density PSD of the oscillation of the platform in current condition. The frequencies are calculated with Welch method [30], as a lower computational cost for the Fast Fourier Transform (FFT) is expected.

The plot derived will show clearly in which reduced velocity range the FIM is activate, according to a synchronized behavior between vortex shedding and motion, or the phenomenon is desynchronized. The FIM behaviour will appear in the peaks of the PSD of the motion. According to Gonçalves et al. [10], this range is expected

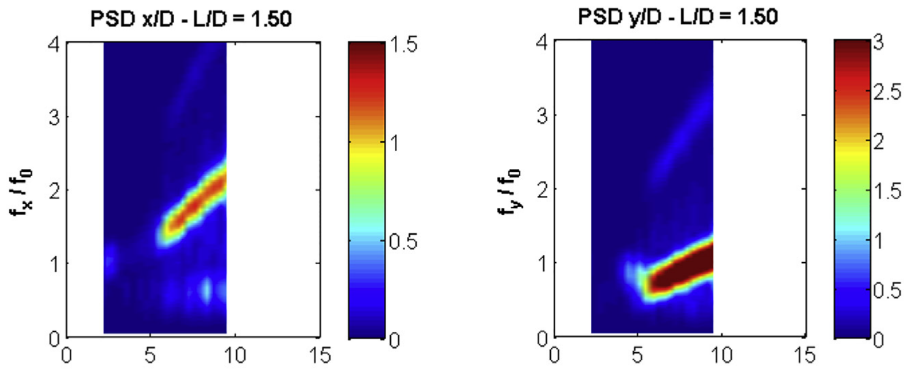

Figure 3.3: PSD analysis, from the work of Gonçalves et al. [11], of the inline (left) and transverse (right) motion for cylinder with A_R=1.5 and m^*=1

to change when the plates are applied on the model surface: the aim of the analysis will highlight for which arrangement of the plates this ranges are changing the most and with mitigating benefits.

The PSD will be shown as a normalization between the analyzed case and the peak value of the *No Spoiler* case, in order to highlight the improvement in the mitigation effect while changing the configuration of the plates.

Chapter 4

Experimental Setup

4.1 Experimental Design

According to the objective of the work, the parametric study of the spoiler plates is studied on a model of spar platform in a fundamental way. In order to simulate the sea current, the model is towed with constant velocity in a towing tank. The towing tank used is "The University of Tokyo Experimental Tank" at Hongo Campus.

The model was towed with 25 different velocities to investigate the typical range of reduced velocity for spar platform: each velocity of the cart corresponds to a current condition. As the reduced velocity is also dependent on the natural period of the motion of the platform, the springs stiffness must be designed to stay in that range.

Different arrangements of spoiler plates have been tested to check the motion response of the platform, changing their configuration and geometric parameters. The experiment will be described in a more detailed way in the following sections

4.1.1 Towing Tank

As previously said, the model is towed in the tank and is attached to a cart through four springs mounted along the inline and transverse direction. The springs are supposed to ensure the restoration force given by a mooring system and support the motion of the model with the motion of the cart.

The time series of the motions were collected by a 3D tracking software, called Qualisys®. Four cameras are installed on the cart in order capture the 6 DOF motion of the floating body with a sampling frequency of 100 Hz. The number of cameras is directly proportional to the accuracy of the capture: in case the camera missed the targets, installed on the model's deck, the others can recollect the position and trace the time series of the motion, assuming the targets rigidly linked among themselves.

The towing tank facility has been provided by The University of Tokyo and all the experiments have been carried out in this facility, which consists on a water tank with a cart running above it, along two rails mounted on the sides of the tank. The dimension and the characteristics of the facility are summed up in the following Table.

Tank Dimension				**Cart Parameters**			
Dimension	**Symbol**	**Value**	**Unit**	**Parameter**	**Symbol**	**Value**	**Unit**
Length	L_t	85	m	Maximum Speed	$U_{c,max}$	0.7	m/s
Width	W_t	3.5	m	Minimum Speed	$U_{c,min}$	0.04	m/s
Depth	H_t	2.4	m	Weight	M_c	1203	kg

Table 4.1: Tank and cart specification

The following figure represents a sketch of the towing cart as designed and installed in 1968. On the left, the top view of the cart shows the central window deck, whilst on the right a side of the cart and a section show width and the water level.

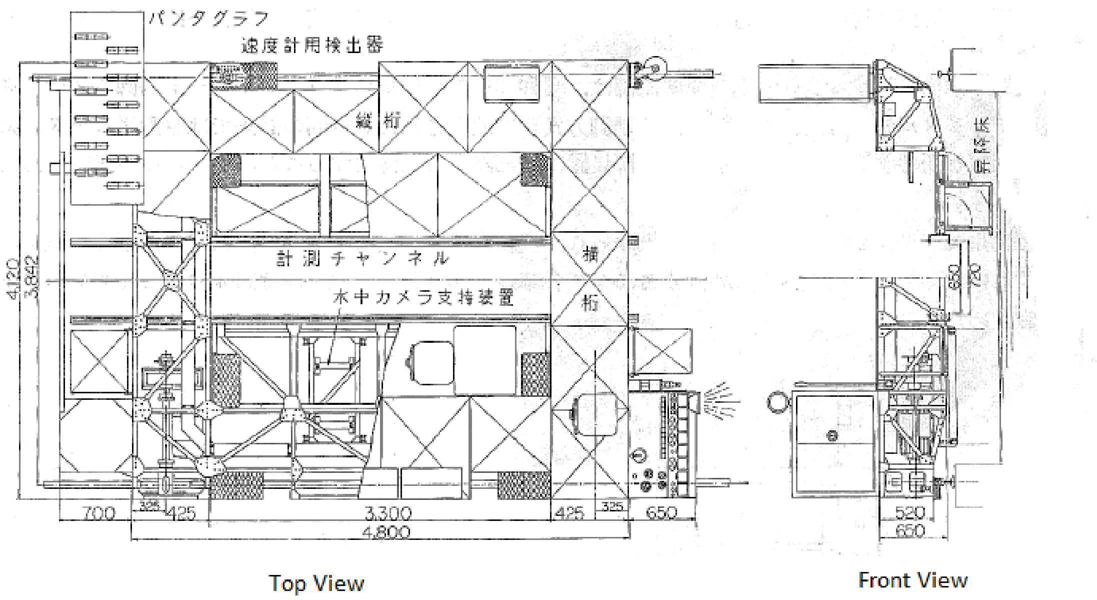

Figure 4.1: Top and front view of the Towing Cart of the University of Tokyo [26]

4.2 Model Design

4.2.1 Spar model

The model consists on a cylindrical steel model whose geometric characteristics are summed up in Table 4.2. The model size has been chosen according to the feasibility of the spoiler plates application. If the model sizes were comparable to the tank dimensions, the boundaries of the tank would significantly influence the structure motion.

Model Dimension			
Dimension	**Symbol**	**Value**	**Unit**
Length	L_C	600	mm
Immersed Length	L	450	mm
Diameter	D	300	mm
Aspect Ratio	L/D	1.5	–
Blockage Effect	B_e	0.016	–

Table 4.2: Spar model geometric characteristics

The parameter to take care of is the diameter of the model. The effect of the side of the tank can be relevant for the experiment results if the diameter of the model is too big. This effect has been described in literature as *blockage effect* and consists on an increase in relative flow speed around the cylinder, as water is constrained in a tank. The increase of relative speed involves change in pressure distribution on the model surface and consequently a change in motion. The blockage effect is usually verified for high *diameter to tank width ratio* or *immerse length to tank depth ratio*, but the choice of a towing tank compared to the recirculating channel made the effect negligible (see Table 4.2).

The model is empty inside and manufactured in steel according to the purpose of the experiment. The spoiler plates are made of Neodymium, ferromagnetic material, in order to easy the change of configuration of the plates.

Furthermore, a deck has been designed to put the target for Qualisys® tracking system.

4.2.2 Ballasts

As far as the stability of the model is concerned, the model is *ballast-stabilized* type. Indeed, in order to keep the same immersed length (draft) and to lower its centre of gravity, ballasts must be arranged inside the model.

The draft line is kept equalizing the mass of water displaced with the total mass of the body. The total mass of the body is less of the volume displaced, as the model is hollow. The difference between the real mass of the model and the mass of the displaced water is the mass of ballasts required to keep the draft. The total mass has been calculated comprehensive of the deck of the model. The calculation routine is shown below.

Firstly, the volume of water displaced, V_D is calculated, fixing the draft line. The draft line is equivalent to the immersed length of the model:

$$V_D = \pi \frac{D^2 L}{4} \tag{4.1}$$

Consequently the mass of water displaced is calculated, knowing the water density, ρ_w:

$$m_D = \rho_w V_D \tag{4.2}$$

Once the mass displaced is derived and the weight of the model is known, the mass of the ballasts is quickly calculated as the difference between the two.

Four fundamental coordinates must be taken into account while designing a platform: centre of gravity (G), centre of buoyancy (B), metacenter (M) and the water plane point (F). These values have been estimated modelling with Solidworks®. In the centre of gravity the weight force is acting, while in the centre of buoyancy the buoyancy force is acting. The two forces are equal in modulus as the platform is floating with fixed draft, but opposite direction.

Adding ballasts is not just a matter of keeping the draft but also of stability. In ship design theory, the stability is ensured when the metacenter is higher than the centre of gravity (measured from the keel). In addition, the higher the distance between centre of gravity and metacenter, the higher the stability. This distance is called *metacentric height*.

According to Figure 4.2, case (a) the position of the centre of gravity ensures a moment which avoids the overturning of the platform: the moment of the gravity

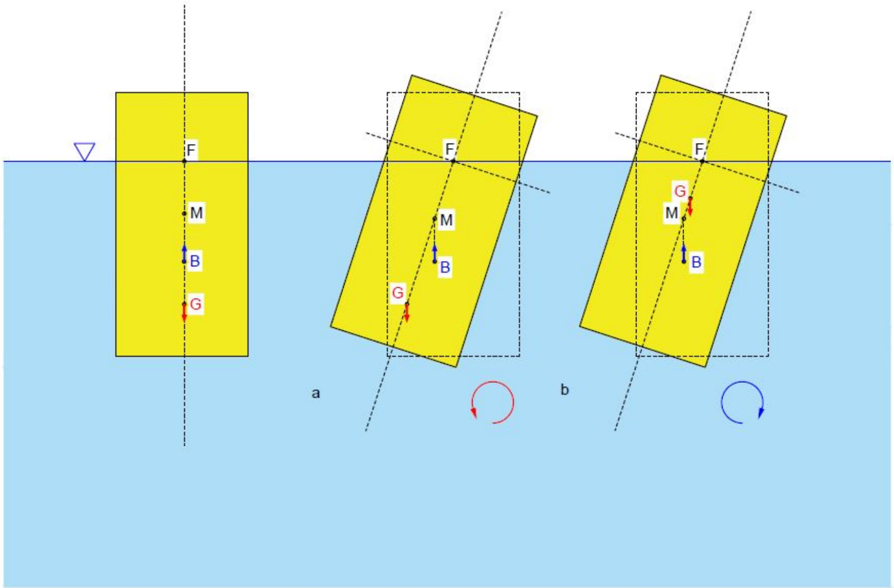

Figure 4.2: Sketch of the static of a cylindrical floating structure

force is higher and opposite to the one of the buoyancy force. Whilst, case (b) highlights an instability of the platform with consequent overturning moment.

Design values and characteristics of the model are summed up in Table 4.3, with related calculation in Appendix A and picture of the model in Figure 4.3b.

Model Dimension			
Dimension	**Symbol**	**Value**	**Unit**
Weight[1]	m	31.81	kg
Ballasts Weight	m_b	13.38	kg
Water Displacement	V_D	$3.18 \cdot 10^7$	mm^3
Centre of Gravity[12]	G	204	mm
Centre of Gravity[3]	G	297	mm
Centre of Buoyancy[2]	B	225	mm
Metacentre[2]	M	250	mm
Metacentric Height	GM	47	mm

Table 4.3: Spar model inertial characteristics

[1]Comprehensive of ballasts
[2]Measured from the keel: as the model is symmetric just one coordinate is required.
[3]Without ballasts, from inertia test

(a) **(b)** **(c)**

Figure 4.3: Ballasts arrangement (a), model manufactured (b) and position of the centres (c)

4.2.3 Spoiler Plates

The spoiler plates used for the experiment are Neodymium magnets with a shape designed specifically for the experiment. The non-dimensional parameters chosen to characterize the geometry of the spoiler plates are the following:

- Aspect ratio of the spoiler, $A_{R,S}$, defined as:

$$A_{R,S} = D_S/L_S \tag{4.3}$$

- Length ratio spoiler extrusion and diameter platform, defined as:

$$L_{R,S-P} = D_S/D \tag{4.4}$$

According to the lack of studies and data regarding spoiler plates dimension the dimensions listed in Table 4.4 has been chosen:

The thickness of the spoiler has been designed to ensure the attachment between the spoiler and the curved surface of the cylinder. Small thickness coupled with a big curve radius is the condition to minimize the imperfect coupling between spoiler and cylinder. The calculation for the spoiler plates design and the material characteristics are explained in Appendix A. According to the small mass value of the spoiler, their contribute on the change in the draft have been considered irrelevant.

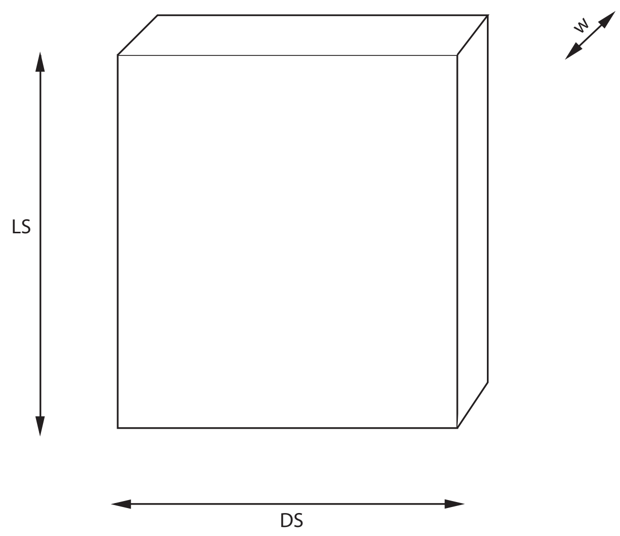

Figure 4.4: Sketch of a spoiler plate

Spoiler Plates Dimension				
Parameter	**Symbol**	**Type 1**	**Type 2**	**Type 3**
Aspect Ratio	$A_{R,S}$	0.5	1	2
Length Ratio	$L_{R,S-P}$	1/60	1/30	1/15
Thickness	$w_s[mm]$	3	3	3

Table 4.4: Spoiler Plates geometric characteristics

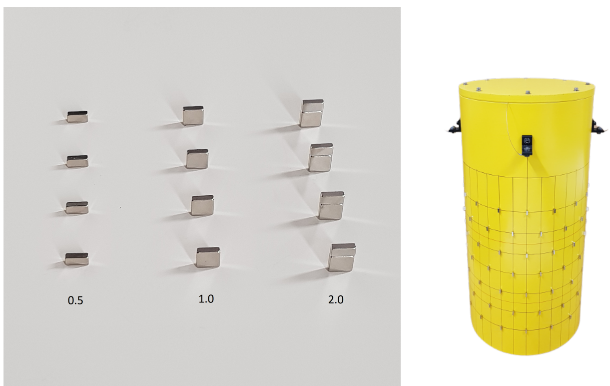

(a) **(b)**

Figure 4.5: Different spoiler plates aspect ratio (a) and model with spoiler plates (b)

4.3 Experimental Procedure

4.3.1 Calibration and Installation

First step of the setup is to collocate and calibrate the cameras. A reference point coincident to the zero of the motion has to be settled on Qualisys®: this is called *calibration*. The tracking system, detects the relative motion between the targets - arranged on the deck of the model - and the reference point called *zero condition*, through cameras mounted on the cart.

After the calibration step, the experiment installation has been fulfilled arranging the ballasts inside the hollow model and fixing the deck on the top of it. After verifying that the water line and the draft line are coincident, the model is fixed to the cart with a set of four springs, whose characteristics are listed in Table 4.5.

According to the work of Stappenbelt [24], the mooring system response for big displacement is usually considered as a non-linear phenomenon, but the choice of a pre-tensed configuration for the spring would reduce the non-linearity of the model response (see Figure 4.6).

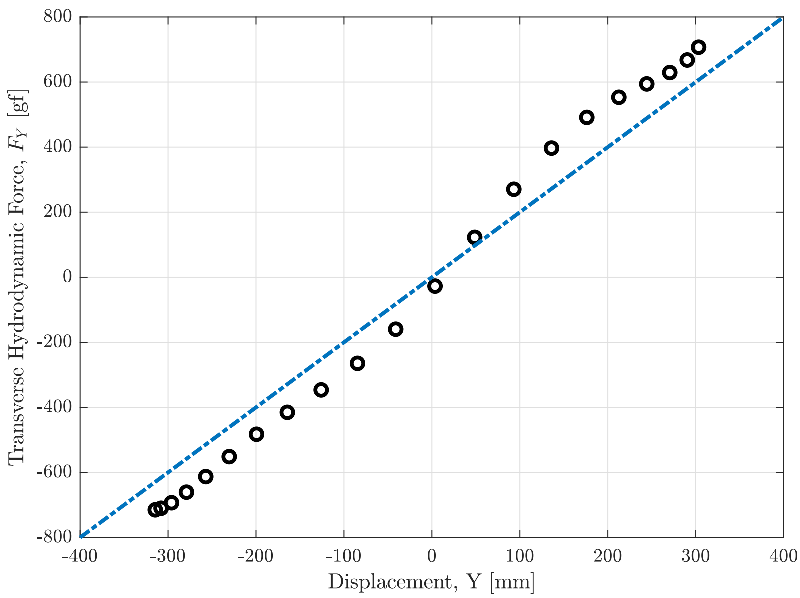

Figure 4.6: Demonstration of linear correlation between forces and displacements for the model designed

The model has been positioned inside the tank and its motion with the cart is supported by the set of springs. The configuration of the experimental set-up is sketched in Figure 4.7.

Spring Characteristics			
Parameter	**Symbol**	**Value**	**Unit**
Inline Spring Cable Length	KX	800	mm
Transverse Spring Cable Length	KY	400	mm
No-load Inline Spring Length	LKX	225	mm
No-load Transverse Spring Length	LKY	200	mm
Inline Spring Stiffness	k_x	0.76	gf/mm
Transverse Spring Stiffness	k_y	0.94	gf/mm

Table 4.5: Spring characteristics

4.3.2 Experimental Outline

The goal of the experiment is to collect the time series of the motion for the model for each current condition and per configuration of spoiler plates. From these data the parameters identifying the FIM (specified in Chapter 2) are calculated. The current condition are performed in the towing tank shown in Figure 4.8

Several experiments have been carried out in the past decades and from that experience the range of reduced velocities has been calculated. This range has been chosen according to the work of Gonçalves et al. [11], in which experiments with low aspect ratio cylinders have been carried out. In the A_R=1.5 case, it is verified a synchronization region in both inline and transverse direction between $4 < U_r < 9$ reduced velocities.

As this range is crucial for the analysis, more towing speeds have been tested in that range. In order to set the range of reduced velocities a preliminary decay test for the smooth cylinder took place. The decay gave as a result the natural period of the motion for the model of study, and consequently the calculation of the range of reduced velocity.

Once established the range of investigation, the parametric study had been performed. The parametric study goal is to understand the physics behind changing the spoiler arrangement.

The spoiler arrangement consists on a set of circumferences equidistant, use to position the spoiler plates in the vertical direction of the model, and a set of radial position angular equidistant between each other of an angle α.

The plate are not aligned in the vertical direction, but changing the circumference the plates position is twisted of an angle:

$$\beta_i = \frac{\alpha_i}{2}, \tag{4.5}$$

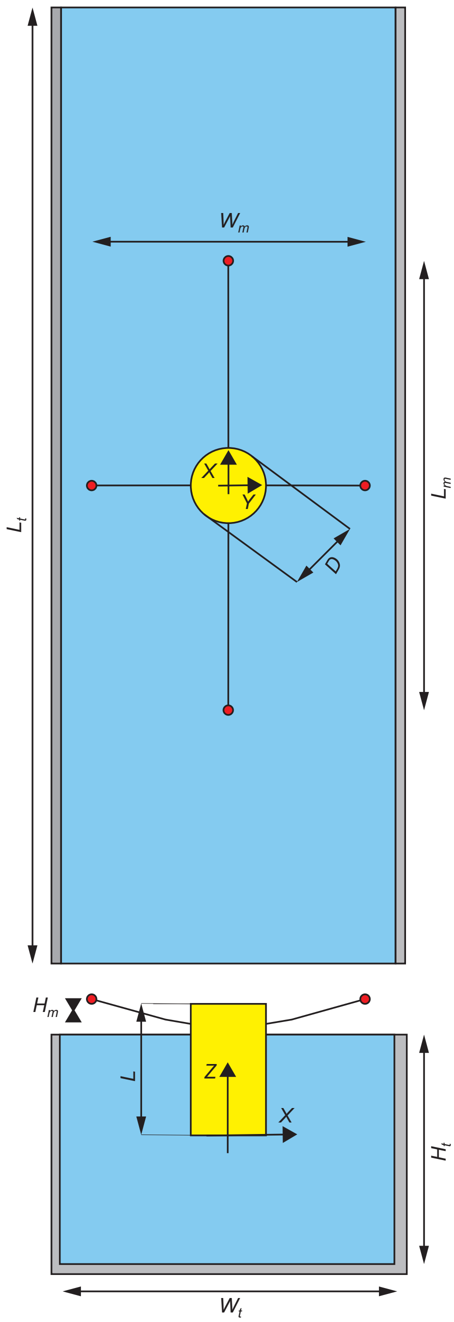

Figure 4.7: Sketch of the experimental setup (not in scale)

where the index i identifies a specific set of n_D. This is due to the fact that increasing the density of spoiler plates on a circumference the angular distance between two spoiler will decrease.

The configuration parameters chosen are listed below:

- circumferential number of plates, n_D;
- number of circumferences of plates, n_L;

Figure 4.8: Experimental Towing Tank at the University of Tokyo, Hongo Campus

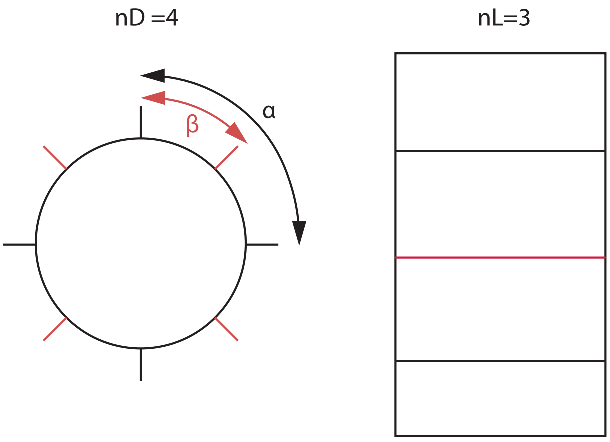

Figure 4.9: Top view (left) and side view of twisted disposition of the spoiler plates on the model

- aspect ratio of the plates, $A_{R,S}$.

The parameters' values have been selected in order to have significant influence on the results: because of the lack of research in this specific topic, the difference in results could not be obvious. All of them are summed up in Table 4.6.

Investigating the influence of the parameters on the phenomenon will help in evaluating future choices and optimization of this kind of devices.

Spoiler Plates Arrangement Parameters				
Parameter	**Symbol**	**Values**		
Number of Circumferences of Plates	n_L	3	5	7
Number of Plates per Circumference	n_D	4	8	16
Aspect Ratio of the Plates	$A_{R,S}$	0.5	1	2

Table 4.6: Spoiler Plate Arrangement Parameters

4.3.3 Decay test

As previously remarked, a decay test is performed while changing the spoiler plate arrangement on the model surface. The test is performed in the towing tank in still water condition. The aim of the test is to derived the decay in the motion amplitude for the platform according to the viscous and the structural damping on the system. The value of the natural period of the decay is calculated to derive the reduced velocity range of the platform model.

Figure 4.12 shows a typical decay curve for the model of interest. The decay test must be carried out for each mode of motion taken into account for the analysis (in this case 2 DOF).

The natural period for inline and transverse direction are shown in Table **??**, and it can be deduced that changes can be neglected.

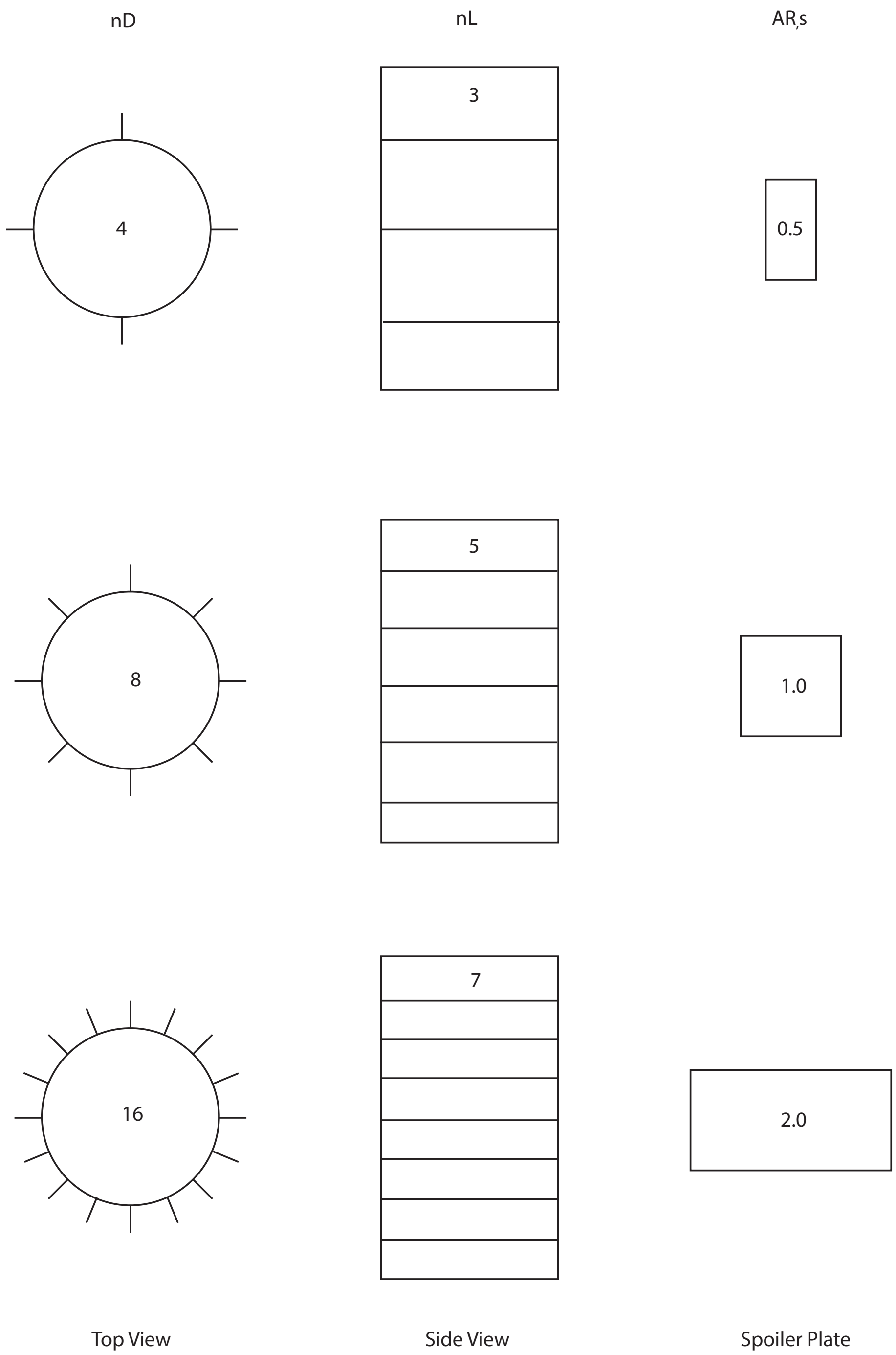

Figure 4.10: Sketch of the parameters involved

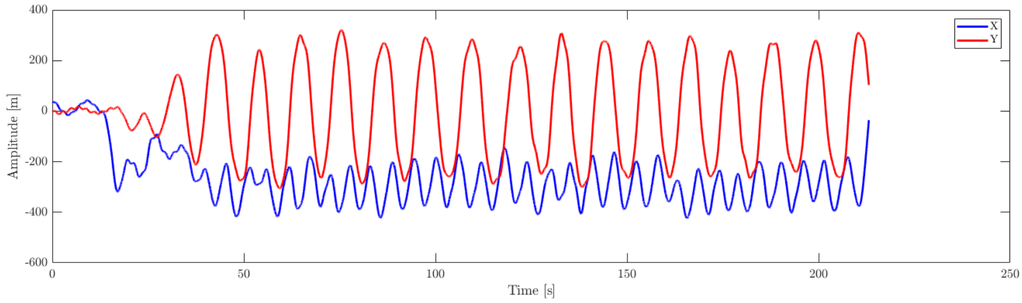

Figure 4.11: Time series of the model displacements (inline in blue and transverse in red) in synchronization region (U_r=5.3)

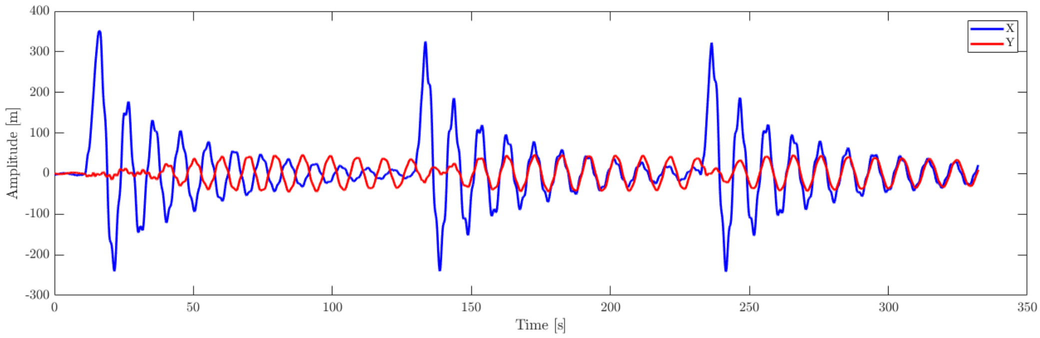

Figure 4.12: Inline decay curve for spar platform model without spoiler plates arranged. The decay is perform three times for benchmark reason

Natural Period Change				
Case	$T_{n,x}$ [s]	$T_{n,y}$ [s]	Δ_x [%]	Δ_y [%]
No Spoiler	9,168	9,3597	-	-
$A_{R,S} = 0.5, n_L = 5, n_D = 8$	9,2298	9,3736	0,7	0,1
$A_{R,S} = 1.0, n_L = 5, n_D = 16$	9,2444	9,3724	0,8	0,1
$A_{R,S} = 1.0, n_L = 5, n_D = 4$	9,1494	9,3721	-0,2	0,1
$A_{R,S} = 2.0, n_L = 5, n_D = 8$	9,2223	9,3499	0,6	-0,1
$A_{R,S} = 2.0, n_L = 5, n_D = 4$	9,2785	9,445	1,2	0,9
$A_{R,S} = 1.0, n_L = 3, n_D = 8$	9,2891	9,2924	1,3	-0,7
$A_{R,S} = 1.0, n_L = 7, n_D = 8$	9,1911	9,3725	0,3	0,1
$A_{R,S} = 2.0, n_L = 5, n_D = 16$	9,2377	9,3543	0,8	-0,1
$A_{R,S} = 2.0, n_L = 3, n_D = 8$	9,2794	9,375	1,2	0,2
$A_{R,S} = 2.0, n_L = 7, n_D = 8$	9,271	9,44	1,1	0,9
$A_{R,S} = 2.0, n_L = 3, n_D = 4$	9,297	9,3463	1,4	-0,1
$A_{R,S} = 2.0, n_L = 7, n_D = 4$	9,2846	9,3803	1,3	0,2

Table 4.7: Natural period derived from the free decay test. The Δ value is the difference between each case and the *no spoiler* case

Chapter 5

Experimental Results

5.1 Experiment Development

According to the methodology followed in Chapter 3, the experiment has been divided into four *stages*, and in each stage are performed a number of *cases*: each study correspond to a parameter study. The *case 2* of each parameter is considered the fixed parameter value in each study performed. All the experiment record has been described in Table 5.1 and Figure 5.12.

Experiment Record				
Stage	**Parameter Study**	$A_{R,S}$	n_L	n_D
0	Without Spoiler	-	-	-
A	$A_{R,S}$	0.5 - 1.0 - 2.0	5	8
A	n_L	1.0	3 - 5 - 7	8
A	n_D	1.0	5	4 - 8 - 16
B	n_L	2.0	3 - 5 - 7	8
B	n_D	2.0	5	4 - 8 - 16
C	n_L	2.0	3 - 5 - 7	4

Table 5.1: Experiment record

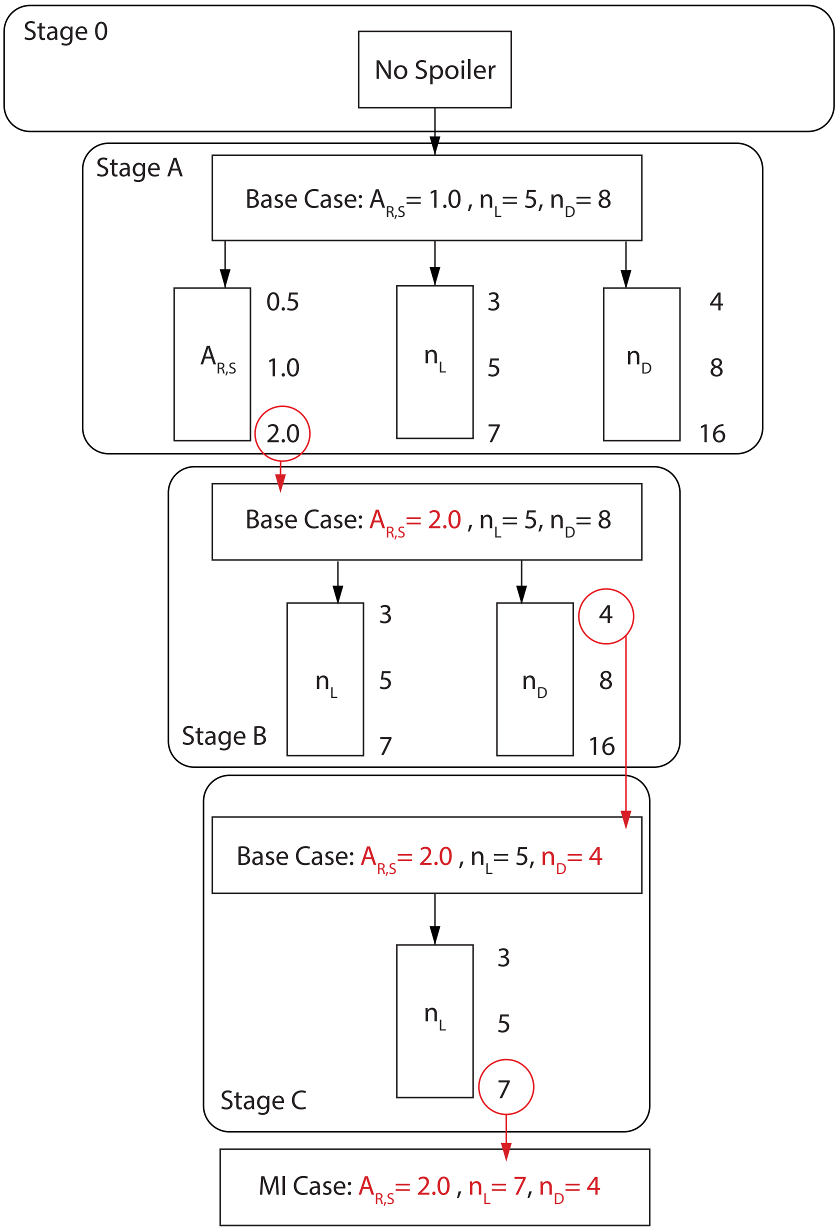

Figure 5.1: Experiment organigram

5.2 Stage 0 - No Spoiler

Stage 0 was performed to be able to verify the FIM mitigation. *Stage A* is the first set of experiment in order to investigate the phenomenon suppression. *Stage B* is the second set of experiment to verify the previous studies' results. *Stage C* is the final set carried out to select the best mitigating values associated to each parameter, using the cases object of analysis. The last phase direction was given by a PMA on the data previously collected.

In the following figures will be shown the results related to the *No Spoiler* case for motion, forces and PSD analysis.

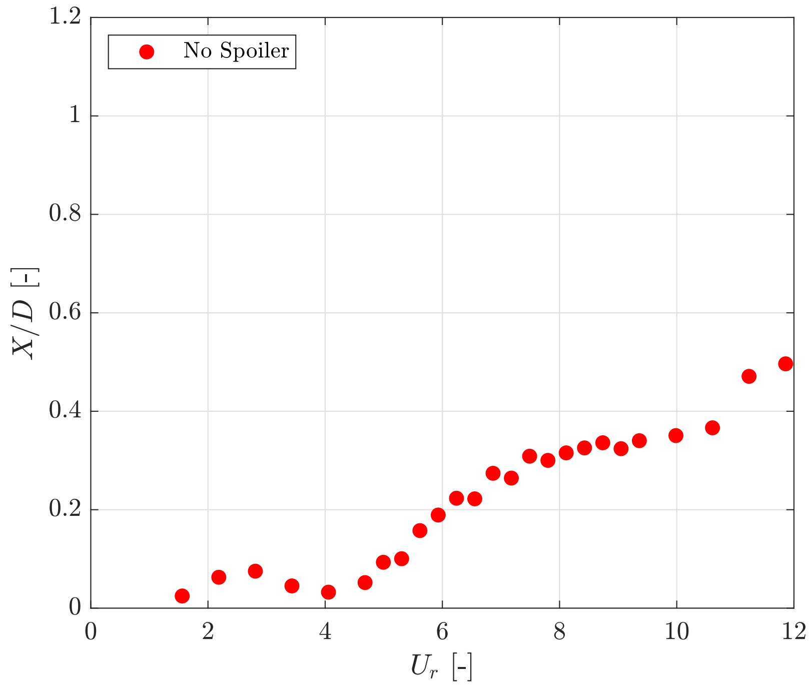

Figure 5.2: Non-dimensional inline amplitude for *Stage 0*, X/D

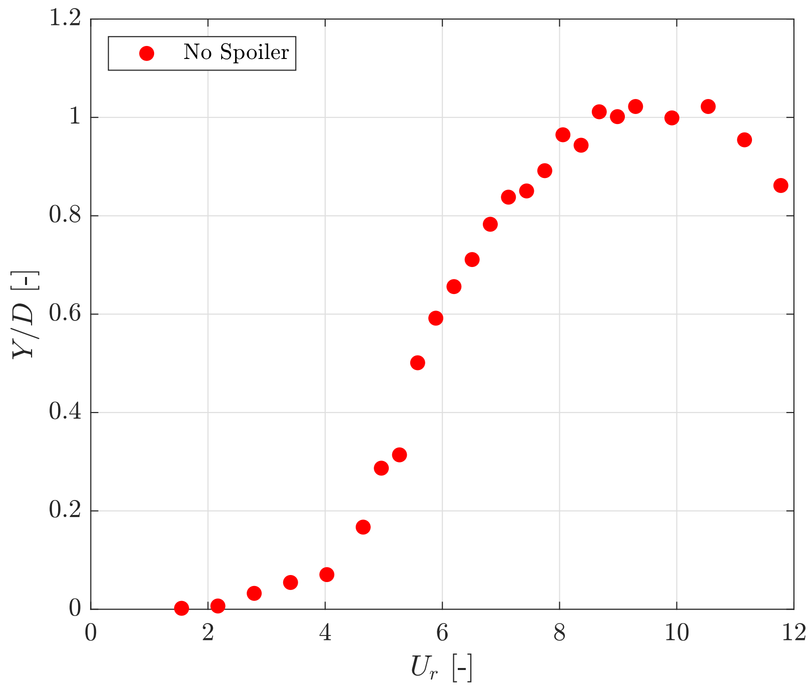

Figure 5.3: Non-dimensional transverse amplitude for *Stage 0*, Y/D

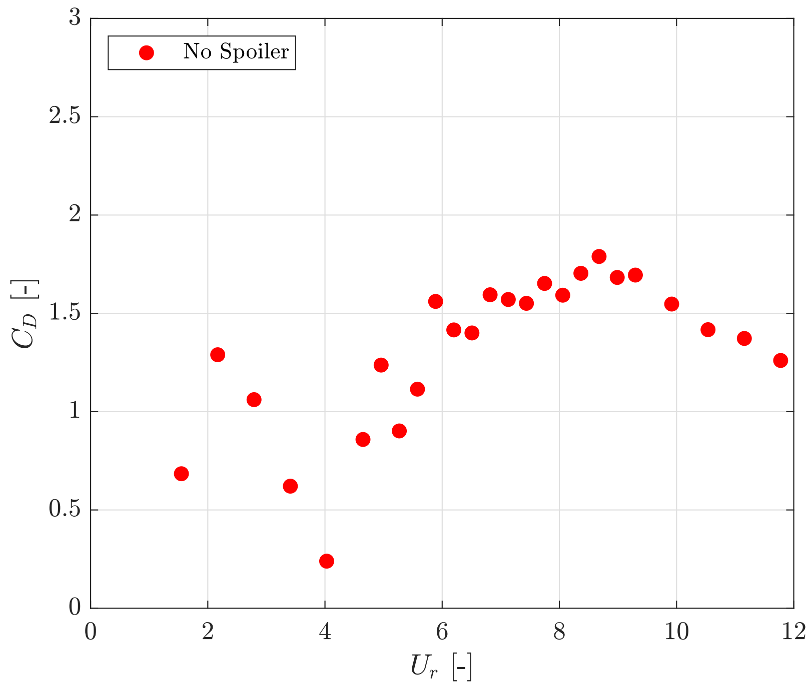

Figure 5.4: Drag coefficient for *Stage 0*, C_D

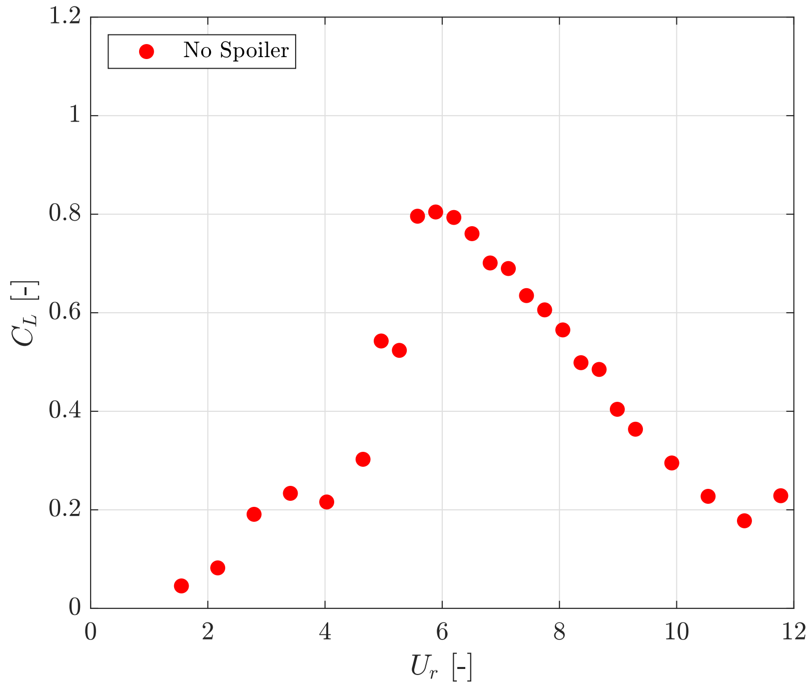

Figure 5.5: Lift coefficient for *Stage 0*, C_L

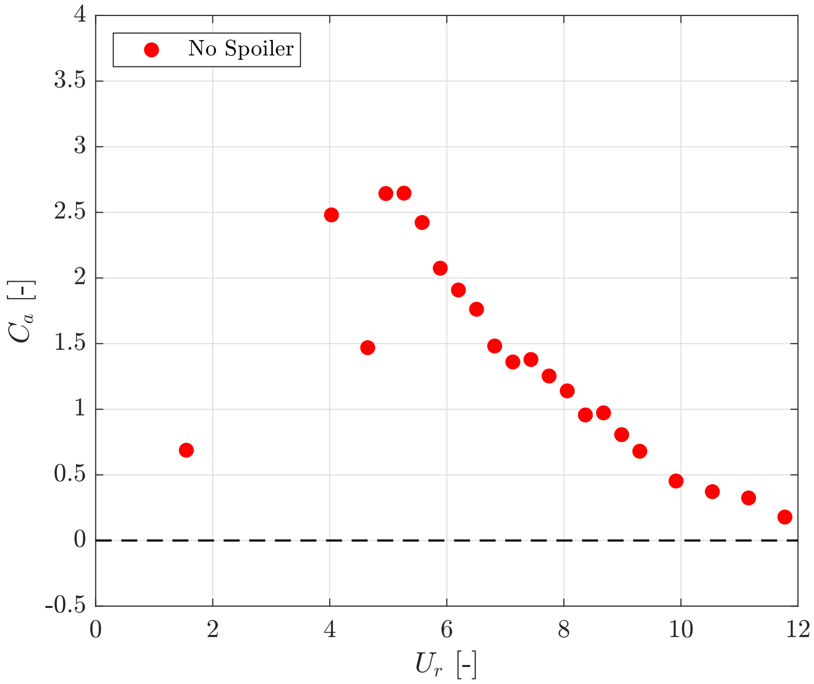

Figure 5.6: Added mass coefficient for *Stage 0*, C_a

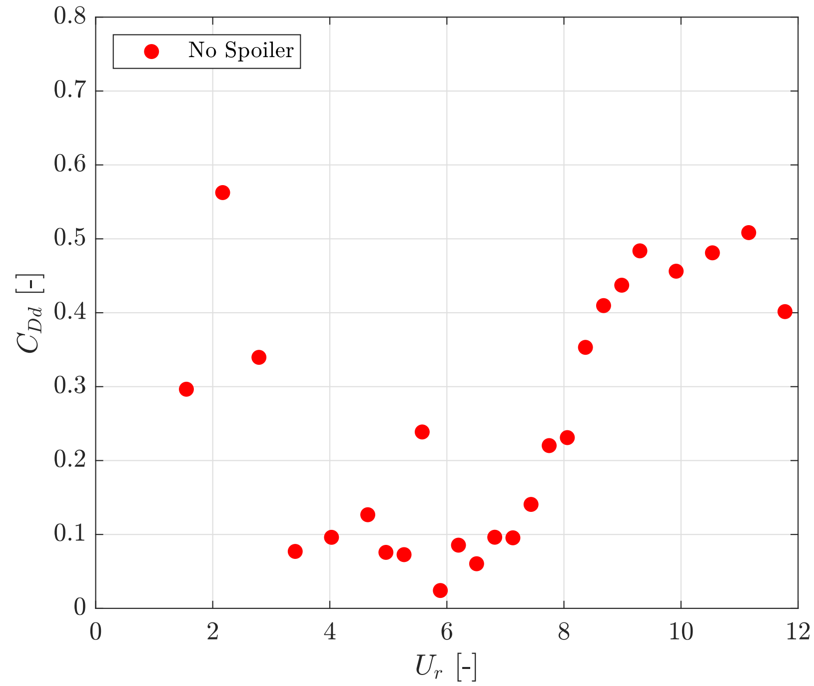

Figure 5.7: Dynamic drag coefficient for *Stage 0*, C_{Dd}

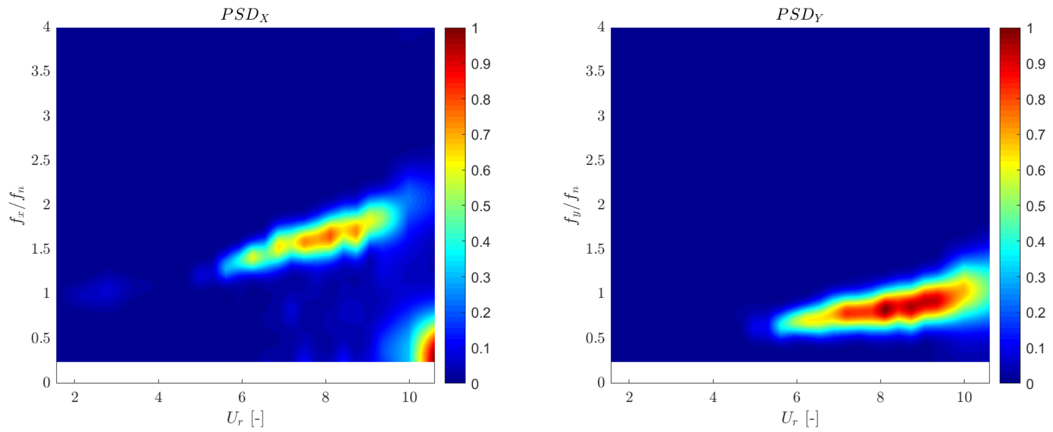

Figure 5.8: Power Spectrum Density of the motion in the inline (a) and transverse (b) direction

According to what previously said in Chapter 3, the definition of a synchronization range is fundamental to understand whether FIM is activated or deactivated. According to Figure 5.8, it is possible to identify a synchronization range for inline and transverse motion, as stated in Table 5.2.

Synchronization Range	
Inline	Transverse
$5 < U_r < 10$	$5 < U_r < 12$

Table 5.2: Synchronization range for the *No spoiler* case

Even though the amplitudes of the motion are still large, the PSD values can be small as the phenomenon is no more oscillatory, so the energy of the vortices is not relevant for FIM.

5.3 Stage A - Parameter $A_{R,S}$

The first stage of the analysis consists on analyzing the influence of the $A_{R,S}$ on FIM phenomenon. The parameter fixed were n_L=5 and n_D=8. Four cases were analyzed: one was the *no spoiler* case and the remaining were the cases targeted for this stage.

As shown in Figure 5.9, mitigation in the inline direction increased while the $A_{R,S}$ is increased. The same behaviour was verified for the transverse direction (see Figure 5.10). $A_{R,S} = 2.0$ case emphasizes a better response in the synchronization range, between $5 \leq U_r \leq 8$ for this platform. Although, the mitigation is verified, the difference in amplitude between $A_{R,S}$ = 2.0 and $A_{R,S}$= 1.0 . Next stages will evidence the best case with higher accuracy.

Furthermore, it can be noticed a different behavior between inline and transverse response for different ranges of reduced velocity. Higher mitigation occurs in synchronization range and for higher reduced velocities (U_r >8) analyzing the inline response. In addition the first resonant peak for $2 < U_r < 4$ is evidently mitigated by changing the $A_{R,S}$.

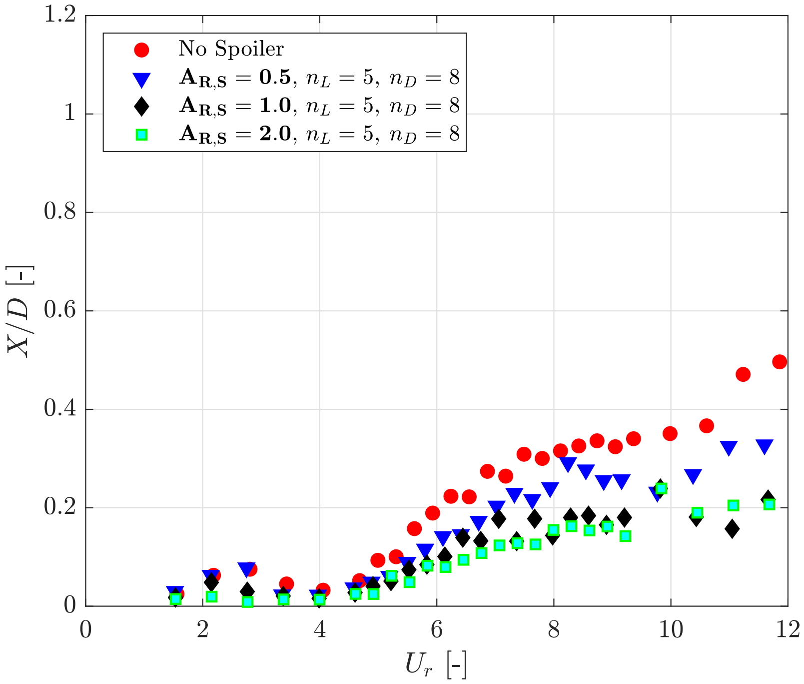

Figure 5.9: Effect of $A_{R,S}$ on the non-dimensional inline amplitude, X/D

Whilst, for the transverse response, the mitigation starts being effective for reduced velocities U_r >5, reaching around 30% reduction for $U_r > 8$. Focusing on the transverse, the response trend for $A_{R,S} = 2.0$ suggests a desynchronization range behaviour at around $U_r = 9$, which will be also confirmed in the PSD analysis.

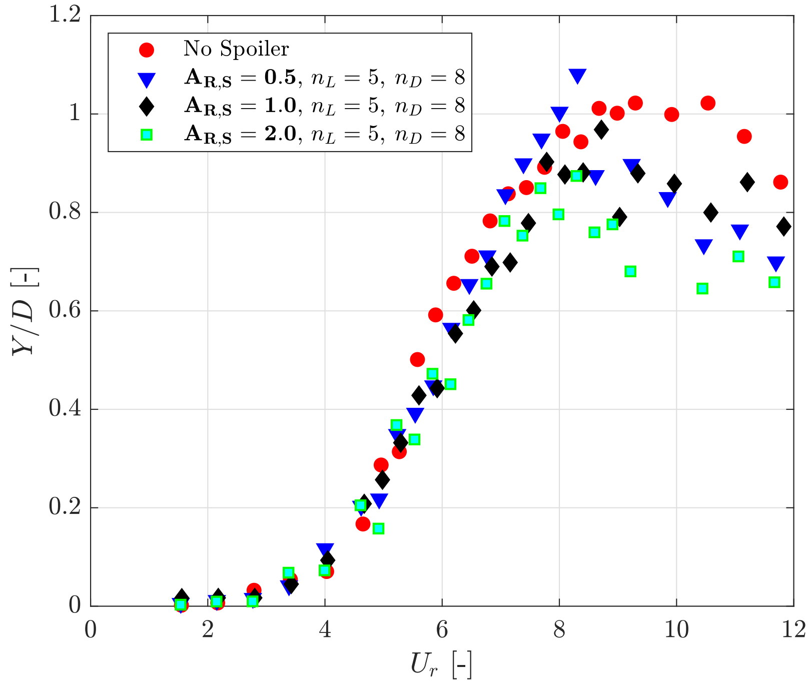

Figure 5.10: Effect of $A_{R,S}$ on the non-dimensional transverse amplitude, Y/D

The physics acting behind the spoiler plate can be described through further analysis, such as *forces analysis*.

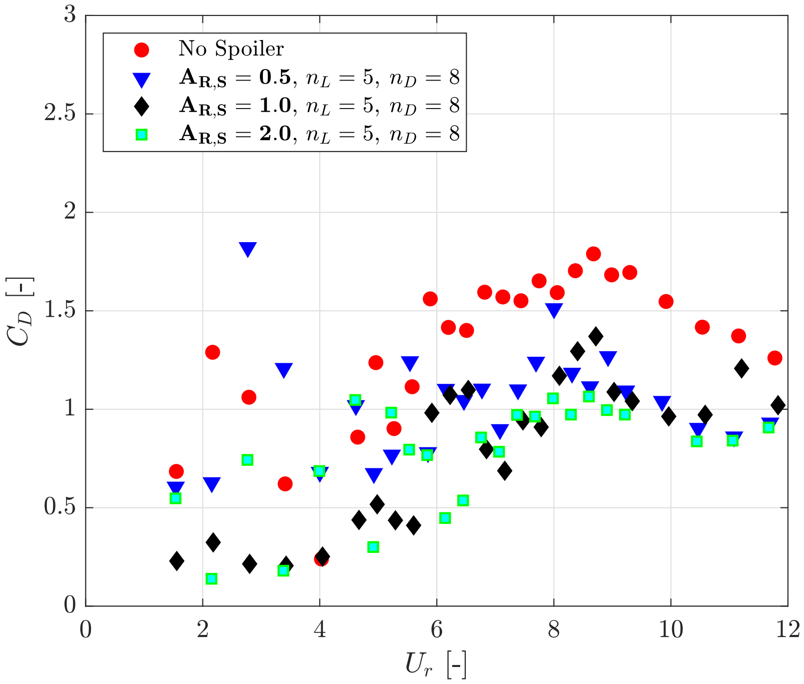

Figure 5.11: Effect of $A_{R,S}$ on the drag coefficient, C_a

The results regarding the drag coefficient are shown in Figure 5.11 and confirms the mitigating behavior of the spoiler plates in inline direction. This results can be physically explained according to Blevins [3], because of the drag coefficient dependence on the turbulent regime. Even though the regime (see Table 5.3) is in the transition range ($150 < Re < 3 \cdot 10^5$) and the boundary layer is expected to be laminar, the plot suggests an anticipation to the critical regime ($Re > 3 \cdot 10^5$) of the analyzed case.The increasing trend for reduced velocities up to $U_r = 8$ is pointed in literature as *drag amplification*

Experiment Reynolds Range		
U_r [-]	U $[m/s]$	Re [-]
1.56 - 11.58	0.05 - 0.38	$1.25 \cdot 10^4$ - $9.50 \cdot 10^4$

Table 5.3: Reynolds Range for the experiment

The turbulence of the boundary layer is correlated to the roughness of the body surface, in this case increased by the presence of spoiler plates. Several works in literature linked the reduction of the drag coefficient to the presence of element on the surface "interrupting" the boundary layer. The consequence of a turbulent boundary layer is a decreasing trend for the C_D for increasing Re numbers, with an

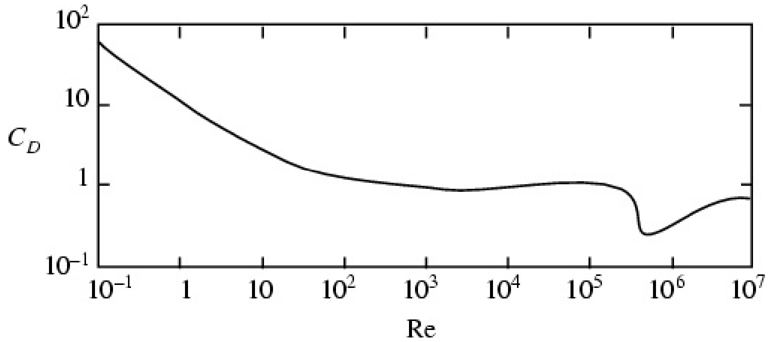

Figure 5.12: Influence of the flow regime (*Re* number) on the drag coefficient for cross-flow in cylindrical bodies

abrupt drop coincident to the *drag crisis*.

As stated in Huang et al. [12], the increasing value of mean drag ,C_D, is caused by a phenomenon investigated in literature as *drag amplification*. This behavior is involved inside the *synchronization* range, when FIM is resonant and acting on the platform.

The increasing $A_{R,S}$ the more efficient is the mitigation in the inline direction, according to a decreasing trend of the C_D. This can be linked to the turbulent boundary layer, whose turbulence is increasing while increasing roughness of the surface: in this case changed while increasing the dimension of the spoiler.

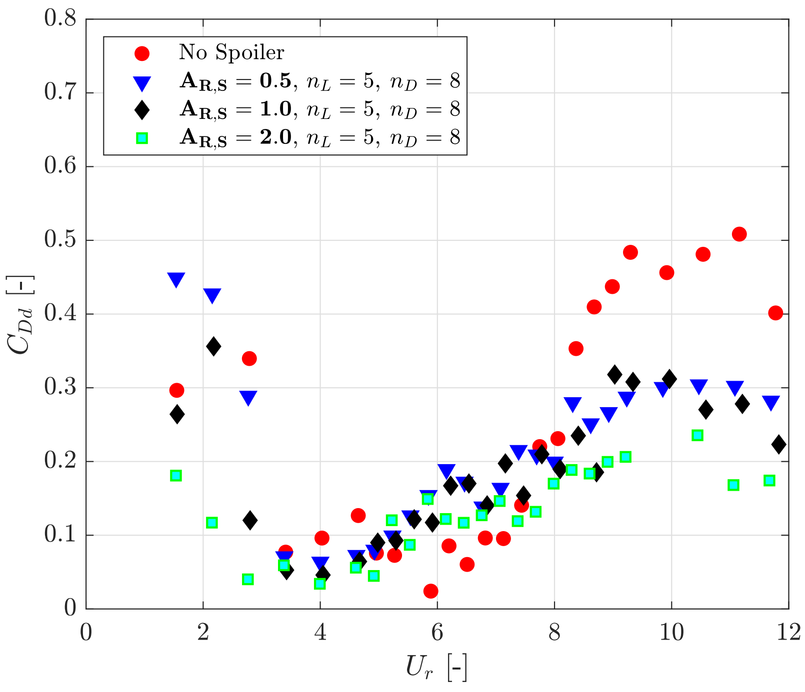

Figure 5.13: Effect of $A_{R,S}$ on the dynamic drag coefficient, C_{Dd}

Regarding the C_{Dd} evaluation in Figure 5.13, the oscillatory component of the drag is increasing in the synchronization range ($5 \leq U_r \leq 8$) because of the resonant behavior of the structure. Beyond the synchronization range ($U_r > 8$) the deviation is steady which suggests not a full suppression of the FIM in inline direction. In addiction, smaller deviation in the drag coefficient are noticed for $1.5 < U_r < 3$.

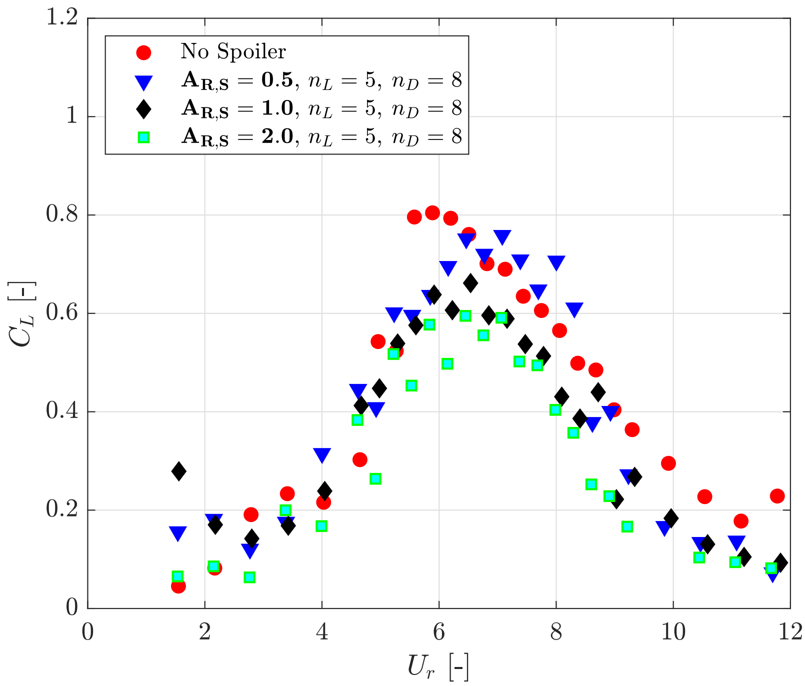

Figure 5.14: Effect of $A_{R,S}$ on the lift coefficient, C_L

According to Figure 5.14 and 5.15, the slight reduction in the synchronization range for the transverse amplitude can be attributed to both the C_L and the C_a. Differences in the amplitudes can be noticed for reduced velocities higher than $U_r > 8$. This behavior, as previously said, can be related to a desynchronization of the vortices. This fact, confirmed in Figure 5.15 and stated in Vikestad et al. [29], is verified for C_a, close to zero, or even negative.

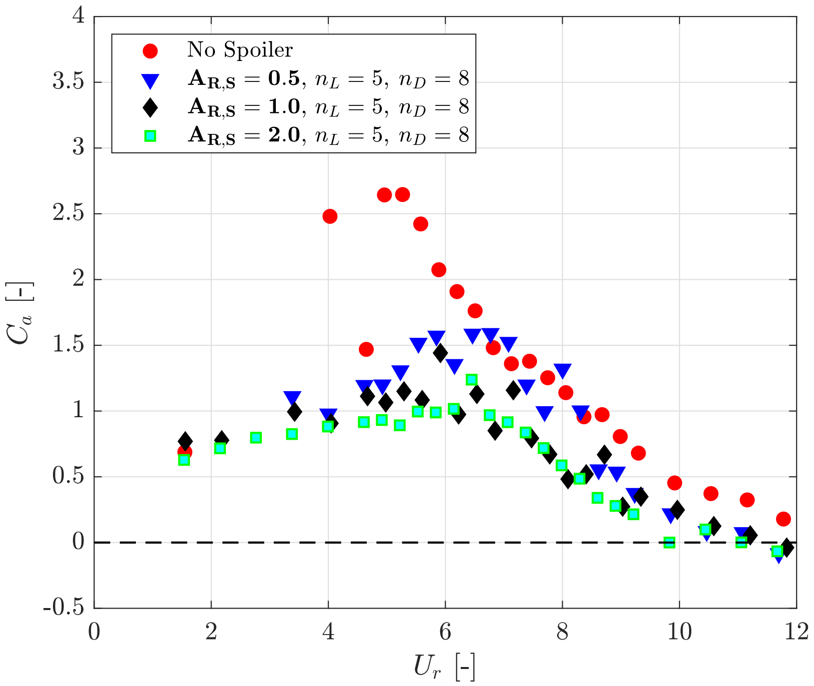

Figure 5.15: Effect of $A_{R,S}$ on the added mass coefficient, C_a

The peaks values for C_L and C_a are related to the resonant effect due to FIM. The range of reduced velocities for this peak is usually after the *synchronization range* of the FIM, in this case for $U_r > 5$.

The PSD analysis in Figure 5.16, 5.17 and 5.18, represent the effect of the spoiler configuration on the reduction of the synchronization range. Increasing the $A_{R,S}$ would almost mitigate the energy of the vortices for the inline direction. Reduction in the energy is also evident for the transverse case, and also the synchronization range is shorten to $6 < U_r < 10$ for the case $A_{R,S}$=2.0.

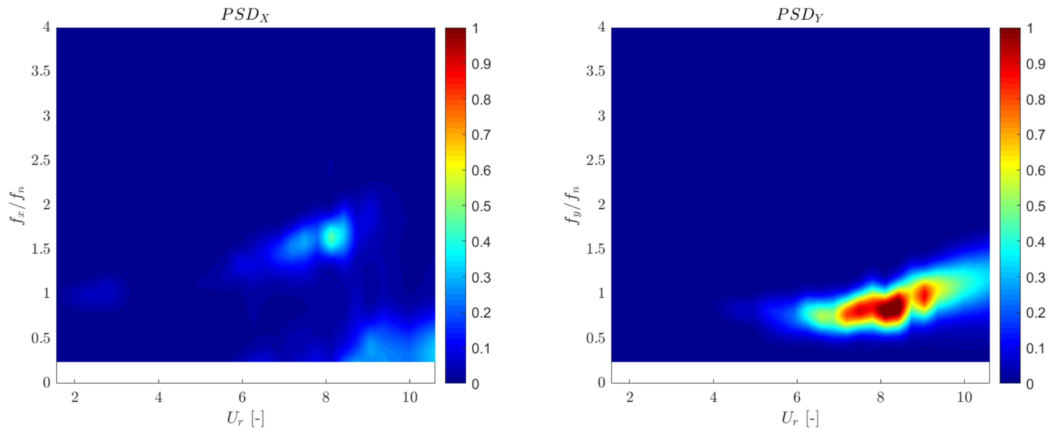

Figure 5.16: Normalized Power Spectrum Density of the motion in the inline (a) and transverse (b) direction for $A_{R,S} = 0.5$, $n_L = 5$ and $n_D = 8$

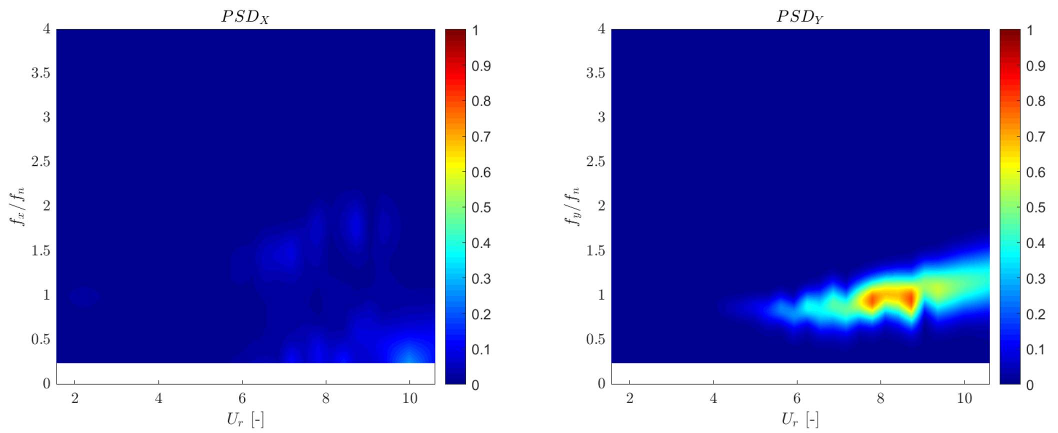

Figure 5.17: Normalized Power Spectrum Density of the motion in the inline (a) and transverse (b) direction for $A_{R,S} = 1.0$, $n_L = 5$ and $n_D = 8$

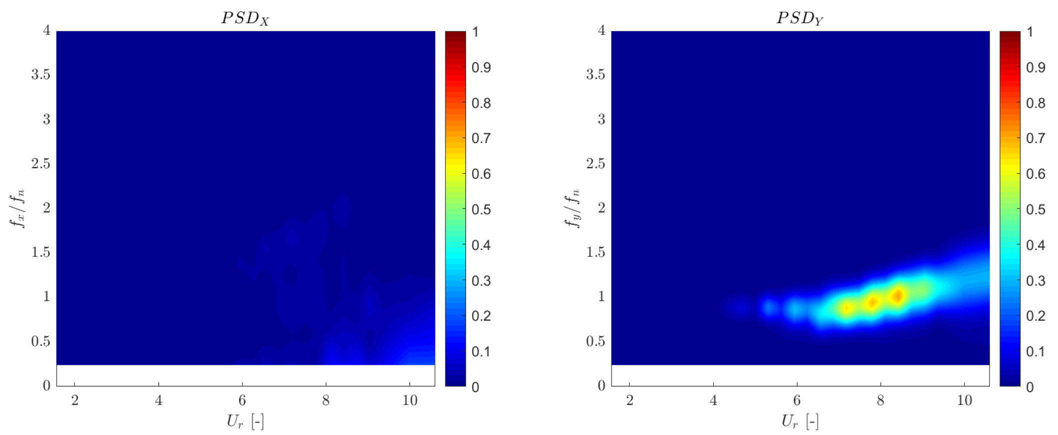

Figure 5.18: Normalized Power Spectrum Density of the motion in the inline (a) and transverse (b) direction for $A_{R,S} = 2.0$, $n_L = 5$ and $n_D = 8$

5.3.1 Stage A - Parameter n_L

The following stage aims at studying the effect of the number of rings of spoiler along the immersed length of the cylinder. The parameter fixed are $A_{R,S}$=1.0 and n_D=8. The cases compared are: the no spoiler case together with the other three cases targeted for this stage. The results obtained increasing the rings of plates are similar to the one obtained in the previous study.

In the case of the inline response shown in Figure 5.19 the case with n_L=7 appears to be the best up to reduced velocities $U_r < 10$. Beyond this value the best mitigated response is verified for n_L=5. In the low reduced velocity resonant peak range, the mitigation effect changing this parameter is not very affecting the suppression of the motion.

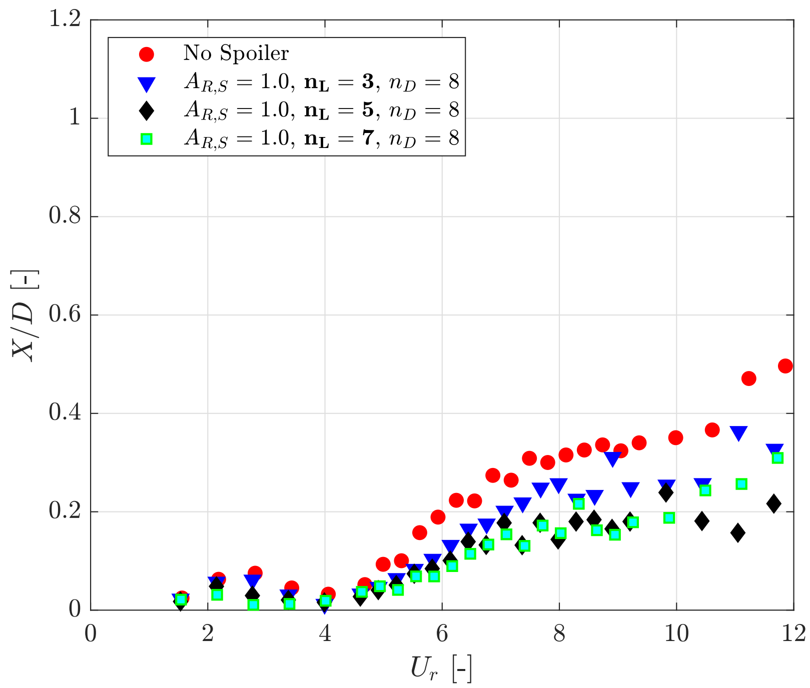

Figure 5.19: Effect of n_L on the inline non-dimensional amplitude, X/L

The difference between the inline and the transverse response is evident, comparing the two responses. As reported in Figure 5.20. The best case is n_L=7 for the whole range of reduced velocity analyzed. In the region in which the n_L appears like the best for the inline direction, in the transverse is the worst among this set of cases.

The analogy between the $A_{R,S}$ and the n_L is the increased roughness of the model along the surface. The number of rings is definitely related to the uniform roughness of the model surface. The more the rings the more rough is the surface and the boundary layer would be turbulent all along the immersed length. According to Figure 5.21 this implies a drag reduction for $U_r > 8$

According to the similarity to the previous case regarding the force analysis, the following plot will be attached in Appendix B.

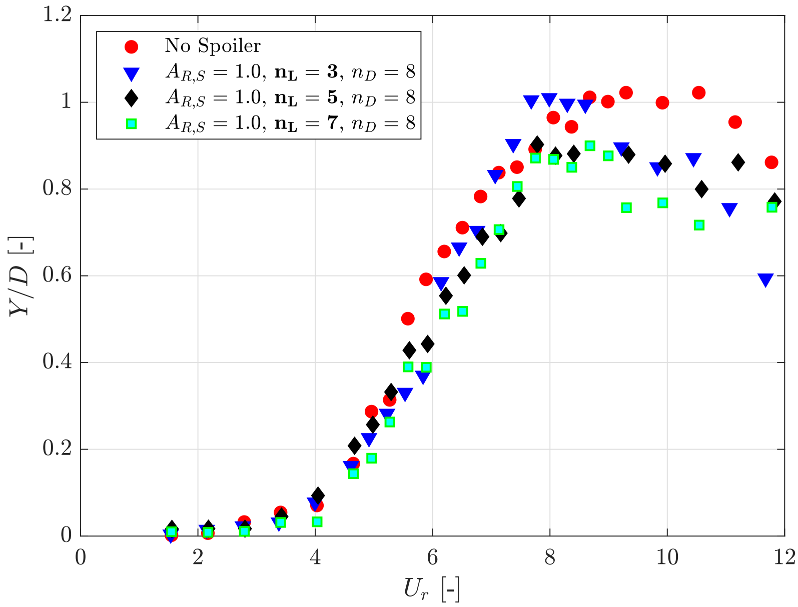

Figure 5.20: Effect of n_L on the transverse non-dimensional amplitude, Y/L

From the PSD analysis in Figure 5.22, 5.23 and 5.24, increasing the n_L would decrease the energy of the vortices with respect to the *No Spoiler* case for the inline direction. Reduction in the energy is also evident for the transverse case, even though the energy in the synchronization range is is not reduced as in the previous stage.

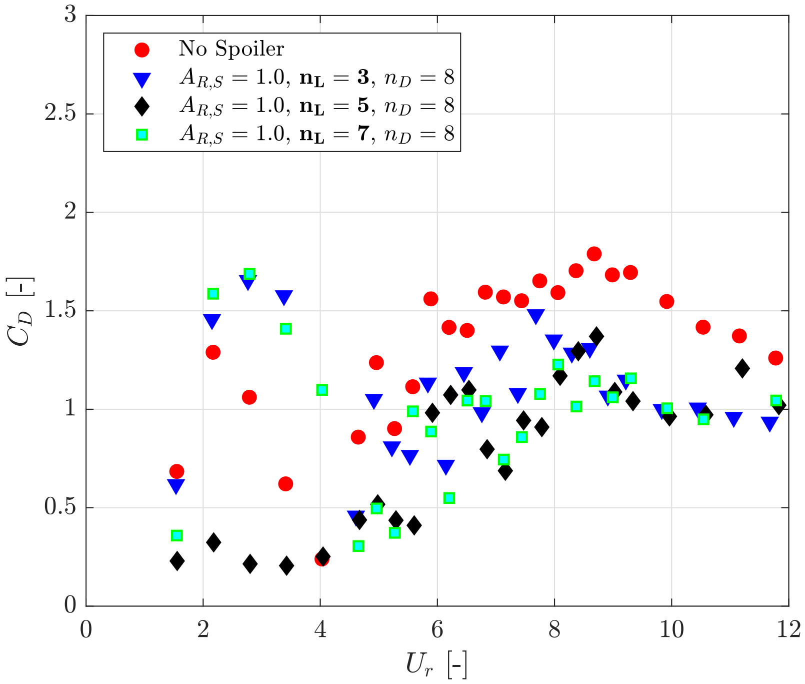

Figure 5.21: Effect of n_L on the drag coefficient, C_D

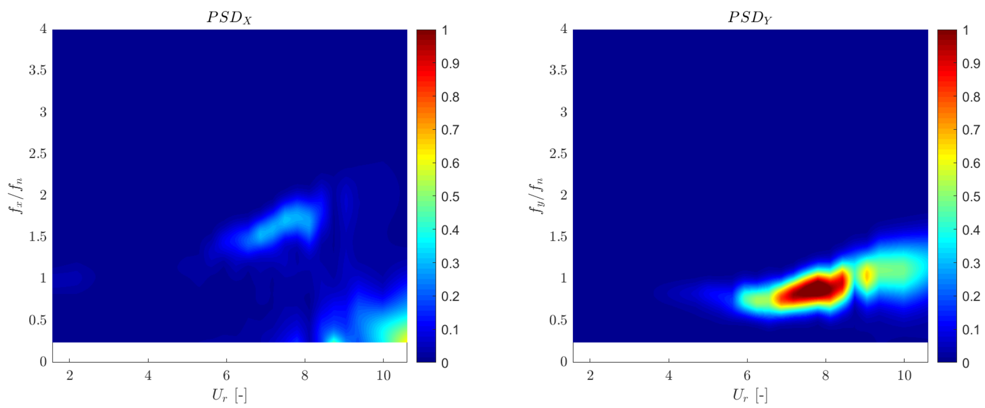

Figure 5.22: Normalized Power Spectrum Density of the motion in the inline (a) and transverse (b) direction for $A_{R,S} = 1.0$, $n_L = 3$ and $n_D = 8$

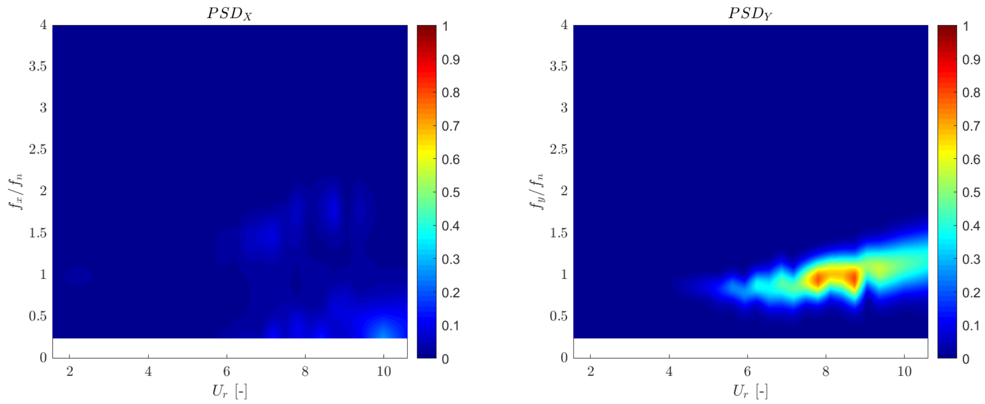

Figure 5.23: Normalized Power Spectrum Density of the motion in the inline (a) and transverse (b) direction for $A_{R,S} = 1.0$, $n_L = 5$ and $n_D = 8$

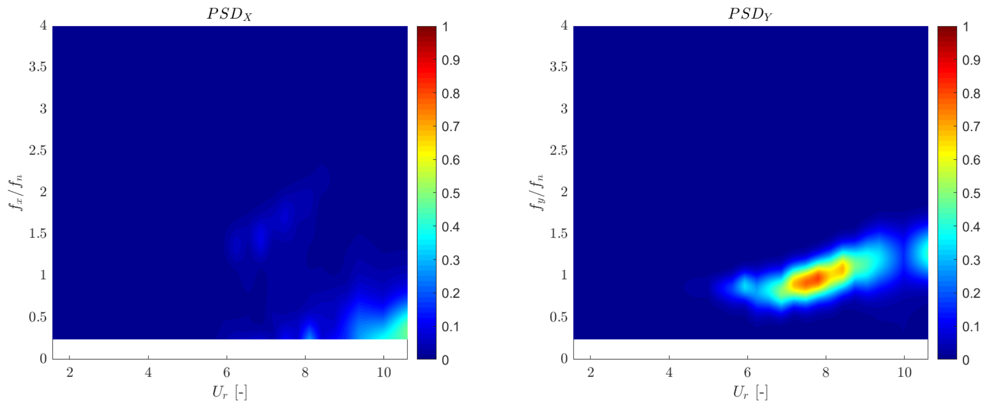

Figure 5.24: Normalized Power Spectrum Density of the motion in the inline (a) and transverse (b) direction for $A_{R,S} = 1.0$, $n_L = 7$ and $n_D = 8$

5.3.2 Stage A - Parameter n_D

The following stage aims at studying the effect of the number of plates per ring around the diameter of the cylinder. The parameter fixed are $A_{R,S}$=1.0 and n_L=5. The cases compared are: the no spoiler case together with the other three cases targeted for this stage.

In the case of the inline response shown in Figure 5.19, the case with n_D=4 appears to be the best because of a sudden drop in the range of $9 < U_r < 11$. This is confirmed in Figure 5.12, as a drag crisis is verified in the range above cited. According to Figure 5.27, the same range of reduced velocities results to be the best for the n_D case.

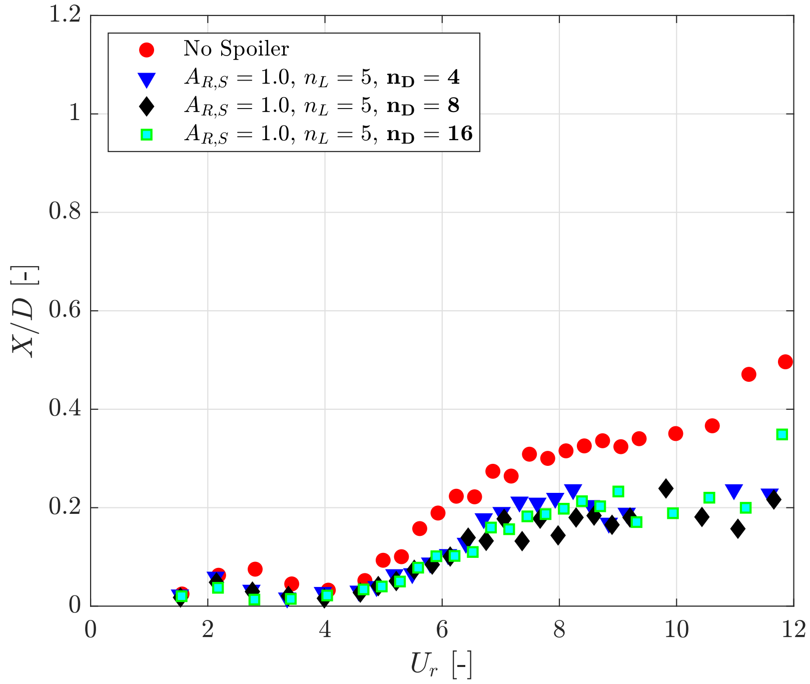

Figure 5.25: Effect of n_D on the inline non-dimensional amplitude, X/L

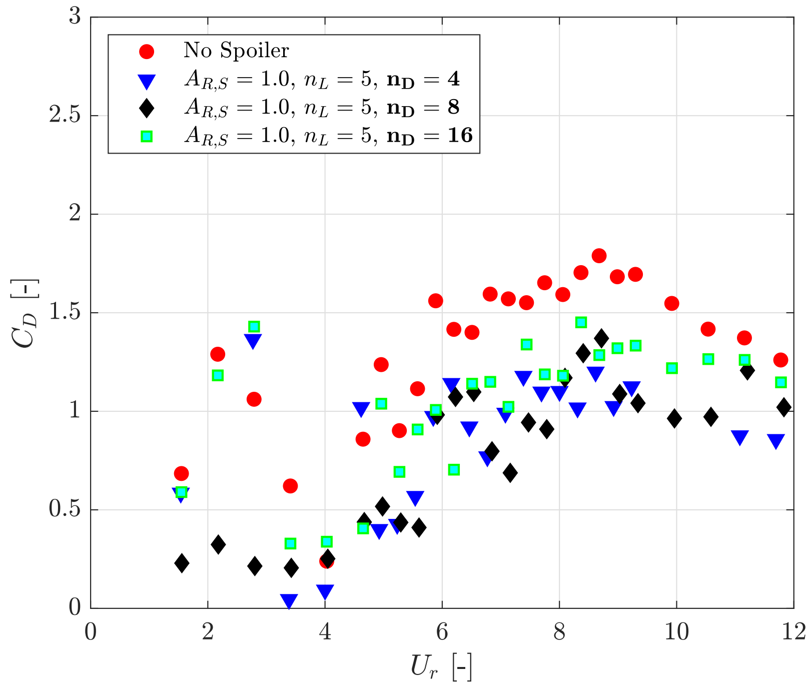

Figure 5.26: Effect of n_D on drag coefficient, C_D

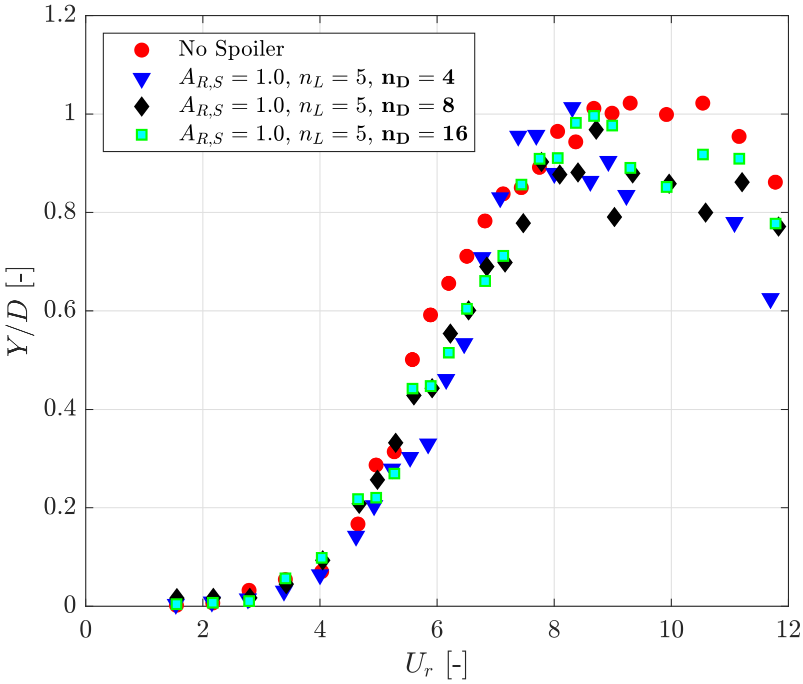

Figure 5.27: Effect of n_D on the transverse non-dimensional amplitude, Y/L

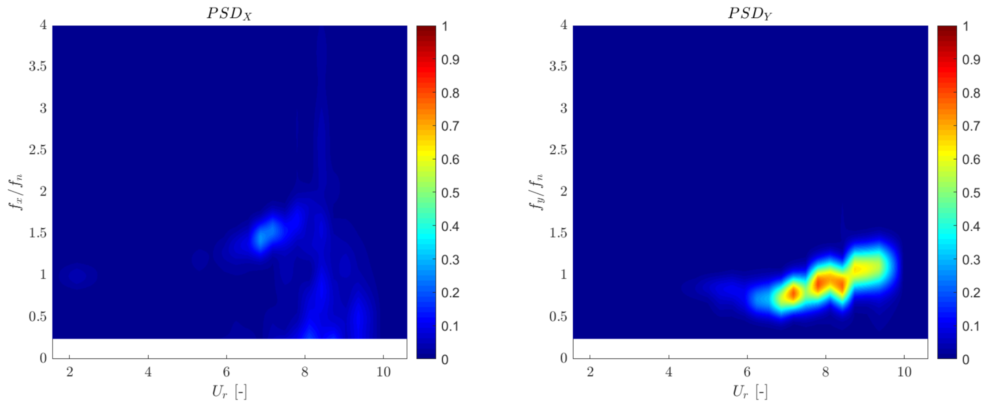

Figure 5.28: Normalized Power Spectrum Density of the motion in the inline (a) and transverse (b) direction for $A_{R,S} = 1.0$, $n_L = 5$ and $n_D = 4$

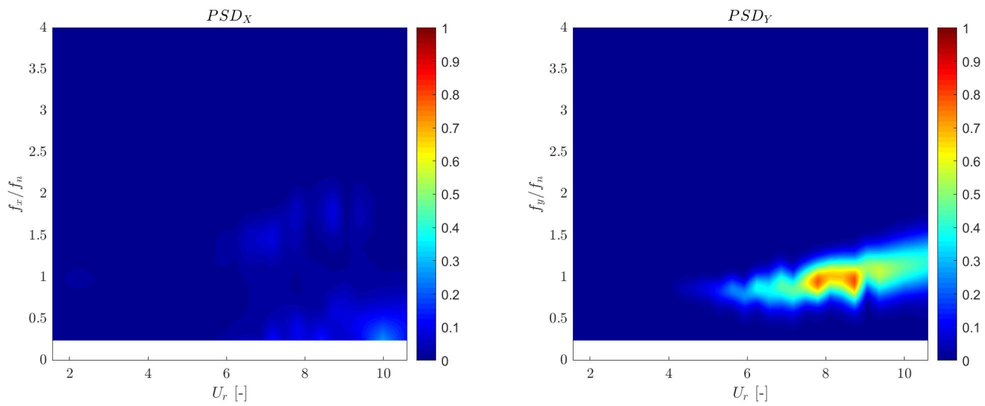

Figure 5.29: Normalized Power Spectrum Density of the motion in the inline (a) and transverse (b) direction for $A_{R,S} = 1.0$, $n_L = 5$ and $n_D = 8$

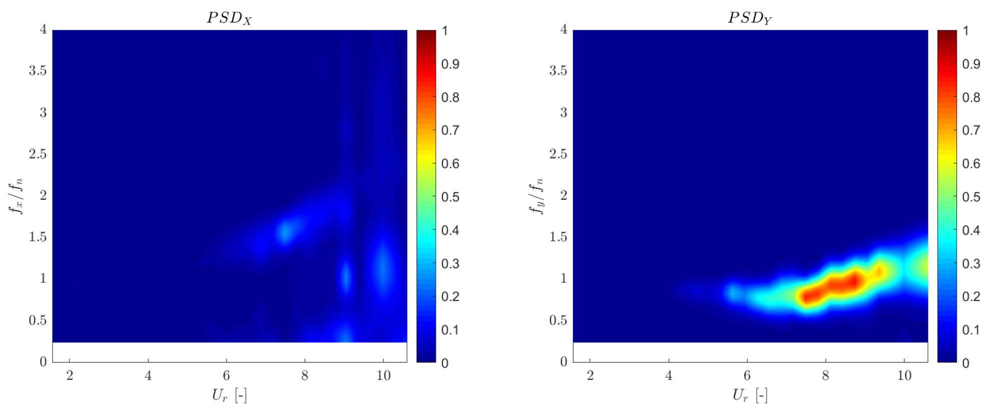

Figure 5.30: Normalized Power Spectrum Density of the motion in the inline (a) and transverse (b) direction for $A_{R,S} = 1.0$, $n_L = 5$ and $n_D = 16$

In Figure 5.26, the low amplitude range can be related to the beginning of a desynchronization region for this case. Indeed, the fluctuating drag highlights a drop in the same region, confirming the fact stated above. The low fluctuation is linked to a desynchronized behaviour for this range of reduced velocity, and then a fully mitigated FIM.

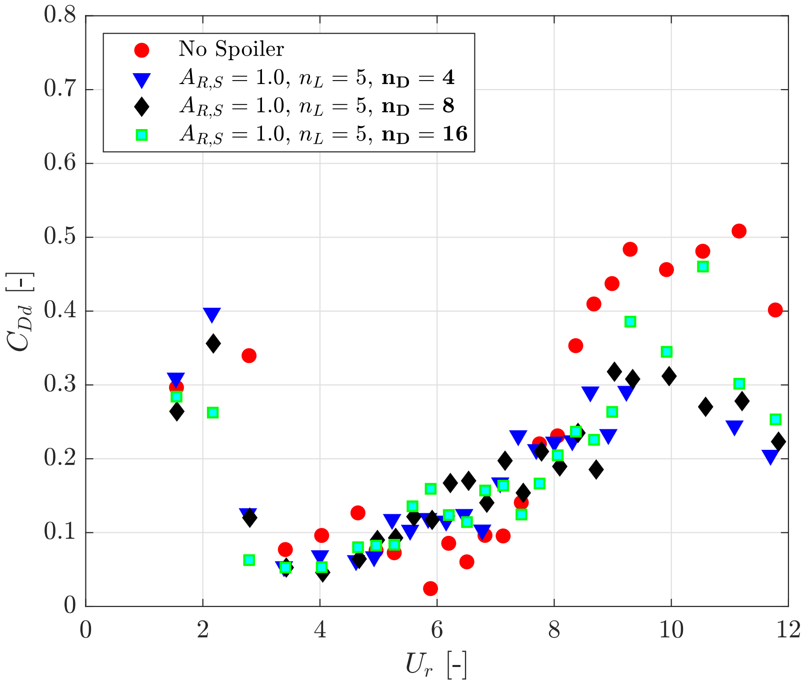

Figure 5.31: Effect of n_D on the dynamic drag coefficient, C_{Dd}

Regarding the transverse response, from the C_L for n_D=4 is not evident the reason of the drop in the transverse response for $9 < U_r < 11$ (see Figure 5.32). Whilst, the C_a is the parameter useful to understand the physics behind this drop in the motion. The n_D=4 case is the one with the lowest values of C_a for the $9 < U_r < 11$ range (see Figure 5.33), which means a clear sign of desynchronization even in the transverse direction.

The result obtained is identifying the best case in n_D=4 as the synchronization beginning is anticipated with respect to the other cases. Further analysis on this parameter will be carried out in *Stage B* to confirm this study.

The next stage of experiments has been carried out in order to confirmed the results obtained in *Stage A* for n_L and n_D studies.

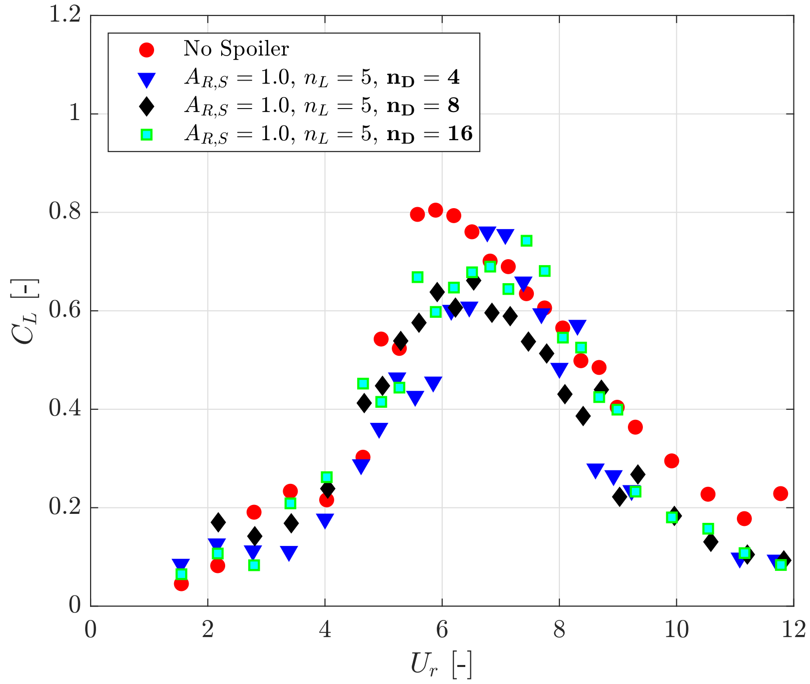

Figure 5.32: Effect of n_D on the lift coefficient, C_L

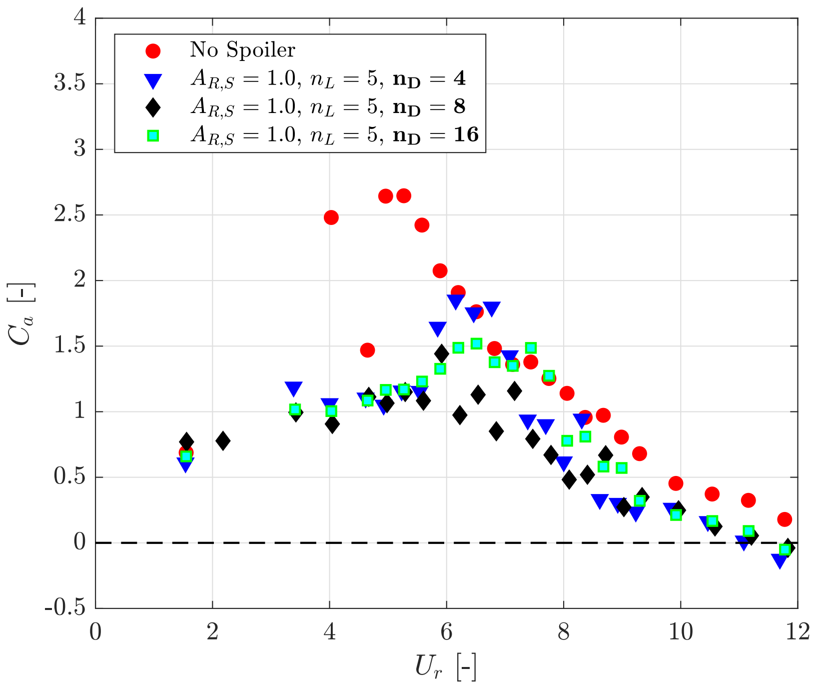

Figure 5.33: Effect of n_D on the added mass coefficient, C_a

The PSD analysis in Figure 5.28, 5.29 and 5.30, decreasing the n_D would decrease the energy of the vortices with respect to the *No Spoiler* case and shorten the *synchronization range* for the transverse case. For the inline a reduction with respect to the *No spoiler* case is evident, but the best mitigating effect is not verified for the same configuration for the transverse. n_D=4 can be considered the best configuration for the transverse according to a shortening of the *synchronization* range to $7 < U_r < 9$, so anticipating the desynchronization of the vortices. Whilst, for the inline the best mitigation is verified for n_D=8, according to a lower energy present.

5.3.3 Stage B - Parameter n_L

The following stage aims at studying the effect of the number of rings of spoiler along the immersed length of the cylinder. The parameter fixed are $A_{R,S}$=2.0 and n_D=8. The cases compared are: the *no spoiler* case together with the other three cases targeted for this stage.

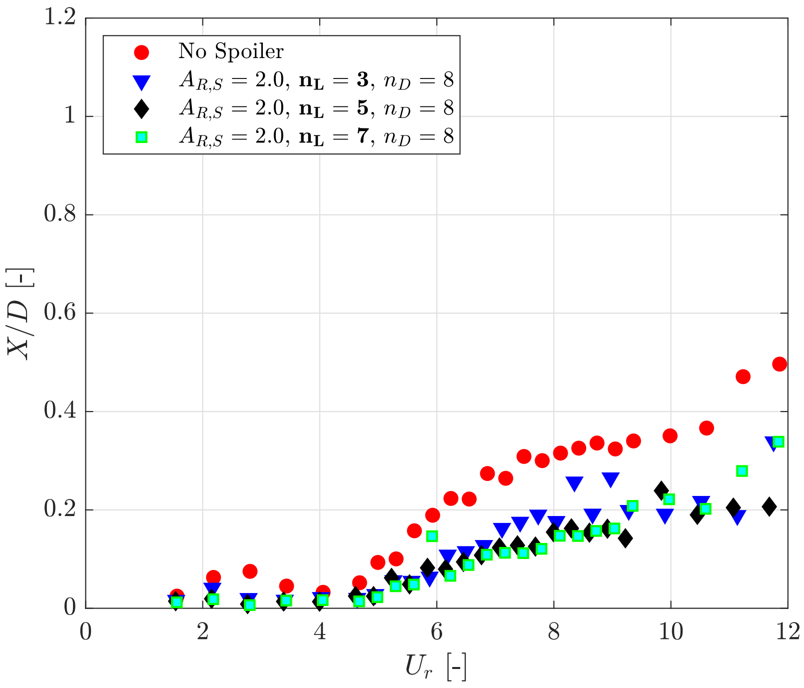

Figure 5.34: Effect of n_L on the inline non-dimensional amplitude, X/L

The results obtained in Figure 5.34 and 5.35 clarified the fact that the n_L parameter is affecting the mitigation, which is starting for $U_r > 5$. Whilst, it is not clear which parameter is the best and how the mitigation effect varied changing this parameter, as the response is similar to the one derived in *Stage A*.

The PSD analysis results are similar to the one derived in *Stage A* for the same parameter. The results are attache in Appendix B.

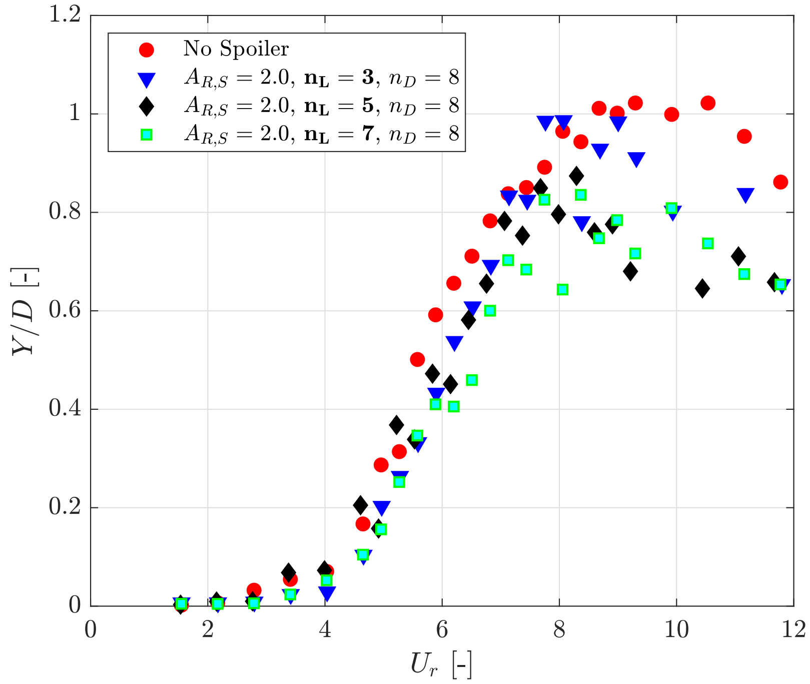

Figure 5.35: Effect of n_L on the transverse non-dimensional amplitude, Y/L

5.3.4 Stage B - Parameter n_D

The following stage aims at studying the effect of the number of plates per ring around the diameter of the cylinder. The parameter fixed are $A_{R,S}$=2.0 and n_L=5. The cases compared are: the *no spoiler* case together with the other three cases targeted for this stage.

The results obtained in Figure 5.36 and 5.37 confirmed the results obtained in *Stage A* for n_D. The difference in this case is the coupled contribute of a larger $A_{R,S}$ and a decreasing n_D. In the n_D=4 case desynchronized vortices are shed downstream the model for $U_r > 9$. This phenomenon contributes to a drop in the inline and transverse motion for FIM.

In conclusion, the best mitigating effect for both inline and transverse direction is verified while decreasing the n_D value. A smaller number of plates per ring is required to reach a desynchronization region in the range of U_r in exam.

The PSD analysis results are similar to the one derived in *Stage A* for the same parameter. The results are attached in Appendix B.

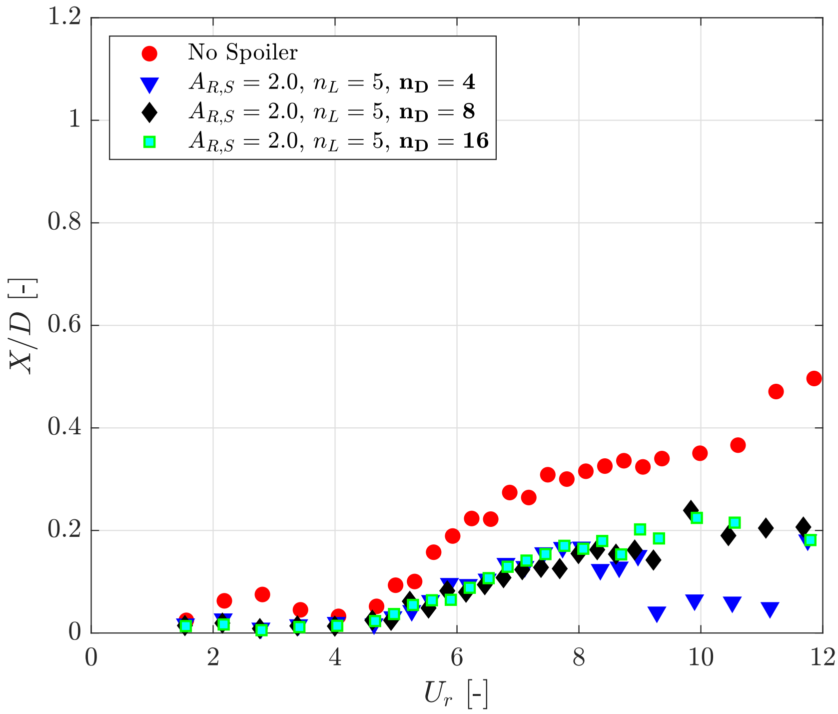

Figure 5.36: Effect of n_L on the inline non-dimensional amplitude, X/L

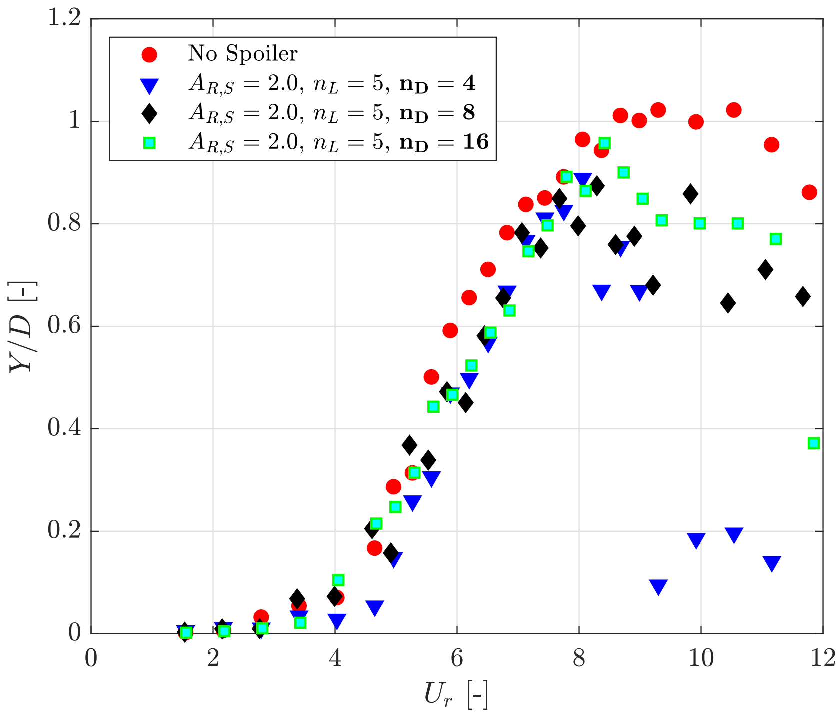

Figure 5.37: Effect of n_L on the transverse non-dimensional amplitude, Y/L

5.3.5 Stage C - Parameter n_L

The following stage aims at studying the mitigating effect parameter n_L and an optimization of the set of parameters analyzed. The parameter fixed are $A_{R,S}$ and n_D, the best parameters discovered in the previous *stages*: respectively 2.0 and 4. The cases compared are: the no spoiler case together with the other three cases targeted for this stage.

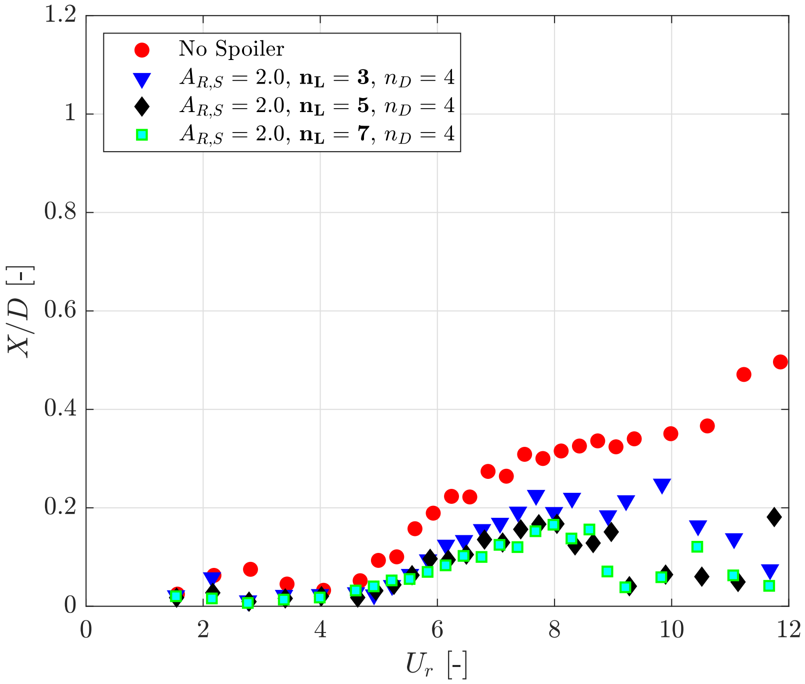

Figure 5.38: Effect of n_L on the inline non-dimensional amplitude, X/L

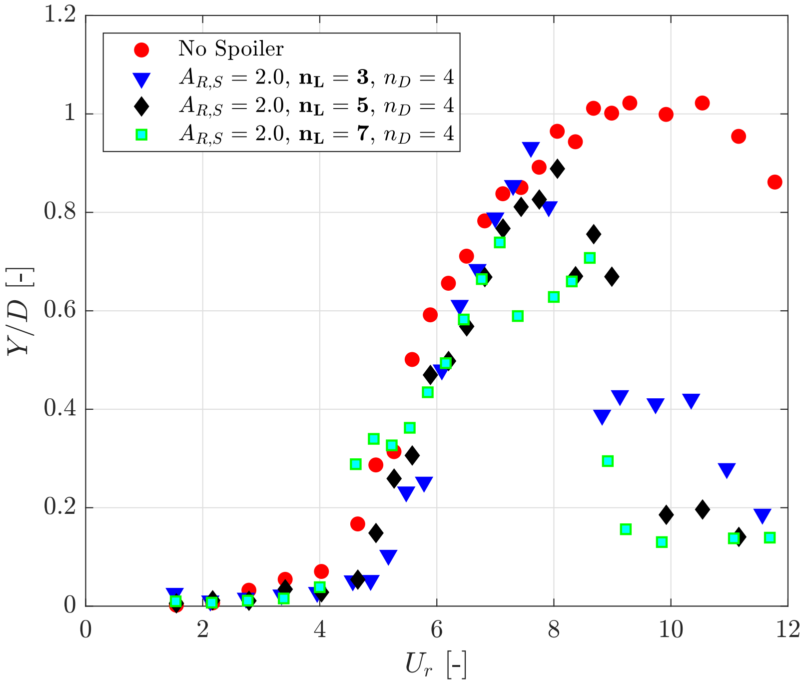

Figure 5.39: Effect of n_L on the transverse non-dimensional amplitude, Y/L

According to Figure 5.38 and 5.39, the desynchronization region for inline and transverse motion starts from reduced velocities $U_r > 8$. Contrarily from the previous stages, in this stage the best n_L can be identified. Focusing on the transverse amplitude, it is possible to understand that n_L=7 is better than n_L=5 in the range of $8 < U_r < 9$. In addition, also in the inline direction the lowest PSD value confirms a better behaviour for the n_L=7.

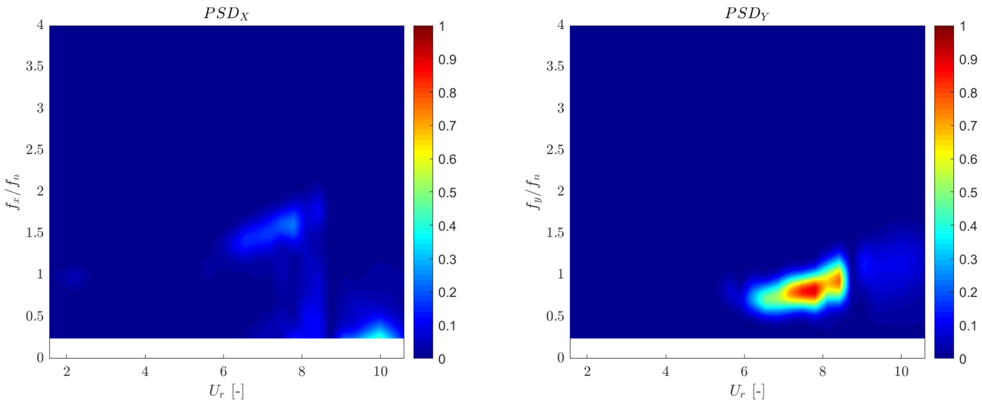

Figure 5.40: Normalized PSD of the motion in the inline (a) and transverse (b) direction for $A_{R,S} = 2.0$, $n_L = 3$ and $n_D = 4$

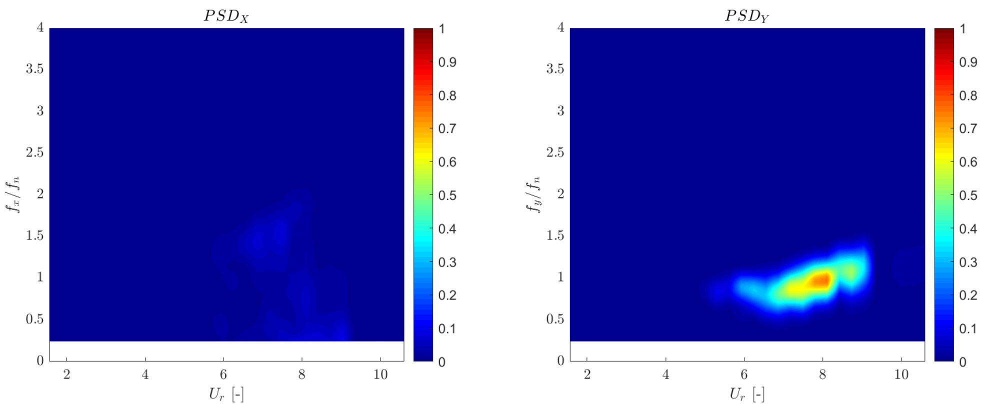

Figure 5.41: Normalized PSD of the motion in the inline (a) and transverse (b) direction for $A_{R,S} = 2.0$, $n_L = 5$ and $n_D = 4$

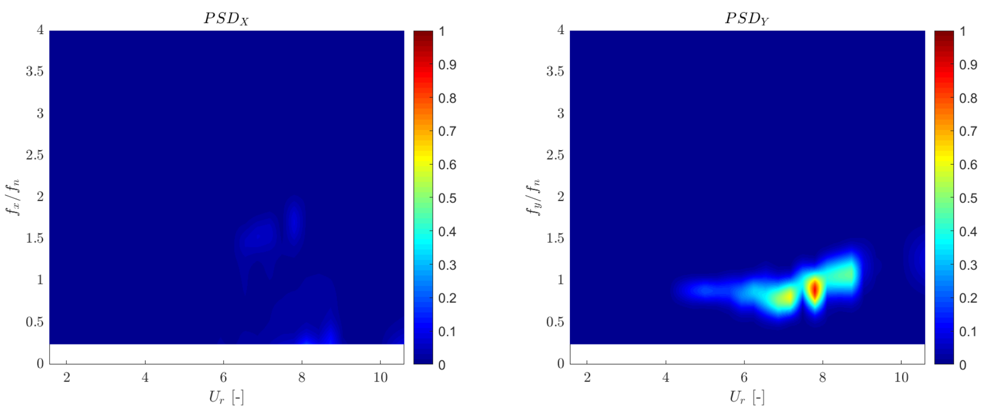

Figure 5.42: Normalized PSD of the motion in the inline (a) and transverse (b) direction for $A_{R,S} = 2.0$, $n_L = 7$ and $n_D = 4$

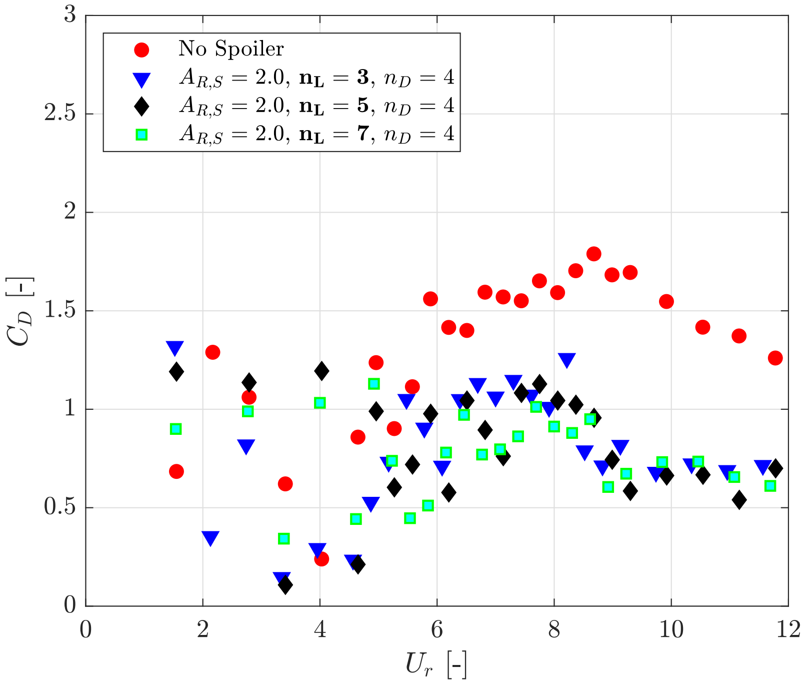

Figure 5.43: Effect of n_L on drag coefficient, C_D

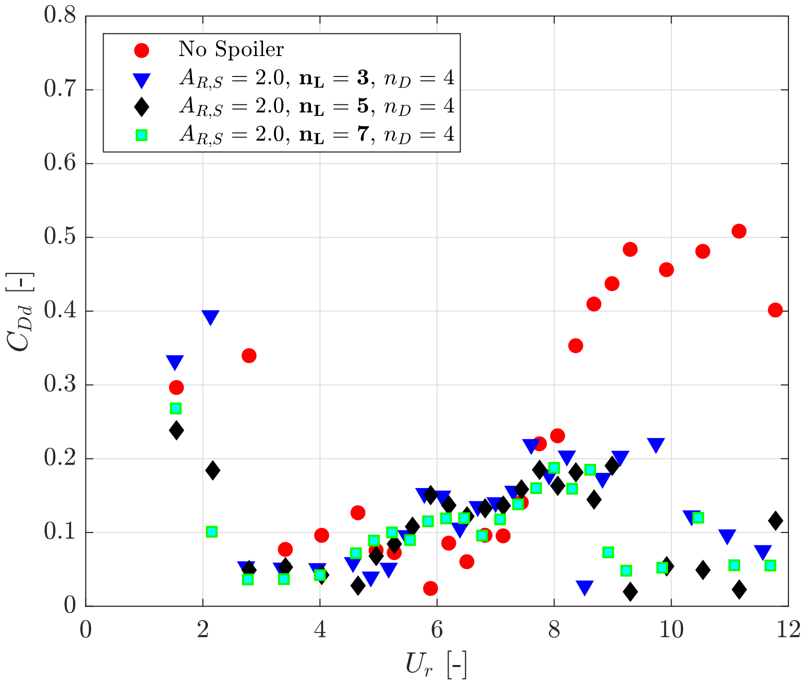

Figure 5.44: Effect of n_L on the dynamic drag coefficient, C_{Dd}

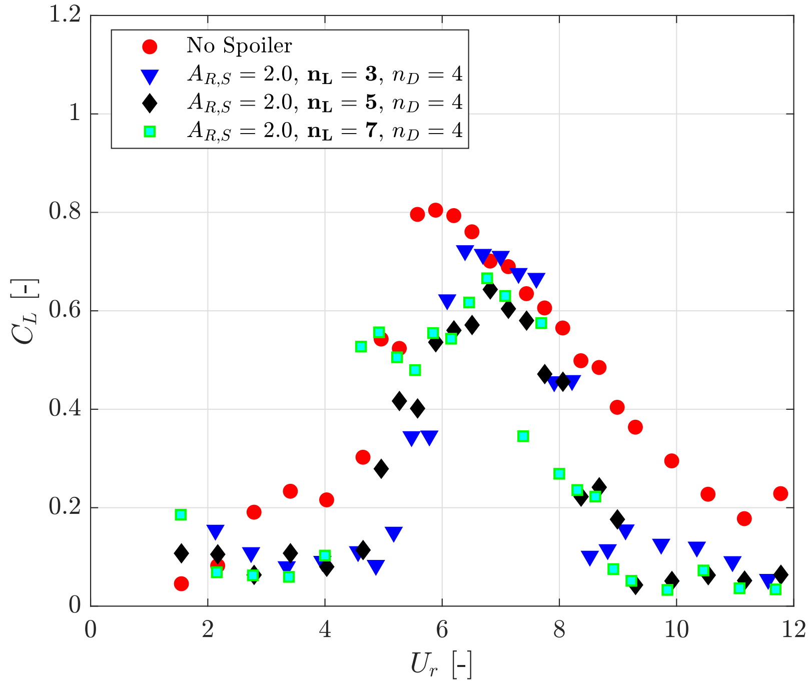

Figure 5.45: Effect of n_L on the lift coefficient, C_L

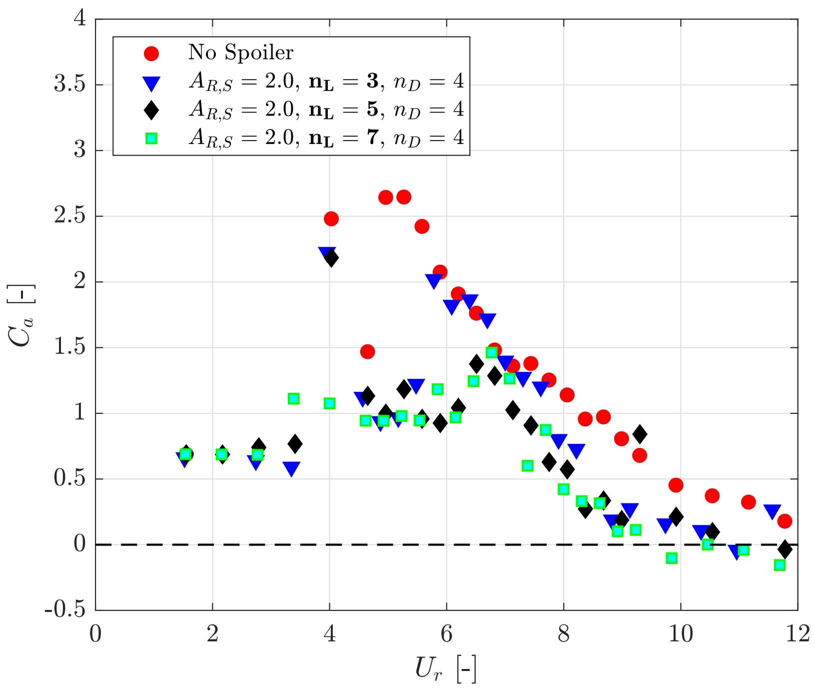

Figure 5.46: Effect of n_L on the added mass coefficient, C_a

In conclusion, for the whole stages of experiment performed, the case $A_{R,S}$=2.0, n_L=7 and n_D=4 is the most improved case (MIC). The mitigation effect with this spoiler arrangement is the most effective for this kind of platform. The anticipated desynchronization is the main factor that affects the mitigation for both inline and transverse direction. Furthermore, mitigating effects are present all over the range of study always in both direction.

Chapter 6

Conclusions

The following chapter sums up the experimental results previously obtained, comparing the benefits provided by the Most Improved Case (MIC). Additionally, the studies carried out will give the knowledge to decide which parameter is mostly affecting the FIM mitigation.

Furthermore, other aspects related to the suppression device applied have to be evaluated. According to the literature, the *free-end* effect and the *side-effect* related to the hydrodynamics of the flow around a low aspect ratio fixed cylinder, are the main reason for the vortex shedding downstream the cylinder. The characteristics of those effects will be explained in order to justify the motion amplitudes and find possible other way of FIM mitigation.

According to the lack of maturity of this subject, further hints and future studies will be proposed.

6.1 Concluding Remarks

The analysis of the results enlightened the mitigating characteristic of each parameter. *Stage A* is the parametric study of the spoiler plate mitigating effect. The best cases for each parameter are summed up in Table 6.1.

Best Parameter - Stage A			
Study	$\mathbf{A_{R,S}}$	$\mathbf{n_L}$	$\mathbf{n_D}$
$A_{R,S}$	**2.0**	5	8
n_L	1.0	**7**	8
n_D	1.0	5	**4**

Table 6.1: Best parameters confirmed in *Stage A*

Figure 6.1 and 6.2 give an estimation of the mitigating effect of each parameter. The best case of each study of *Stage A* is compared with the *no spoiler* case. This comparison shows the influence of the single parameter on the structure motion response and that each parameter has its own influence range.

According to Figure 6.1, parameter n_L and n_D are mainly effective between $5 < U_r < 9$, which is the resonance range for the platform. The reduction estimated is oscillating around Δ_X=50%. Whilst $A_{R,S}$ is performing better for $U_r > 9$, resulting in a desynchronized region for that range. This fact is suggested by an approximated value of Δ_X=90%. The reduction is not relevant up to U_r=5, as the displacements and the amplitudes are very small in that range.

Even though the reduction is verified, the inline motion amplitudes for FIM are not as big and relevant as the transverse.

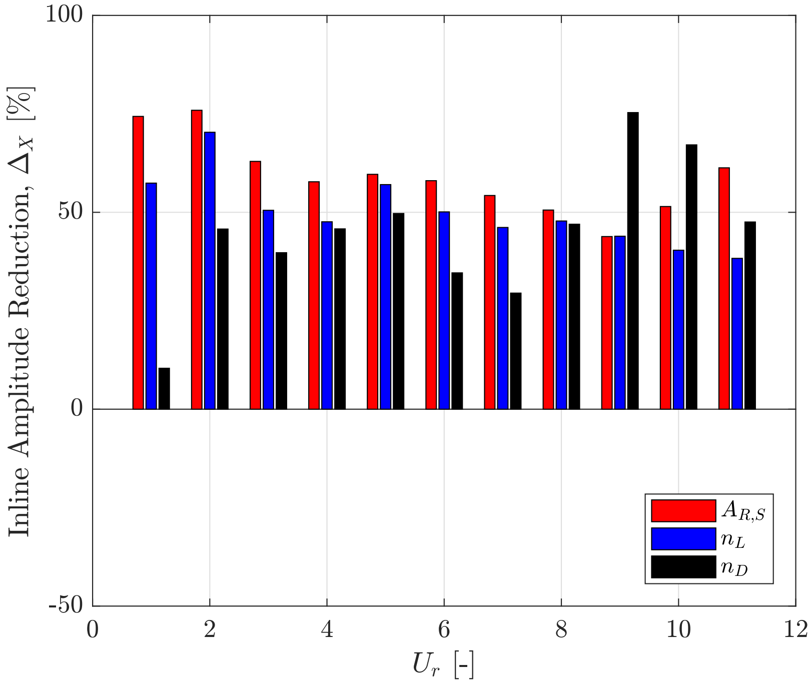

Figure 6.1: Percentage reduction of the inline motion amplitude, because of $A_{R,S}$ (red), n_L (blue) and n_D (black)

As previously stated, the transverse amplitudes are the most relevant. According to Figure 6.1, parameter n_L and n_D are mainly effective between $5 < U_r < 9$, which is in the synchronization range for the platform, as well as in the inline case, even though reduction is decreasing while approaching the resonance peak (U_r=9). The reduction estimated differs in a range of 5%$< \Delta_Y <$ 40%. Whilst, $A_{R,S}$ is performing better for $U_r > 9$, resulting in a desynchronized region for that range, as verified in the inline case. This fact is suggested by an approximated value of Δ_X=90%. As for the inline case, the reduction is not relevant up to U_r=5, as the displacements are very small in that range.

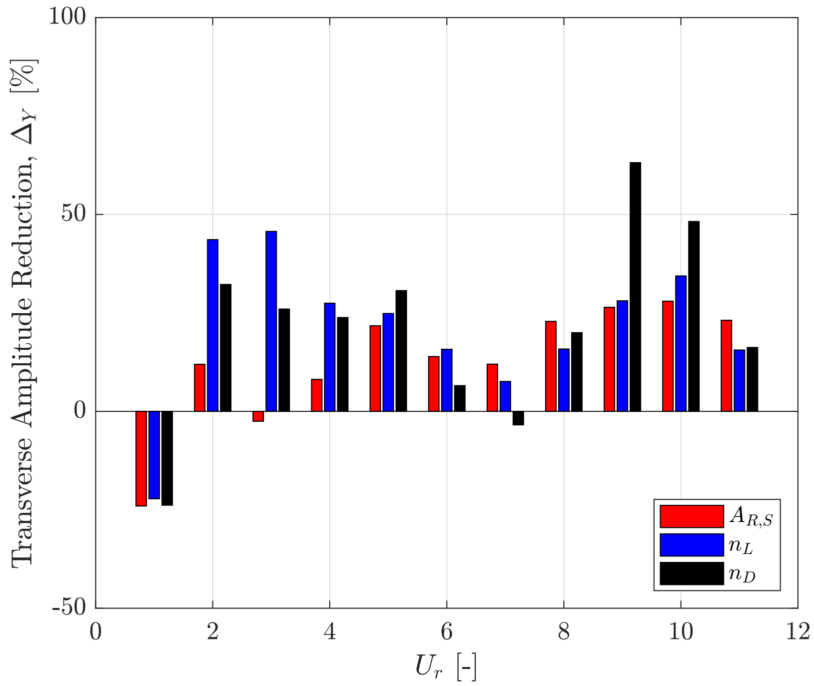

Figure 6.2: Percentage reduction of the transverse motion amplitude, because of $A_{R,S}$ (red), n_L (blue) and n_D (black)

Once extrapolated the previously deduction, it is evident which is the *Most Improved Case* (MIC), and it is possible to show and understand the response once all the parameters influences are super-positioned. Figure 6.5 shows the reduction in inline and transverse amplitudes, and how effective is the FIM mitigation in the *MIC* arrangement.

The trend of the inline and transverse reduction is similar to the one previously shown. The largest reduction is verified for inline case, even though the amplitudes are smaller compared to the transverse one. In the synchronization range the mitigation is less effective especially for the transverse case. The best performance is verified for $U_r > 9$ suggesting a desynchronization range.

In conclusion, the spoiler device is mainly affecting the inline motion, because of drastic reduction of the drag coefficient (see Figure 5.12). Whilst, the main benefit for the transverse motion mitigation is an anticipation of the desynchronization vortex shedding - platform motion.

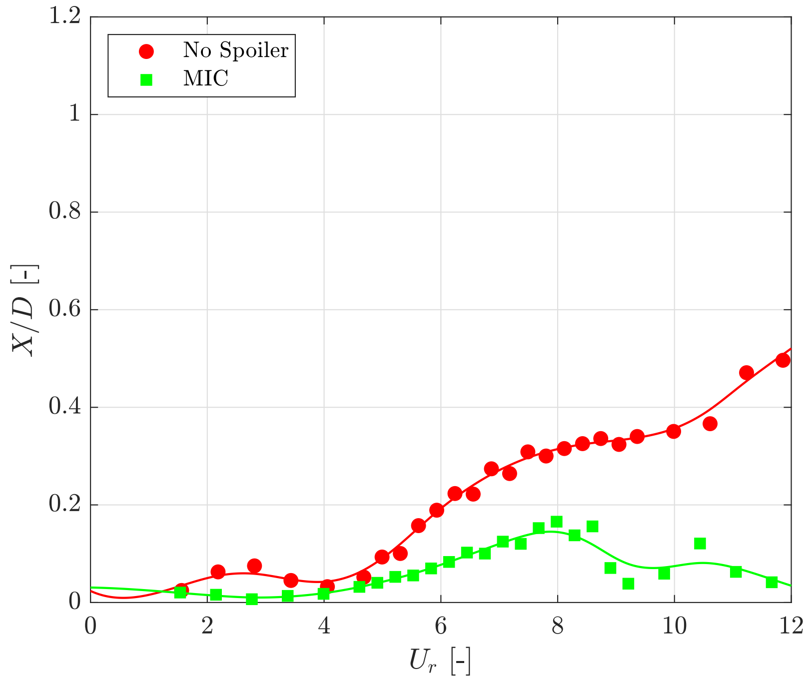

Figure 6.3: Comparison inline amplitude between the *no spoiler* case and the *MIC*

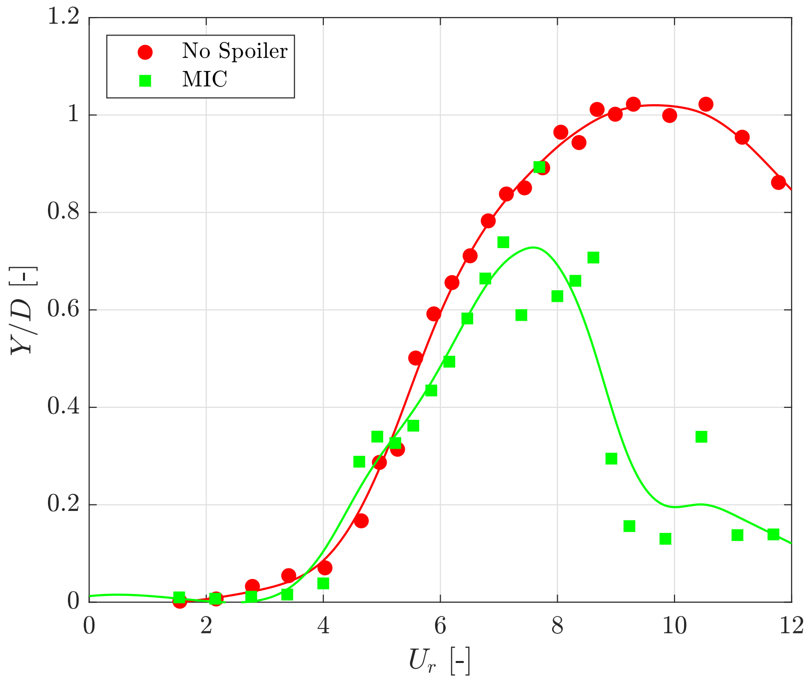

Figure 6.4: Comparison inline amplitude between the *no spoiler* case and the *MIC*

One of the reason of this constraint on the transverse mitigation effect of the spoiler plates, could be related to the position and the type of vortices created. As

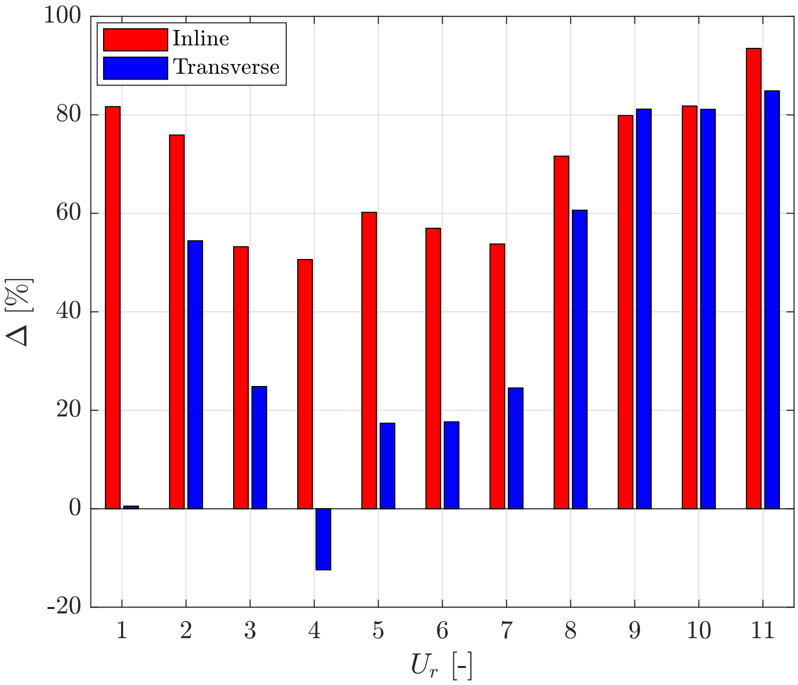

Figure 6.5: Percentage reduction in the inline (red) and transverse (blue) motion amplitude, comparing the *No spoiler* case and the *MIC*

the spoiler are arranged on the side of the cylinder, mainly the vorticity created in that area is suppressed. Several works in literature tried to evaluate experimentally and numerically - respectively through PIV test and CFD simulations - the characteristics of the vortices shed in the wake of a fixed cylinder and their pattern. The results is the discover of the presence of not just 2D vortices, but also 3D vortices created by the free-end of the platform.

The 3D vortices generation is related to a formation of stagnation and recirculating area in specific position in the wake of the cylinder. These stagnation points, or *bubbles*, let the flow circulate around them with consequent creation of recirculating flow. As investigated in the work of Gonçalves et al. [9], for fixed cylinder A_R=1.5 the vortex shedding is dominated by von Kármán vortices in the streamwise direction and is also affected by vortices originated from the free-end of the cylinder.

According to Kawamura et al. [13], the free-end vortices are generated because of a *bubble* located under the bottom of the cylinder. These vortices are distinguished in *blow-up* and *recirculating* vortices.

Figure 6.6 illustrates a sketch of the vortices created and the location of the *bubbles*: the bubble are located under the free-end and on the side of the cylinder.

The vortex structures are affecting the motion of the cylinder and their effects are distinguished according to where they originated: *side effect* and *free-end effect*.

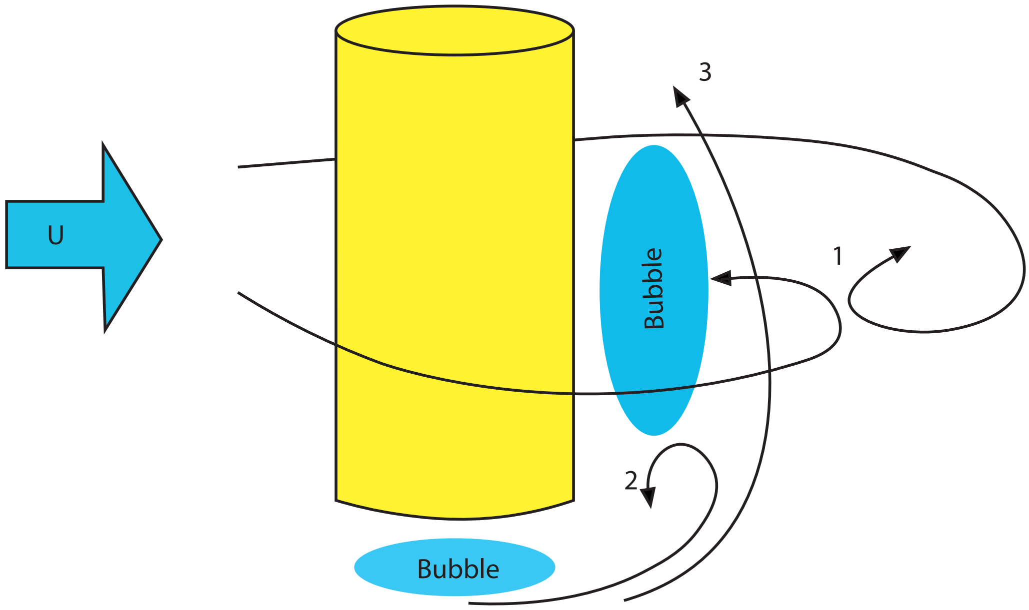

Figure 6.6: Sketch of the vortex structure in the wake of a cylinder: von Kármán (1), recirculating (2) and blow-up (3)

The intensity of the effect is strongly related to the aspect ratio of the structure. The larger the aspect ratio the larger the contribute in the motion of the side vortices and the smaller the contribute of the free-end vortices, and viceversa (see Figure 6.7). For aspect ratio $0.75 < A_R < 1.5$ both the von Kármán and the free-end characteristics are present. For $A_R < 0.75$ the free-end vortices are predominant.

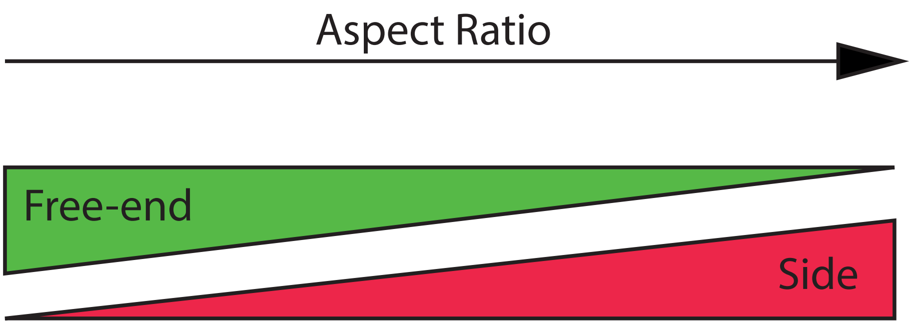

Figure 6.7: Illustration of the dependence of the vortex origin with the aspect ratio

Part of the works are associated to fixed cylinder case and not floating, but similarities can be hypothesized. Figure 6.8 compares different transverse amplitude response for floating ($m^* = 1$) cylinders of different aspect ratio.

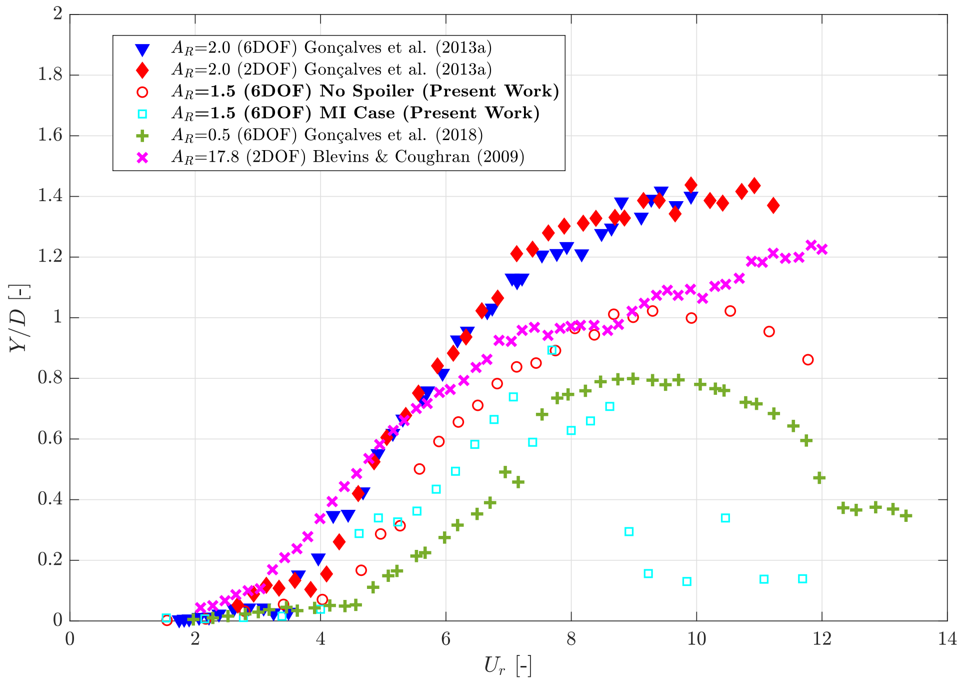

Figure 6.8: Effect of the vortices characteristics on different aspect ratio, A_R, cylinders

Comparing the amplitude of A_R=17.8, considered as an *"infinite cylinder"*, A_R=2.0 and A_R=0.5, it is reasonable to say that the phenomena stated for the fixed case can be also associated for the floating case. The reason is that for A_R=2.0 the amplitude is higher as both the vortices contributes are present, whilst lower for A_R=17.8 and A_R=0.5, whose stronger characteristics of the vortices are respectively side and free-end.

The *Most Improved Case* transverse amplitude response is between this two cases. The motion amplitude is reduced compared to the case without spoiler, probably because of a suppression of the side vortices. Comparing with the A_R=0.5, in the synchronization range the amplitude is high because of the free-end vortices as the trend and the amplitude values are similar.

The results and the conclusion obtained are evaluated in order to show the response of this kind of model in a fundamental way. The full scale case is not concern of this work, and for the implication of this mitigation device a further evaluation regarding the current velocity field must be assessed.

6.2 Future Works

One of the interesting point that came out of this discussion is the lack of literature regarding spoiler plates and their application. Furthermore, the numerical calculation for floating cylinder in current condition are in developing phase, so new methods should be defined.

A CFD simulation of the present case would confirm and could be validated in order to reduce the time cost taken by the experiment. Once a numerical method for 6DOF, floating and current condition case is developed, it would be possible to confirm the characteristics of the vortices shed in the wake of the cylinder and to collocate the mitigation devices where they are required and they could be more effective.

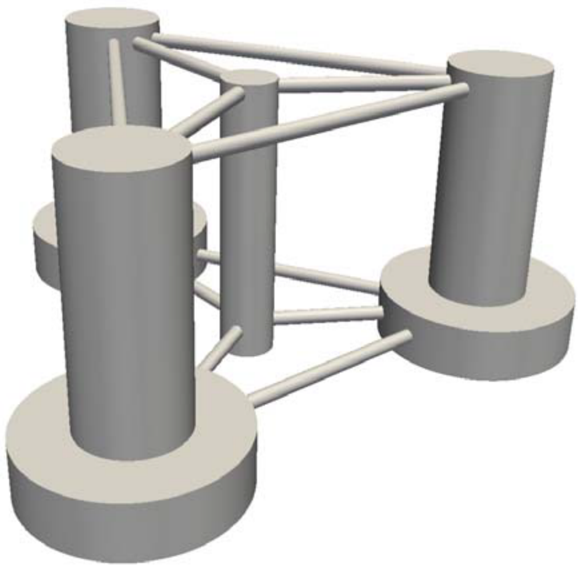

Figure 6.9: OC4 concept

Furthermore, the increasing exploitation of low aspect ratio cylindrical structures for offshore platform would require further studies and investigation related to *fluid-structure interaction* and, particularly, FIM. Mitigation devices should be tested on new generation platform models, i.e. OC4 (see Figure 6.9), in order to verify the effectiveness of the device for other and more complex geometry of platform.

Other works that can be developed are further studies related to the *free-end effect*, as could be the most influencing effect for the FIM in this type of platform.

Bibliography

[1] Agency, I. E. (2018). Weo 2018 special report offshore energy outlook. Technical report, IEA.

[2] Antony, A., Parambath, A., Yue, B., Man, K., Thethi, R., et al. (2017). Cost savings associated with improved vim prediction accuracy. In *Offshore Technology Conference*. Offshore Technology Conference.

[3] Blevins, R. D. (1984). Applied fluid dynamics handbook. *New York, Van Nostrand Reinhold Co., 1984, 568 p.*

[4] Castro-Santos, L. and Diaz-Casas, V. (2016). *Floating offshore wind farms*. Springer.

[5] Fredsoe, J. and Sumer, M. (1997). Hydrodynamics around cylindrical structures.

[6] Fujarra, A. L. and Pesce, C. P. (2002). Added mass of elastically mounted rigid cylinder in water subjected to vortex-induced vibrations. In *ASME 2002 21st International Conference on Offshore Mechanics and Arctic Engineering*, pages 661–666. American Society of Mechanical Engineers.

[7] Fujarra, A. L., Rosetti, G. F., de Wilde, J., and Gonçalves, R. T. (2012). State-of-art on vortex-induced motion: A comprehensive survey after more than one decade of experimental investigation. In *ASME 2012 31st International Conference on Ocean, Offshore and Arctic Engineering*, pages 561–582. American Society of Mechanical Engineers.

[8] Gao, Z., Guachamin Acero, W., Li, L., Zhao, Y., Li, C., and Moan, T. (2016). Numerical simulation of marine operations and prediction of operability using response-based criteria with an application to installation of offshore wind turbine support structures. In *Proceedings of the Third Marine Operations Specialty Symposium (MOSS2016), September*, pages 20–21.

[9] Gonçalves, R., Franzini, G. R., Rosetti, G. F., Meneghini, J. R., and Fujarra, A. L. C. (2015). Flow around circular cylinders with very low aspect ratio. *Journal of Fluids and Structures*, 54:122–141.

[10] Gonçalves, R. T., Fujarra, A. L., Rosetti, G. F., and Nishimoto, K. (2010). Mitigation of vortex-induced motion (vim) on a monocolumn platform: forces and movements. *Journal of Offshore Mechanics and Arctic Engineering*, 132(4):041102.

[11] Gonçalves, R. T., Meneghini, J. R., and Fujarra, A. L. (2018). Vortex-induced vibration of floating circular cylinders with very low aspect ratio. *Ocean Engineering*, 154:234–251.

[12] Huang, S., Khorasanchi, M., and Herfjord, K. (2011). Drag amplification of long flexible riser models undergoing multi-mode viv in uniform currents. *Journal of Fluids and Structures*, 27(3):342–353.

[13] Kawamura, T., HIWADA, M., HIBINO, T., MABUCHI, I., and KUMADA, M. (1984). Flow around a finite circular cylinder on a flat plate: Cylinder height greater than turbulent boundary layer thickness. *Bulletin of JSME*, 27(232):2142–2151.

[14] Kokkinis, T., Sandstrom, R., Jones, H., Thompson, H., and Greiner, W. (2004). Development of a stepped line tensioning solution for mitigating vim effects in loop eddy currents for the genesis spar. In *ASME 2004 23rd International Conference on Offshore Mechanics and Arctic Engineering*, pages 995–1004. American Society of Mechanical Engineers.

[15] Kozakiewicz, A., Sumer, B. M., Fredsøe, J., Hansen, E. A., et al. (1997). Vortex regimes around a freely vibrating cylinder in oscillatory flow. *International Journal of Offshore and Polar Engineering*, 7(02).

[16] Lee, H. S., Yamashita, T., Komaguchi, T., and Mishima, T. (2011). Storm surge in seto inland sea with consideration of the impacts of wave breaking on surface currents. *Coastal Engineering Proceedings*, 1(32):17.

[17] of Denmark, D. T. U. (June 2019). Global wind atlas. `https://globalwindatlas.info/`.

[18] Otsuka, A. (2016). *Regional Energy Demand and Energy Efficiency in Japan: An Application of Economic Analysis*. Springer.

[19] Pattenden, R., Turnock, S., and Zhang, X. (2005). Measurements of the flow over a low-aspect-ratio cylinder mounted on a ground plane. *Experiments in Fluids*, 39(1):10–21.

[20] Roshko, A. (1961). Experiments on the flow past a circular cylinder at very high reynolds number. *Journal of Fluid Mechanics*, 10(3):345–356.

[21] Sarpkaya, T. (2004). A critical review of the intrinsic nature of vortex-induced vibrations. *Journal of fluids and structures*, 19(4):389–447.

[22] Schewe, G. (1983). On the force fluctuations acting on a circular cylinder in crossflow from subcritical up to transcritical reynolds numbers. *Journal of fluid mechanics*, 133:265–285.

[23] Smith, D. W., Thompson, H., Kokkinis, T., and Greiner, W. (2004). Hindcasting vim-induced mooring fatigue for the genesis spar. In *ASME 2004 23rd International Conference on Offshore Mechanics and Arctic Engineering*, pages 1005–1014. American Society of Mechanical Engineers.

[24] Stappenbelt, B. (2010). *Vortex-Induced Motion of Nonlinear Offshore Structures*. Lambert Academic Publishing, LAP.

[25] Stappenbelt, B., O'Neill, L., et al. (2007). Vortex-induced vibration of cylindrical structures with low mass ratio. In *The Seventeenth International Offshore and Polar Engineering Conference*. International Society of Offshore and Polar Engineers.

[26] Takao Inui, Hisashi Kajitani, S. K. T. M. S. O. (1968). The new carriage and facilities of the experimental tank of the university of tokyo. Technical report, The University of Tokyo.

[27] Trust, T. C. (June 2015). Floating offshore wind: Market and technology review. Technical report.

[28] Van Dyke, M. and Van Dyke, M. (1982). An album of fluid motion.

[29] Vikestad, K., Vandiver, J., and Larsen, C. (2000). Added mass and oscillation frequency for a circular cylinder subjected to vortex-induced vibrations and external disturbance. *Journal of Fluids and Structures*, 14(7):1071–1088.

[30] Welch, P. (1967). The use of fast fourier transform for the estimation of power spectra: a method based on time averaging over short, modified periodograms. *IEEE Transactions on audio and electroacoustics*, 15(2):70–73.

[31] Williamson, C. and Govardhan, R. (2008). A brief review of recent results in vortex-induced vibrations. *Journal of Wind engineering and industrial Aerodynamics*, 96(6-7):713–735.

[32] Williamson, C. H. (1989). Oblique and parallel modes of vortex shedding in the wake of a circular cylinder at low reynolds numbers. *Journal of Fluid Mechanics*, 206:579–627.

[33] Wind, I. (2017). Annual report 2017. Technical report, IEA Wind.

Appendix A

Design Details

A.1 Metacenter Calculation

The metacenter of a cylindrical floater can be calculated as:

$$M = B + \frac{I_A}{V_D}, \tag{A.1}$$

where B is coordinate of the centre of buoyancy of the body, I_A is the secon moment of inertia of a cylinder and V_D is the water displacement.The second moment of inertia has been calculated as:

$$I_A = \pi \frac{D^4}{32}, \tag{A.2}$$

where D is the diameter of the cylinder. The metacentric height, GM, is derived as the distance between the metacenter and the center of gravity of the floater:

$$GM = G - M. \tag{A.3}$$

A.2 Blockage Effect

According to the definition described in Chapter 4, the blockage effect coefficient, B_e, is the contribute of the boundaries of the tank's wall on the result of the experiment. this coefficient take in to account both the effects of the side and the bottom of the tank. This value is calculated as:

$$B_e = \frac{L \cdot D}{W_T \cdot D_T}, \tag{A.4}$$

Where L is the immersed length of the body and D is its diameter. W_T and D_T are, respectively, width and depth of the tank facility.

A.3 Spoiler Plates Design

In order to ensure the attachment of the spoiler plates to the model surface a preliminary design has been assessed considering the most conservative case: the highest aspect ratio for the spoiler plate and the highest velocity. According to the magnet designing the following hypothesis, estimated by other works in literature, has been taken:

Magnet Design			
Maximum Current Speed	U	m/s	0.4
Maximum Flow Velocity at Model Surface	U_S	m/s	0.8
Maximum Fluctuating Flow Velocity	U_{max}	m/s	1.6
Spoiler Drag Coefficient	$C_{D,S}$	[-]	2
Maximum Length	b	mm	10
Maximum Width	a	mm	20

Table A.1: Magnet design

The maximum force acting on the spoiler, F_X^{max} has been calculated according to the following formula:

$$F_X^{max} = \frac{1}{2} C_{D_S} \rho U_{max}^2 a \cdot b \tag{A.5}$$

The factory standard for neodymium magnets are related to a fixed size (3mmx3mmx10mm) and summed up in the table below:

Neodymium Factory Standard		
Attaching Force	kgf	0.991
Attaching Stress	$N \cdot mm^2$	**0.324**

Table A.2: Neodymium magnet factory standard

Once having all these values, overturning moment and bending stress for the highest aspect ratio case have been calculated, with the following result:

Forces acting on the spoiler		
Drag Force acting on the Spoiler	kgf	0.512
Overturning Moment	$N \cdot mm$	5.12
Bending Stress	$N \cdot mm^2$	**0.256**

Table A.3: Forces values acting in current condition on the spoiler plate

In conclusion, the feasibility of the design is ensured, as the estimated bending stress is lower than the attachment force of the Neodymium magnet.

Appendix B

Additional Results

B.1 Stage A - Parameter n_L

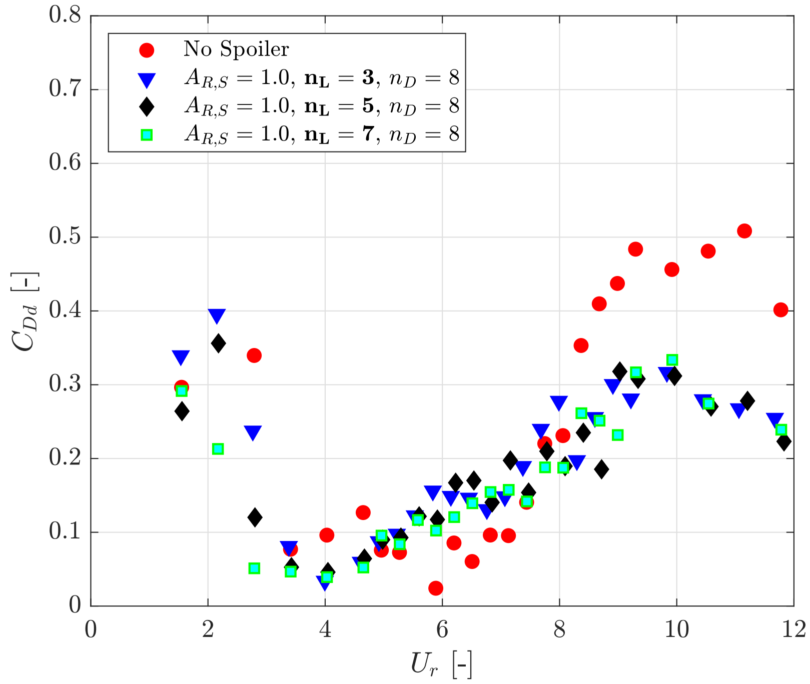

Figure B.1: Effect of n_L on the dynamic drag coefficient, C_{Dd}

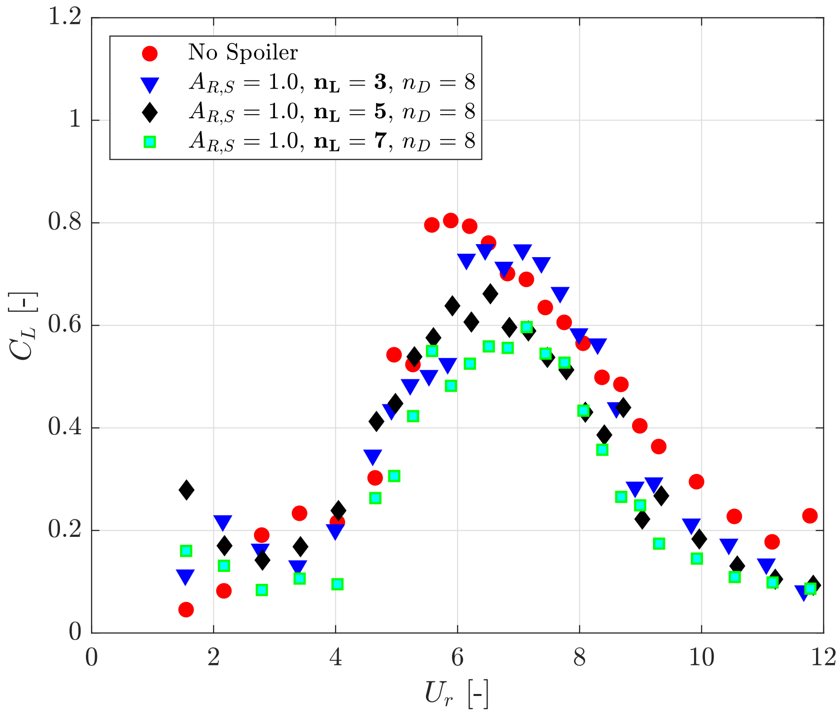

Figure B.2: Effect of n_L on the lift coefficient, C_L

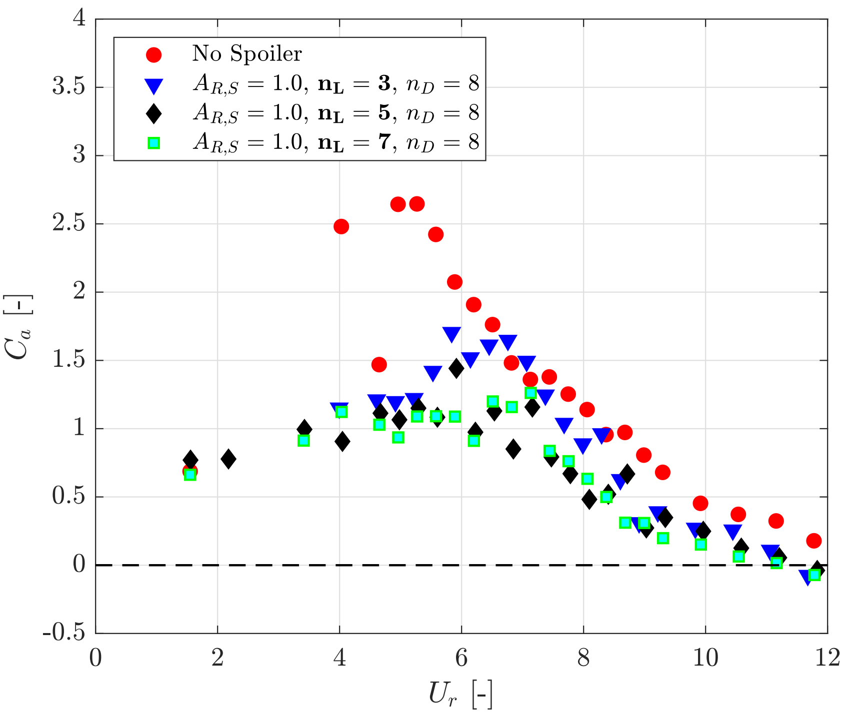

Figure B.3: Effect of n_L on the added mass coefficient, C_a

B.2 Stage B - Parameter n_L

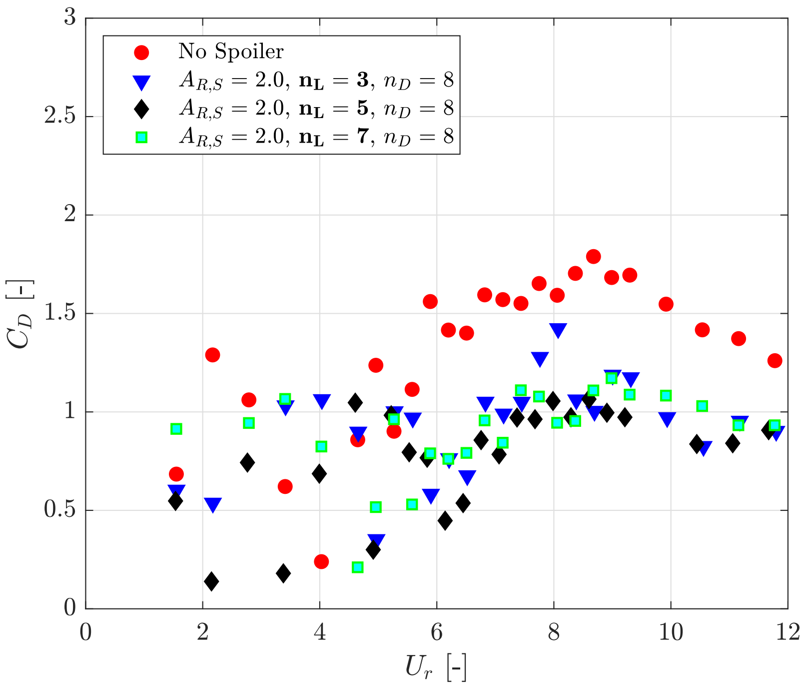

Figure B.4: Effect of n_L on drag coefficient, C_D

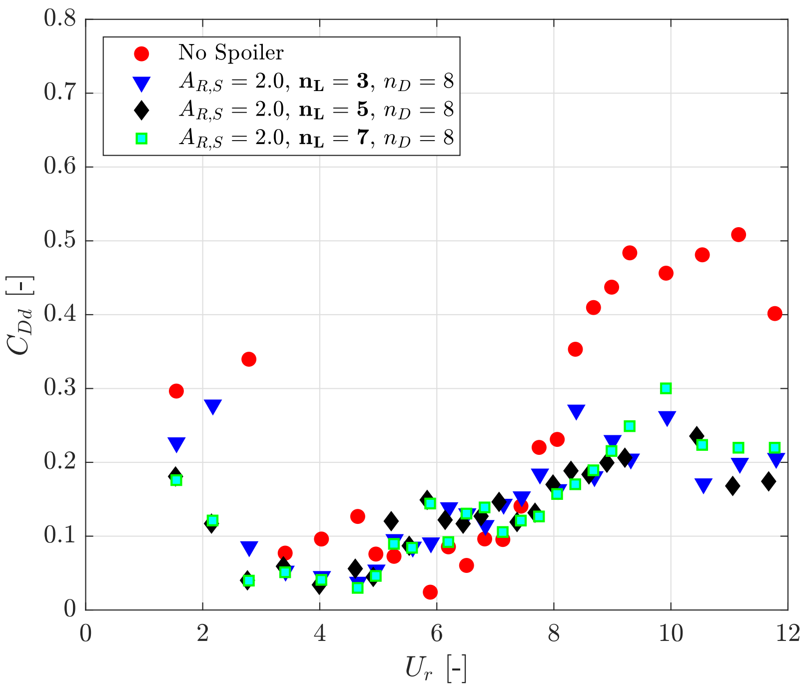

Figure B.5: Effect of n_L on the dynamic drag coefficient, C_{Dd}

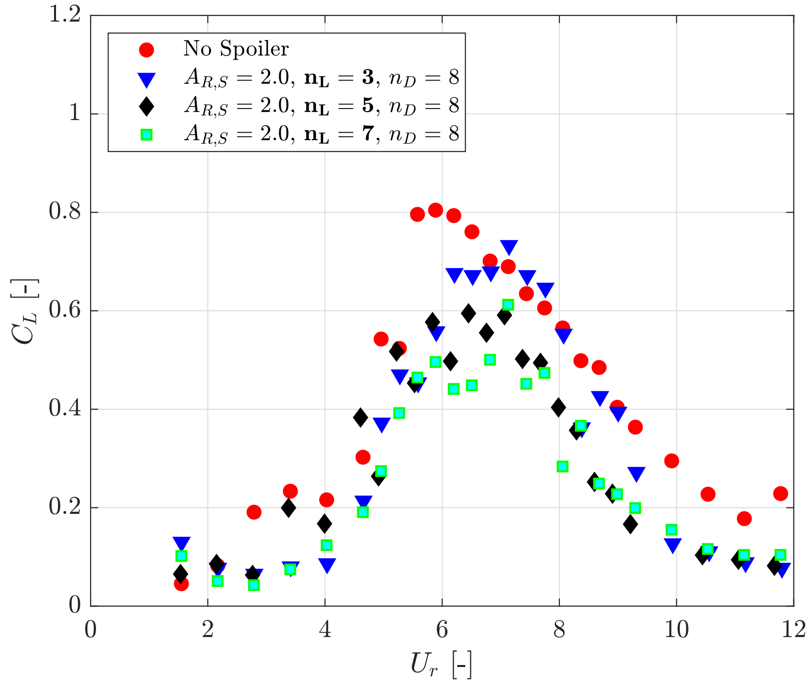

Figure B.6: Effect of n_L on the lift coefficient, C_L

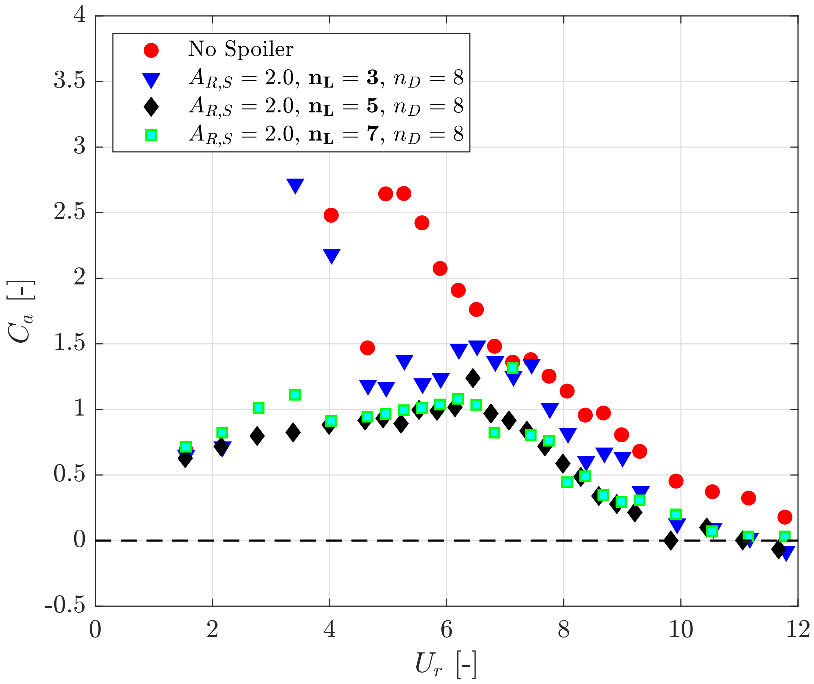

Figure B.7: Effect of n_L on the added mass coefficient, C_a

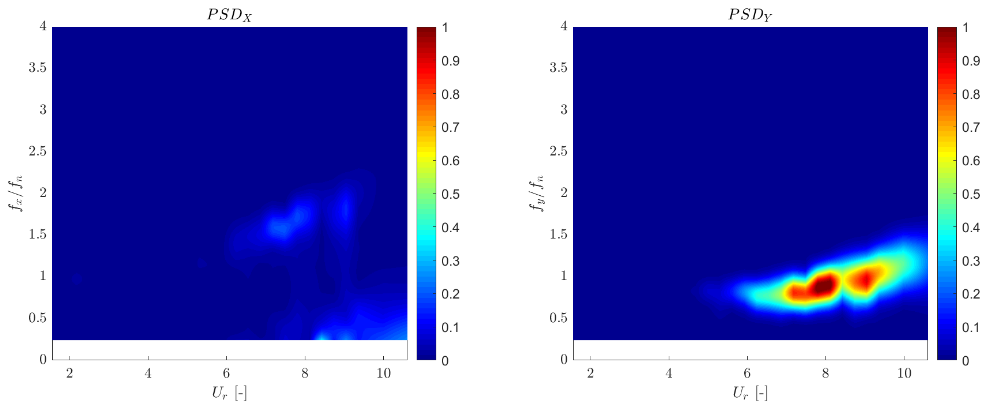

Figure B.8: Normalized Power Spectrum Density of the motion in the inline (a) and transverse (b) direction for $A_{R,S} = 2.0$, $n_L = 3$ and $n_D = 8$

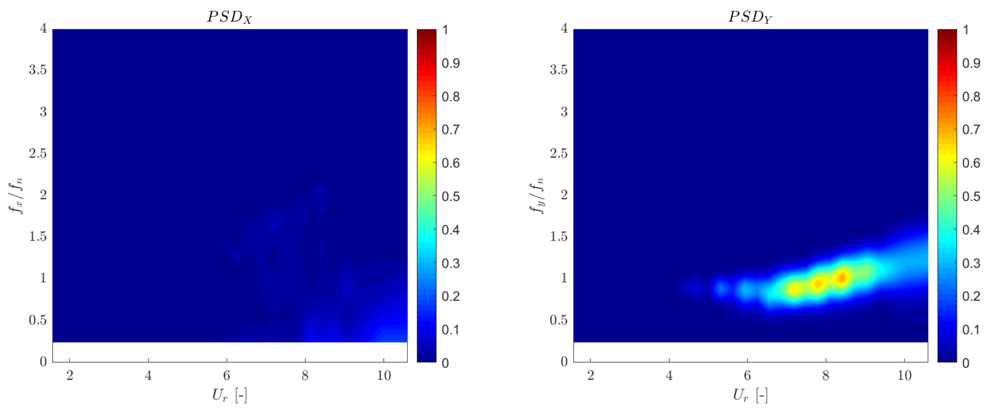

Figure B.9: Normalized Power Spectrum Density of the motion in the inline (a) and transverse (b) direction for $A_{R,S} = 2.0$, $n_L = 5$ and $n_D = 8$

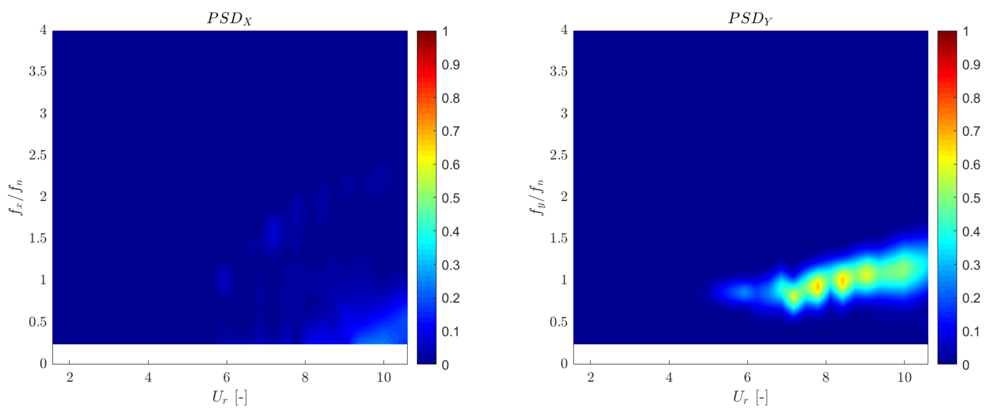

Figure B.10: Normalized Power Spectrum Density of the motion in the inline (a) and transverse (b) direction for $A_{R,S} = 2.0$, $n_L = 7$ and $n_D = 8$

B.3 Stage B - Parameter n_D

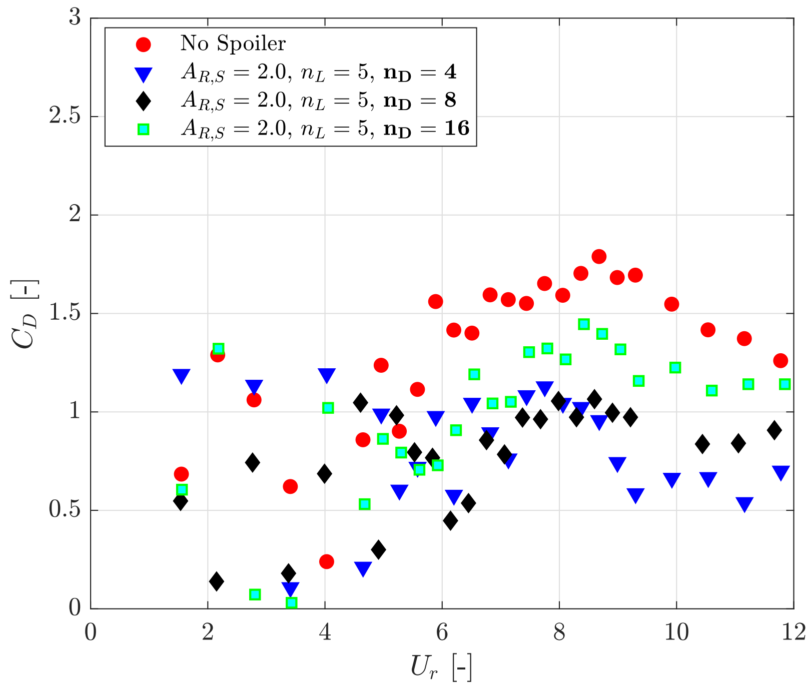

Figure B.11: Effect of n_D on drag coefficient, C_D

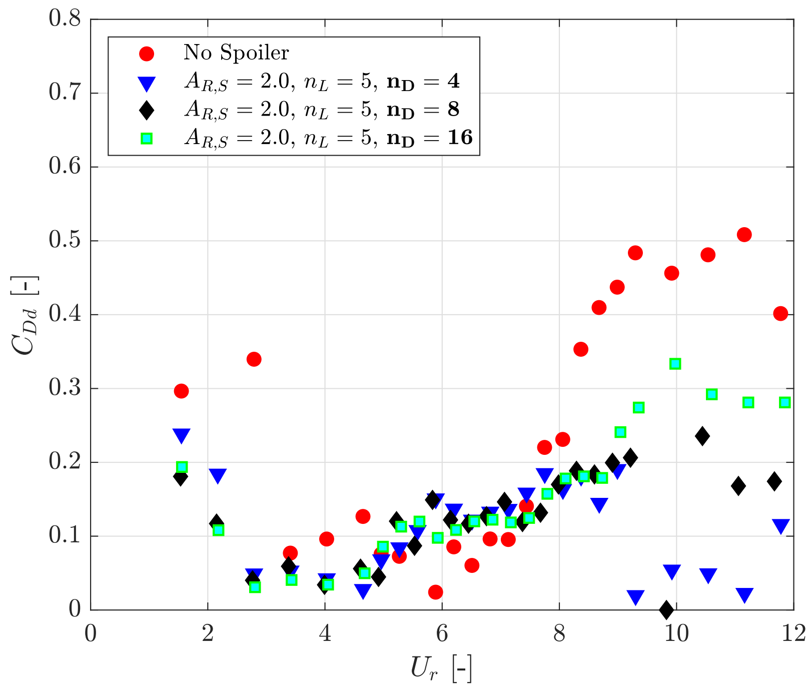

Figure B.12: Effect of n_D on the dynamic drag coefficient, C_{Dd}

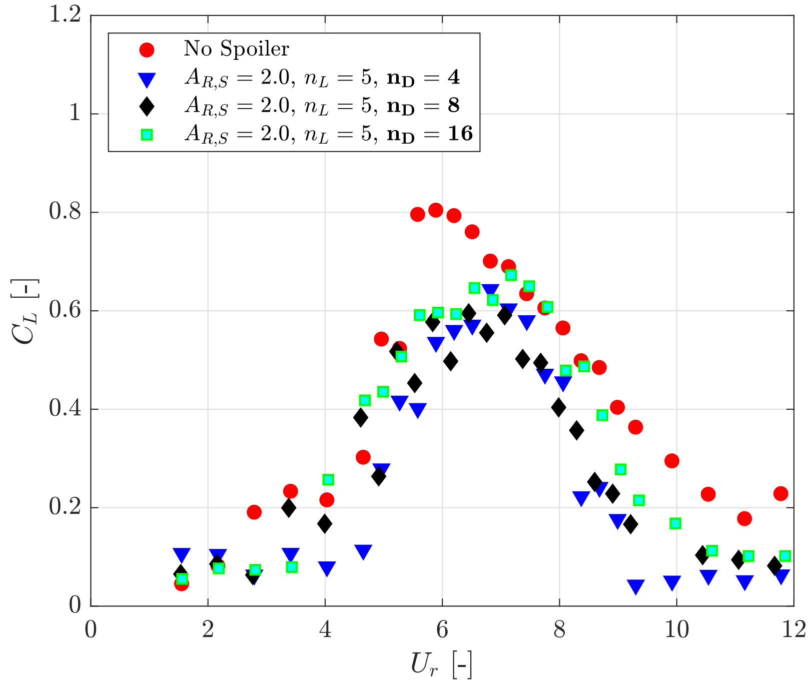

Figure B.13: Effect of n_D on the lift coefficient, C_L

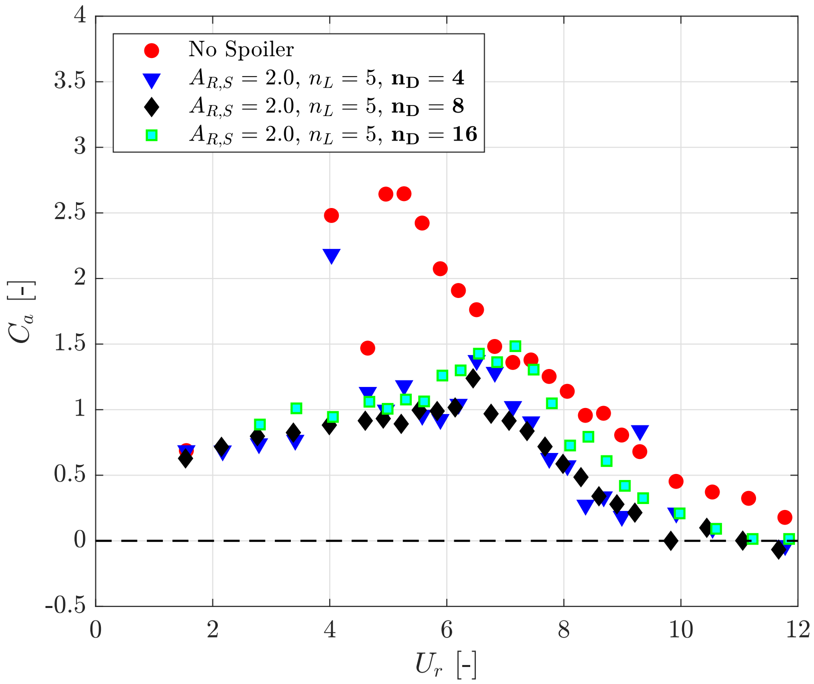

Figure B.14: Effect of n_D on the added mass coefficient, C_a

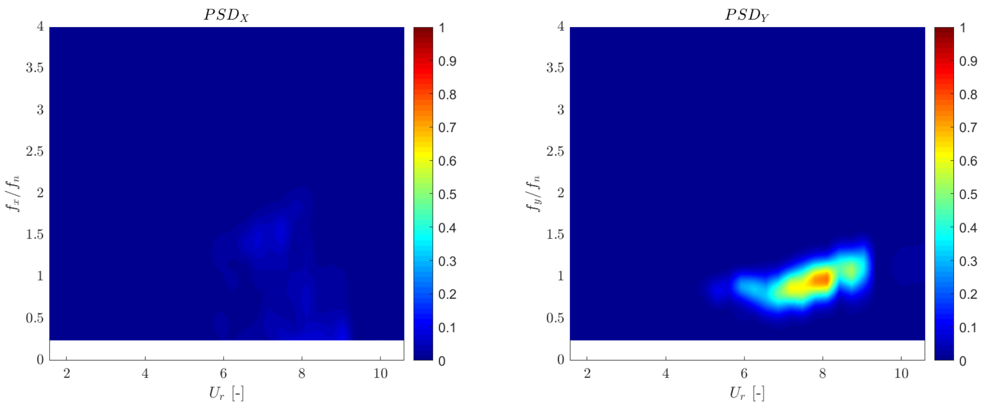

Figure B.15: Normalized Power Spectrum Density of the motion in the inline (a) and transverse (b) direction for $A_{R,S} = 2.0$, $n_L = 5$ and $n_D = 4$

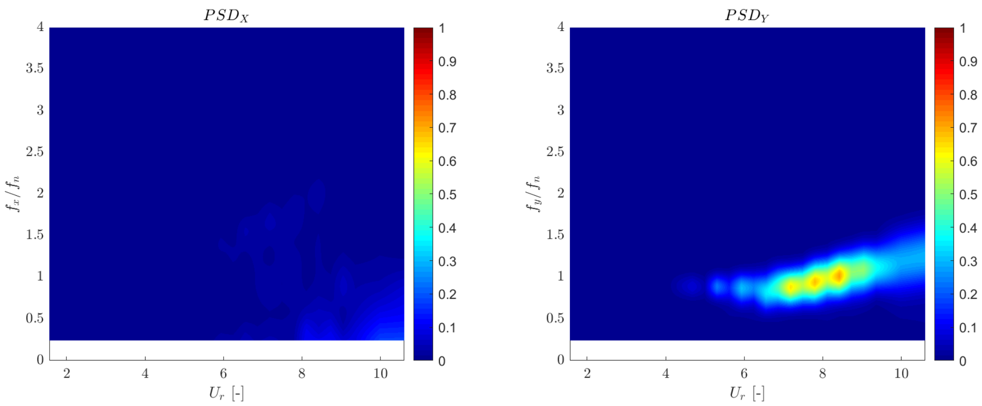

Figure B.16: Normalized Power Spectrum Density of the motion in the inline (a) and transverse (b) direction for $A_{R,S} = 2.0$, $n_L = 5$ and $n_D = 8$

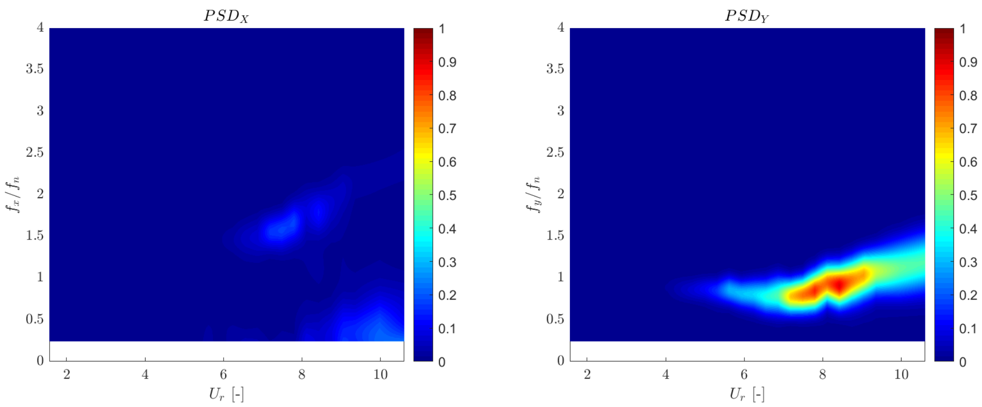

Figure B.17: Normalized Power Spectrum Density of the motion in the inline (a) and transverse (b) direction for $A_{R,S} = 2.0$, $n_L = 5$and $n_D = 16$